



DETERMINATION OF STRESS INTENSITY FACTORS IN CRACKED PANELS  
REINFORCED WITH RIVETED STIFFENERS

A THESIS SUBMITTED TO  
THE GRADUATE SCHOOL OF NATURAL AND APPLIED SCIENCES  
OF  
MIDDLE EAST TECHNICAL UNIVERSITY

BY

M. BURAK SAYAR

IN PARTIAL FULFILLMENT OF THE REQUIREMENTS  
FOR  
THE DEGREE OF MASTER OF SCIENCE  
IN  
AEROSPACE ENGINEERING

FEBRUARY 2012

Approval of the thesis:

**DETERMINATION OF STRESS INTENSITY FACTORS IN CRACKED PANELS  
REINFORCED WITH RIVETED STIFFENERS**

submitted by **M. BURAK SAYAR** in partial fulfillment of the requirements for the degree of **Master of Science in Aerospace Engineering Department, Middle East Technical University** by,

Prof. Dr. Canan ÖZGEN  
Dean, Graduate School of **Natural and Applied Sciences**

\_\_\_\_\_

Prof. Dr. Ozan TEKİNALP  
Head of Department, **Aerospace Engineering**

\_\_\_\_\_

Prof. Dr. Altan KAYRAN  
Supervisor, **Aerospace Engineering Dept., METU**

\_\_\_\_\_

Prof. Dr. Rıza GÜRBÜZ  
Co-supervisor, **Metallurgy and Materials Engineering Dept., METU**

\_\_\_\_\_

**Examining Committee Members:**

Assist. Prof. Dr. Demirkan ÇÖKER  
Aerospace Engineering Dept. , METU

\_\_\_\_\_

Prof. Dr. Altan KAYRAN  
Aerospace Engineering Dept. , METU

\_\_\_\_\_

Prof. Dr. Rıza GÜRBÜZ  
Metallurgy and Materials Engineering Dept. , METU

\_\_\_\_\_

Assist. Prof. Dr. Ercan GÜRSES  
Aerospace Engineering Dept. , METU

\_\_\_\_\_

M. Sc. Evren TAŞKINOĞLU  
TUSAŞ Aerospace Industries. ,TAI

\_\_\_\_\_

**Date:**

\_\_\_\_\_

**I hereby declare that all information in this document has been obtained and presented in accordance with academic rules and ethical conduct. I also declare that, as required by these rules and conduct, I have fully cited and referenced all material and results that are not original to this work.**

Name, Last Name: M. BURAK SAYAR

Signature :

# ABSTRACT

## DETERMINATION OF STRESS INTENSITY FACTORS IN CRACKED PANELS REINFORCED WITH RIVETED STIFFENERS

SAYAR, M. Burak

M.Sc., Department of Aerospace Engineering

Supervisor : Prof. Dr. Altan KAYRAN

Co-Supervisor : Prof. Dr. Rıza GÜRBÜZ

February 2012, 131 pages

This thesis presents a study about the determination of the stress intensity factors in cracked sheets with riveted stiffeners. Stress intensity factors are determined with both analytical method and finite element method for different combination of rivet/stringer spacing and stringer to sheet stiffness ratio. Analytical part of the thesis is a replication of the original study of Poe which assumes rigid rivet connections with no stringer offset. In the analytical part, the whole systems of equations of Poe are re-derived, and it is shown that there are two typographical errors in the expressions for the calculation of the influence coefficients of the cracked sheet and the stringer. Major objective of the analytical part is to develop a computer code which calculates the variation of the normalized stress intensity factor with the crack length for any combination of rivet/stringer spacing and stringer to sheet stiffness ratio. Analytical part of the study also covers the effect of broken stiffener on the stress intensity factor of the cracked sheet. The stress intensity factors of stiffened cracked sheets are calculated by the finite element method by incorporating fastener flexibility and stringer offset. Finite element solutions are performed by Franc2D/L and Abaqus, and comparisons are made. The effect of geometry, fastener flexibility, and stringer offset on the stress intensity factors are studied by presenting normalized stress intensity factor versus crack length curves. Finally, as a case

study a sample damage tolerant stiffened panel is designed according to FAR 25 safety criteria. Experiments are performed for determining mechanical and crack growth properties of Al 2124 which is used as the material in the case study. Present study showed that the most significant effect on the stress intensity factor is seen when stringer-cracked sheet offset is included in the analysis model.

Keywords: stiffened cracked sheets, fastened stringers, stress intensity factor, finite element method

## ÖZ

### GÜÇLENDİRİLMİŞ PERÇİNLİ PLAKALARDA GERİLİM ŞİDDET KATSAYISININ HESAPLANMASI

SAYAR, M. Burak

Yüksek Lisans, Havacılık ve Uzay Mühendisliği Bölümü

Tez Yöneticisi : Prof. Dr. Altan KAYRAN

Ortak Tez Yöneticisi : Prof. Dr. Rıza GÜRBÜZ

Şubat 2012, 131 sayfa

Bu tezde güçlendirilmiş panellerde çatlak ilerlemesi esnasında oluşan gerilim şiddet katsayılarının hesaplanma yöntemleri ele alınmıştır. Gerilim şiddet katsayıları, değişen çatlak boyu kirişler arasına uzaklık oranı ve çeşitli kiriş/çatlak levha sağlamlık oranları için analitik ve numerik yöntemlerle hesaplanmıştır. Analitik hesaplamada Poe'nin yöntemi esas alınmış sonsuz sağlamlıkta perçinler kullanılmıştır, ayrıca kirişler ile çatlak içeren levha aynı düzlemde kabul edilmiştir. Analitik çalışmanın esasını oluşturan bütün denklemler yeniden türetilmiş, katsayılar yeniden hesaplanmıştır. Buna ek olarak kırık kirişin altından ilerleyen çatlak durumu için de katsayılar düzenlenmiş, ve çalışmaya dahil edilmiştir. Analitik çalışmanın ana amacı normalize edilmiş gerilim şiddet katsayılarının değişik çatlak boyları ile değişimini, çeşitli kiriş/levha sağlamlık oranları ve, perçinler arası uzaklık kirişler arası uzaklık oranları için hesaplayan bilgisayar programını geliştirmektir. Analitik çalışmayı sonlu elemanlar analizleri takip etmiş, analizler için Franc2D/L ve Abaqus kullanılmıştır. Çıkan sonuçlar birbirleri ile ve analitik yöntemle karşılaştırılmıştır. Geometrik faktörler, perçin esnekliği, kalınlık offseti gibi birçok değişkenin çözümlere olan etkisi incelenmiş ve irdelenmiş, çatlak uzunluğu, normalize edilmiş gerilim şiddet katsayısı grafikleri ile içerikte sunulmuştur. Son olarak, gerilim şiddet katsayısı hesaplarının önemini ve işlevini vurgulamak için, FAR 25 kriterlerine

uygun örnek hasara toleranslı güçlendirilmiş panel tasarlanmış, tasarımda alüminyum 2124 kullanılmıştır. Malzemenin mekanik ve çatlak hızı özellikleri ise deneyler ile elde edilmiştir.

Anahtar Kelimeler: güçlendirilmiş paneller, gerilim şiddet katsayısı, çatlak ilerlemesi, perçinli plakalar, sonlu elemanlar yöntemi

*Rock'n Roll is forever to stay*

## ACKNOWLEDGMENTS

First, I would like to emphasize my special thanks to Prof. Dr. Altan KAYRAN for guiding me throughout the thesis work. He was the one to help me when I was hopelessly struggling with the complex equations. Being involved in every single part of the thesis, he shared his invaluable knowledge with me whenever necessary. I can honestly say that without his guidance and support, accomplishment of this thesis would be nearly impossible. Thanks for being so friendly, curious and careful. All necessary items are provided by Prof. Dr. KAYRAN.

As well, I would like to express my sincere gratitude to Prof. Dr. Rıza GÜRBÜZ for his invaluable help and encouragement in conducting the experimental study. He was the one to encourage me to make me try again, after my first unsuccessful attempt of the experiments. Also I would like to thank him for being so friendly to me, and using his power in the Materials Engineering Department for keeping the work environment as comfortable as possible. Thanks for the understandings and sincere talks throughout the three years of work life.

I would like to give special thanks to the Göksu GÜRER for helping me, and teaching me how to use the experimental set-up. Without his friendship, support and guidance it would be very difficult to accomplish the experimental study.

I also want to thank to Asst. Prof. Dr. Demirkan ÇÖKER for being so nice and understanding to me throughout the two years of my assistance life. I am very happy for getting to know him and working together. I also want to thank him for his wise advises and showing me another window on the world, and also saving me of giving an incredibly boring presentation in the ICEAF Conference in Greek.

As well, thanks to another important person Evren Eyüp TAŞKINOĞLU, whom I used to worked in TAI together. He was the first person dealing with the fatigue and damage tolerance, and he gave me the inspiration for investigating such a specific topic.

I pour out my warm thanks to my old friend, my bro Mert ATASOY, and his beautiful fiance

Çiğdem Ayşenur ŞAFAK. As always being warm and funny, they always kept my motivation high. They are the most enjoyable couple around me. I can intimately say that, I feel very lucky to get to know this two beautiful people.

There are also three special people whom I had given many concerts with, they are three dangerous Bad Bull's, my bro Gönenç GÜRSOY, Kenan CENGİZ, and Oğuzhan GÜRS. When my thrill is gone, they always gave me power, and motivation to go on. I am very happy that I am sharing the walk of life with them. Badbull is forever to stay. Likewise, I want to thank to my old friends, brothers, all AŞIR fellowship members, Oğuz, Ufuk, İlker, Emre, Aşır, Hamza, Can, İbrahim, and our Aşures for those mentally healing and entertaining moments. Special thanks to Semra Sultan, Türkiye's and Europe's mother in law, for the delicious food. She is always like a real mother to us.

I also want to thank to my little small rabbit Sino, and my little blue friend Şakir, with whom I shared everything in the last two years of my life. As being lovely and funny, Sino always cheered me up and kept me alive whenever I felt tore down, and Şakir was always with me never letting me feel alone.

Last, but not least, I would like to express my deepest thanks to my parents Şadiye and Ahmet Bilgin, and also to my sister Ezgi, for their endless support, trust, love, understanding and patience. Without their love it would not be possible for me to finish this thesis.

# TABLE OF CONTENTS

ABSTRACT . . . . .	iv
ÖZ . . . . .	vi
ACKNOWLEDGMENTS . . . . .	ix
TABLE OF CONTENTS . . . . .	xi
LIST OF TABLES . . . . .	xv
LIST OF FIGURES . . . . .	xvi
LIST OF ABBREVIATIONS . . . . .	xxi
 CHAPTERS	
1 INTRODUCTION . . . . .	1
1.1 Motivation of the Study . . . . .	1
1.2 Background and Literature Survey . . . . .	3
1.3 Flight Loads on the Fuselage Panels . . . . .	6
1.4 Critical Crack Directions . . . . .	7
1.5 Influence of Geometry . . . . .	8
1.6 Contribution of the Thesis to Literature . . . . .	8
1.7 Scope of the Thesis . . . . .	10
2 ANALYTICAL STUDY . . . . .	11
2.1 Formulation of the Problem . . . . .	11
2.1.1 Stiffened panel with intact stiffeners . . . . .	11
2.1.2 Stiffened panel with a broken stiffener . . . . .	14
2.2 Influence Coefficients . . . . .	16
2.2.1 $A_{ij}$ Coefficient-Displacement at the $i$ th Rivet on the Cracked Sheet due to the Unit Force at the $j$ th Rivet . . . . .	16

2.2.2	$A_{ij}^s$ Coefficient-Displacement at the $i$ th Rivet on the Stiffener due to the Unit Force at the $j$ th Rivet . . . . .	25
2.2.3	$B_i$ Coefficient-Displacement on the Cracked Sheet at the $i$ 'th Rivet due to the Uni-axial Loading . . . . .	26
2.2.4	$B_i^s$ Coefficient-Displacement on the Stiffener at the $i$ 'th Rivet due to the Uni-axial Loading . . . . .	28
2.2.5	$\bar{A}_{ij}^s$ Coefficient-Displacement at the $i$ th Rivet on the Broken Stiffener due to the Unit Force at the $j$ th Rivet . . . . .	28
2.2.6	$\bar{B}_i^s$ Coefficient . . . . .	29
2.3	Results of the analytical solution . . . . .	30
2.3.1	Variation of stress intensity factor for different crack configurations . . . . .	31
2.3.2	Variation of $K_N$ with the normalized crack length $a/b$ . . . . .	33
2.3.3	The effect of the rivet pitch to stringer pitch $p/b$ on $K_N$ . . . . .	33
2.3.4	The effect of the <i>Stiffness Ratio</i> on $K_N$ . . . . .	34
2.3.5	The effect of the <i>rivet diameter</i> on $K_N$ . . . . .	41
3	DETERMINATION OF THE STRESS INTENSITY FACTOR BY THE FINITE ELEMENT METHOD . . . . .	43
3.1	Determination of Stress Intensity Factors by Franc2D/L Analysis . . . . .	43
3.1.1	Model Definition . . . . .	44
3.1.1.1	Intact stiffener model . . . . .	44
3.1.1.2	Broken stiffener model . . . . .	44
3.1.2	Analysis results of Franc2D/L for the intact and broken stiffener configurations . . . . .	45
3.1.2.1	The effect of rivet material . . . . .	48
3.2	Determination of Stress Intensity Factors by Abaqus Analysis . . . . .	49
3.2.1	Analysis results of Abaqus . . . . .	50
3.2.1.1	The effect of physical diameter of the rivet on the stress intensity factor . . . . .	53
3.2.1.2	The effect of sheet-stiffener offset on the stress intensity factor . . . . .	55
4	LIFE PREDICTION OF A STIFFENED PANEL . . . . .	58
4.1	Introduction . . . . .	58
4.1.1	Technical Specifications and Geometry of the Aircraft . . . . .	58

4.2	Methodology of damage tolerance analysis . . . . .	60
4.2.1	Calculation of Loads . . . . .	60
4.2.2	Determination of the normalized stress intensity factor with FEM . . . . .	62
4.2.2.1	Model Definition . . . . .	62
4.2.2.2	Analysis results . . . . .	68
4.2.3	Experimental Material Characterization . . . . .	72
4.2.3.1	Mechanical Properties . . . . .	72
4.2.4	Life assessment of the fuselage panel with a broken stiffener	74
4.2.4.1	Paris and Erdoğan Model . . . . .	74
4.2.4.2	Forman Model . . . . .	75
4.2.4.3	Nasgro Model . . . . .	76
4.2.5	Determination of Critical Fracture Toughness and Crack Constants . . . . .	77
4.2.5.1	Determination of Critical Fracture Toughness	78
4.2.5.2	Determination of the Paris and Erdoğan Constants . . . . .	79
4.2.5.3	Determination of the Forman Constants . . . . .	79
4.2.6	Life Calculation with AFGROW . . . . .	81
4.3	Analysis Results of AFGROW . . . . .	84
4.3.1	Stage 1 . . . . .	84
4.3.2	Stage 2 . . . . .	86
4.3.3	Conclusion . . . . .	89
5	CONCLUSION . . . . .	90
	REFERENCES . . . . .	95
	APPENDICES	
A	DERIVATION OF INFLUENCE COEFFICIENTS . . . . .	99
A.1	Derivation of $B_i$ Coefficient . . . . .	99
A.2	Derivation of $A_{ij}^s$ Coefficient . . . . .	103
A.2.1	Derivation of $\Psi_0$ . . . . .	104
A.2.2	Derivation of $\Psi_n$ . . . . .	105

A.3	Derivation of $A_{ij}$ Coefficient . . . . .	106
	A.3.1 Derivation of Equation (2.9) . . . . .	106
	A.3.2 Derivation of Equation (2.10) . . . . .	107
	A.3.3 Derivation of Equation (2.14) . . . . .	108
	A.3.4 Derivation of Equation (2.17) . . . . .	109
<b>B</b>	<b>TESTING OF MATERIAL PROPERTIES . . . . .</b>	<b>111</b>
B.1	Micro-structure Analysis . . . . .	111
B.2	TENSION TEST . . . . .	114
B.3	FRACTURE TOUGHNESS TEST . . . . .	116
	B.3.0.1 First fracture toughness experiment . . . . .	120
	B.3.0.2 Second fracture toughness experiment . . . . .	122
	B.3.0.3 Validity requirements, and Calculation of the $K_q$ . . . . .	123
B.4	CRACK PROPAGATION TEST . . . . .	124

## LIST OF TABLES

### TABLES

Table 4.1	Technical Specifications and Geometry of the Cargo A/C . . . . .	59
Table 4.2	Boundary conditions on the local model shown in Figure 4.6 . . . . .	64
Table 4.3	Applied forces on the local model shown in Figure 4.7 . . . . .	64
Table 4.4	Stress Intensity Factors [ $MPa \sqrt{m}$ ] for various crack lengths [ $mm$ ] for the curved fuselage panes with a broken stiffener under internal pressure . . . . .	70
Table 4.5	Room-Temperature Plane-Strain Fracture Toughness of Aluminum 2124- T851 [40] . . . . .	73
Table 4.6	Paris and Erdoğan Constants for Al 2124 T-851 . . . . .	79
Table 4.7	Forman Constants for Al 2124 T-851 . . . . .	80
Table 4.8	Stage 1(a): Double through crack propagating on the stringer, Forman Eq. . .	84
Table 4.9	Stage 1(b): Edge through crack propagating on the stringer, Forman Eq. . .	85
Table 4.10	Stage 1: Double through crack at the rivet hole propagating on the skin, Forman Eq. . . . .	86
Table 4.11	Stage 2: Center through crack propagates on the skin, Forman Eq. . . . .	87
Table B.1	Tension Test Results . . . . .	115
Table B.2	Compact tension specimen test data . . . . .	120
Table B.3	Compact tension specimen test results . . . . .	121
Table B.4	Compact tension specimen test data . . . . .	122
Table B.5	Compact tension specimen test results . . . . .	123
Table B.6	Inverse Bleasdale Equation Coefficients and squared absolute error . . . . .	129
Table B.7	Compact tension specimen test data . . . . .	129

# LIST OF FIGURES

## FIGURES

Figure 1.1 Aloha Airlines Boeing 737-200 experienced explosive decompression after 89,681 flight cycles [2] . . . . .	2
Figure 1.2 Crack should be arrested before it reaches to the critical limit, FAR 25.571 Two Bay Criteria [1] . . . . .	3
Figure 1.3 Complex loading of fuselage panels [1] . . . . .	7
Figure 1.4 Cabin pressure [1]. . . . .	7
Figure 1.5 Bi-axial loading of stiffened panels due to the cabin pressure[1] . . . . .	7
Figure 1.6 Critical crack directions under bi-axial loading [1] . . . . .	8
Figure 2.1 Definition of the problem [6] . . . . .	12
Figure 2.2 Symmetrical rivet forces acting on the cracked sheet [6] . . . . .	13
Figure 2.3 Broken stiffener geometry description [7] . . . . .	14
Figure 2.4 Superposition for $A_{ij}$ Coefficient [6] . . . . .	17
Figure 2.5 Point force at the origin [6] . . . . .	17
Figure 2.6 Distributing the point rivet force over the rivet diameter . . . . .	18
Figure 2.7 Symmetrical four point forces acting on four quadrant . . . . .	19
Figure 2.8 Westergaard solution for symmetrical four point forces applied on the crack surface [6] . . . . .	22
Figure 2.9 Distributing the point load so as to simulate the $\overline{\sigma_{yy}}$ on Figure 2.4 . . . . .	23
Figure 2.10 Cracks Handbook Formulation for symmetrical four point forces acting on a cracked sheet [13] . . . . .	24
Figure 2.11 Approximating a finite width stringer by an infinite size sheet [6] . . . . .	25
Figure 2.12 Cracked sheet subject to uni-axial loading [6] . . . . .	27

Figure 2.13 Displacement of the stiffener under uni-axial loading [6] . . . . .	28
Figure 2.14 Superposition for $\bar{A}_{ij}^s$ Coefficient [7] . . . . .	29
Figure 2.15 Superposition for $\bar{B}_i^s$ Coefficient [7] . . . . .	29
Figure 2.16 Normalized stress intensity factor vs crack length, $\mu = 1$ . . . . .	30
Figure 2.17 Normalized stress intensity factor for the crack between two intact stiffeners, $\mu = 0.5, d/p = 0.25$ . . . . .	31
Figure 2.18 Normalized stress intensity factor for the crack under intact stiffener, $\mu = 0.5, d/p = 0.25$ . . . . .	32
Figure 2.19 Normalized stress intensity factor for the crack under broken stiffener, $\mu = 0.5, d/p = 0.25$ . . . . .	32
Figure 2.20 Configuration one, $\mu = 0$ . . . . .	35
Figure 2.21 Configuration one, $\mu = 0.3$ . . . . .	35
Figure 2.22 Configuration one, $\mu = 0.5$ . . . . .	36
Figure 2.23 Configuration one, $\mu = 1$ . . . . .	36
Figure 2.24 Configuration three, $\mu = 0$ . . . . .	37
Figure 2.25 Configuration three, $\mu = 0.3$ . . . . .	37
Figure 2.26 Configuration three, $\mu = 0.5$ . . . . .	38
Figure 2.27 Configuration three, $\mu = 0.9$ . . . . .	38
Figure 2.28 Stiffness ratio comparison for configuration one, $p/b = 1/12$ . . . . .	39
Figure 2.29 Stiffness ratio comparison for configuration two, $p/b = 1/12$ . . . . .	39
Figure 2.30 Stiffness ratio comparison for configuration three, $p/b = 1/12$ . . . . .	40
Figure 2.31 Comparison of rivet diameters, configuration one, $\mu = 0.3, p/b = 1$ . . . . .	42
Figure 2.32 Comparison of rivet diameters, configuration one, $\mu = 0.3, p/b = 1/12$ . . . . .	42
Figure 3.1 Finite element model of cracked sheet with riveted stringers (a) Layer 1: Cracked sheet (b) Layer 2: with two distinct material zones; 2:Stringer material, 3:Weak material . . . . .	44
Figure 3.2 Finite element model of the cracked sheet with broken stiffener . . . . .	45
Figure 3.3 Analytical Method vs Franc 2D/L, configuration one, $\mu = 0.33, d/p = 0.25$ . . . . .	46
Figure 3.4 Analytical Method vs Franc 2D/L, configuration one, $\mu = 0.5, d/p = 0.25$ . . . . .	46

Figure 3.5 Analytical Method vs Franc 2D/L, configuration three, $\mu = 0.33$ , $d/p = 0.1875$ . . . . .	47
Figure 3.6 Analytical Method vs Franc 2D/L, configuration three, $\mu = 0.5$ , $d/p = 0.1875$	47
Figure 3.7 Rivet material comparison, $\mu = 0.5$ , $p/b = 1$ . . . . .	48
Figure 3.8 Rivet material comparison, $\mu = 0.5$ , $p/b = 1/4$ . . . . .	49
Figure 3.9 Abaqus finite element model of the cracked sheet with riveted stringers . .	49
Figure 3.10 Stress intensity factor versus crack length for the rigid rivet case: Abaqus vs Franc2D/L, $\mu = 0.33$ . . . . .	51
Figure 3.11 Stress intensity factor versus crack length for the aluminum rivet case: Abaqus vs Franc2D/L, $\mu = 0.5$ . . . . .	51
Figure 3.12 Stress intensity factor versus crack length for the titanium rivet case: Abaqus vs Franc2D/L, $\mu = 0.5$ . . . . .	52
Figure 3.13 Rivet material comparison with Abaqus, $\mu = 0.33$ , $p/b = 1$ . . . . .	52
Figure 3.14 The difference between Analytical and Abaqus rivet formulation . . . . .	53
Figure 3.15 Comparison of the $K_N$ for the effect of rigid rivet diameter on the $K_N$ with Analytical Method . . . . .	54
Figure 3.16 Comparison of the $K_N$ for the effect of rigid rivet diameter on the $K_N$ with Abaqus . . . . .	54
Figure 3.17 The cracked sheet and the stringers are in the same plane . . . . .	55
Figure 3.18 The cracked sheet and the stringer has an offset ( $o$ ) due their thicknesses .	55
Figure 3.19 Cracked sheet and the stiffener are in the mid-plane . . . . .	56
Figure 3.20 Cracked sheet and the stiffener are offsetted . . . . .	56
Figure 3.21 Comparison of the SIF's for the offsetted stiffener with rigid rivets, $\mu = 0.33$ , $d/p = 0.25$ . . . . .	57
Figure 3.22 Comparison of the SIF's for the offsetted stiffener with Aluminum rivets, $\mu = 0.33$ , $d/p = 0.25$ . . . . .	57
Figure 4.1 Cross sectional geometry of the stringer and frame . . . . .	59
Figure 4.2 Longitudinal stress in an cylindrical pressure vessel [37] . . . . .	61
Figure 4.3 Forward center fuselage model . . . . .	62

Figure 4.4	Forward center fuselage, cracked stiffened panel local model . . . . .	63
Figure 4.5	Details of the local model . . . . .	63
Figure 4.6	Boundary conditions applied on the local model shown in Figure 4.4 . . . . .	65
Figure 4.7	Applied forces on the local model shown in Figure 4.4 . . . . .	65
Figure 4.8	Position of the crack in the stiffened panel . . . . .	66
Figure 4.9	Focused mesh around the crack tip; A-B-C nodes are on the crack tip element . . . . .	66
Figure 4.10	Deformed symmetric half crack model containing 90 mm crack over broken stiffener, the deformations are 4X exaggerated . . . . .	68
Figure 4.11	Variation of the normalized stress intensity factor with the crack lengths for the stiffened cargo A/C fuselage panels with a broken stiffener . . . . .	69
Figure 4.12	Finite element models of curved and flat fuselage panel with a broken stiffener . . . . .	70
Figure 4.13	Variation of the $K_N$ with the $a/b$ for the stiffened fuselage panels with and without internal pressure . . . . .	71
Figure 4.14	Variation of the $K_N$ with the $a/b$ for the stiffened fuselage panels with and without curvature under uni-axial stress . . . . .	71
Figure 4.15	Mechanical and Physical Properties of 2124-T851 Aluminum Alloy [40] . . . . .	73
Figure 4.16	$da/dN$ vs $\Delta K$ curve for Al 2124-T851 . . . . .	78
Figure 4.17	Stage 1(a): Double crack starts from a hole on the skin and the stringer at the same time . . . . .	82
Figure 4.18	Stage 1(b): Center crack on the stringer breaks through to the edge; crack on the stringer becomes an edge crack . . . . .	82
Figure 4.19	Stage 2: Stringer is completely broken, and the crack propagates on the skin . . . . .	83
Figure 4.20	Applied forces on the local model shown in Figure 4.4 . . . . .	83
Figure 4.21	Crack growth time history for the skin, utilizing Forman Equation with experimentally determined constants . . . . .	88
Figure 4.22	Crack growth time history for the skin, utilizing NASGRO Equation with using the constants available in database . . . . .	88
Figure A.1	Infinite size cracked sheet under bi-axial loading . . . . .	99
Figure A.2	Crack tip zone . . . . .	102

Figure A.3 Symmetrical four point forces acting on four quadrant . . . . .	103
Figure A.4 Approximation of the finite width riveted stiffener by the infinite size riveted sheet [6] . . . . .	104
Figure A.5 Distributing the point force to the diameter . . . . .	108
Figure B.1 Rolling direction and the grain directions . . . . .	112
Figure B.2 Conventions for the crack planes for plates [59] . . . . .	112
Figure B.3 Specimen inspection under the light microscope for the determination of the rolling direction . . . . .	113
Figure B.4 Stress vs Strain data for Aluminum 2124 T-851 . . . . .	114
Figure B.5 Experiment Equipment . . . . .	116
Figure B.6 CT test specimen geometry used in the experiment for crack propagation .	117
Figure B.7 CT test specimen geometry for crack propagation given in ASTM-E399 [59].	118
Figure B.8 Crack tip details . . . . .	119
Figure B.9 Load vs Displacement data obtained from fracture toughness testing according to E-399 . . . . .	121
Figure B.10 Load vs Displacement data obtained from fracture toughness testing according to E-399 . . . . .	122
Figure B.11 Compact tension test specimen geometry used in the experiment . . . . .	125
Figure B.12 Compact tension test specimen geometry given in ASTM-E647 [61]. . . . .	125
Figure B.13 Crack tip types and the minimum fatigue pre-crack size for compact tension test specimen [61] . . . . .	126
Figure B.14 Cycles vs Crack Length data obtained according to the ASTM-E647 [61] .	128
Figure B.15 Crack growth rate changing with the range of stress intensity factor data obtained from the experiment, Inverse Bleasdale with Offset . . . . .	130
Figure B.16 Crack growth rate changing with the range of stress intensity factor data obtained from the experiment, Secant Method . . . . .	130
Figure B.17 Comparison of the crack growth rate changing with the range of stress intensity factor data obtained with Secant Method, and curve fitting with Inverse Bleasdale Eq. with Offset . . . . .	131

## LIST OF ABBREVIATIONS

<b>General Abbreviations</b>		$d$	Rivet diameter
$K_N$	Normalized stress intensity factor	$p$	Rivet spacing
$\bar{K}$	Stress intensity factor for rivet forces	$r, \Theta$	Polar coordinates
$M_b$	Number of broken stiffeners	$t$	Thickness
$N$	Number of rivets	$w$	Stringer width
$E$	Young's modulus of elasticity	<b>Materials Related Parameters</b>	
$F$	Maximum force in stringer	$\Delta K_{th}$	threshold stress intensity factor
$P$	Point force applied to surface of crack	$\Delta K_0$	threshold stress intensity factor range at $R = 0$
$Q$	Rivet force	$C_{th}$	threshold coefficient
$S$	Applied uni-axial stress	$K_{IC}$	Plain strain fracture toughness
$\sigma_{xx}, \sigma_{yy}$	Normal stress components	$A_k$	Fit parameter
$\bar{\sigma}_{yy}$	Normal stress acting on crack surface	$B_k$	Fit parameter
$\tau_{xy}, \tau_{xz}, \tau_{yz}$	Shearing stress components	$t_0$	Reference thickness (Plain strain condition)
<b>Influence Coefficients</b>		$\sigma_0$	Flow stress in Section 4.2.4.3
$A_{ij}$	Influence coefficient for the displacement at the $i$ 'th rivet because of force of unity at $j$ 'th rivet	<b>Mathematical Functions</b>	
$B_i$	Influence coefficient for the displacement at the $i$ 'th rivet because of applied uni-axial stress of unity	$v$	$y$ component of displacement
$\bar{A}_{ij}$	Influence coefficient, for the relative displacement from the first rivet, at the $i$ 'th rivet because of force of unity at $j$ 'th rivet	$\bar{v}$	Relative displacement
$\bar{B}_i$	Influence coefficient, for the relative displacement from the first rivet, at the $i$ 'th rivet because of applied uni-axial stress of unity	$x, y$	Rectangular Cartesian coordinates
<b>Geometric Parameters</b>		$x_0, y_0$	Rivet coordinates
$a$	Half of the crack length	$Z$	Westergaard stress function
$b$	Stringer spacing	$z$	Complex variable
$b_0$	Specific value of stringer spacing	$\alpha$	Stringer spacing reduction parameter
		$\alpha_1, \alpha_2, \alpha_3, \alpha_4$	Mathematical functions described on page 20
		$\Gamma$	Mathematical function described on page 21
		$\Lambda$	Mathematical function described on page 22
		$\mu$	Stiffness ratio described on page 30
		$\nu$	Poisson's ratio

$\rho_1, \rho_2$	Mathematical functions described on page 27
$\phi_1, \phi_2$	Functions described on page 13
$\Omega$	Function described on page 19

### **Subscripts and Superscripts**

$()_i$	At i'th rivet
$()_j$	At j'th rivet
$()_n$	At n'th rivet
$()_{lim}$	Limiting
$()_s$	Stringer
$()^s$	Stringer
$()^{bs}$	Broken stiffener

### **Acronyms**

<i>SIF</i>	Stress intensity factor
<i>LEFM</i>	Linear elastic fracture mechanics
<i>FEM</i>	Finite element method
<i>A/C</i>	Aircraft
<i>C/S</i>	Cross section
<i>GAG</i>	Ground-Air-Ground
<i>NDT</i>	Non Destructive Inspection Technique
<i>BC</i>	Boundary Condition

# CHAPTER 1

## INTRODUCTION

### 1.1 Motivation of the Study

*Fatigue* is a progressive failure mechanism and material degradation due to the cyclic loads which results in crack nucleation and propagation. Fatigue failures are very dangerous because it is unexpected and it happens suddenly which may lead to the failure of the complete structure. Fatigue should be taken into consideration in order to avoid unexpected failure during design. There are two design concepts for considering the fatigue, firstly the crack free design in other words fatigue approach, secondly the damage tolerance approach.

The fatigue design philosophy is based on the assumption that a structure must remain crack-free during its service life is called as Safe Life Design.

Damage Tolerance is another fatigue design philosophy based on the assumption that a structure must be safe even if it is damaged. Damage tolerance design requirements are specified in MIL and JAR/FAR, and are generally satisfied by applying two concepts:

1. Fail-safe design criteria where unstable crack propagation is locally contained through the use of multiple load paths or crack stoppers.
2. Slow crack growth design concept where flaws or defects are not allowed to attain the size required for unstable crack propagation.

In 1988, Aloha Airlines experienced an explosive decompression at 24,000 feet altitude after 89,681 flight cycles which showed that fatigue analysis is necessary but not sufficient for determining the life of the aircraft [1].



Figure 1.1: Aloha Airlines Boeing 737-200 experienced explosive decompression after 89,681 flight cycles [2]

Therefore, new regulations are introduced to aircraft industry which is about Fatigue and Damage Tolerant design of the aircraft. The philosophy under the damage tolerance concept is that, every structure has a crack and it is progressively propagating, therefore for the structure to sustain its integrity, it has to withstand the damage. In other words, structure must be safe even if it is damaged. Moreover the structure must be designed such that crack growth must be slow. The reason of desiring the slow crack growth is that, as the crack moves slower, the flight cycles between inspection intervals which are determined considering the crack growth rate, is allowed to be longer. The best design is the design for which the inspection intervals are the longest, and the crack moves the slowest. Longer inspection intervals will reduce the maintenance cost, and the risk of failing of panels significantly.

According to FAR 25.571 two bay criterion, the crack must be arrested in two frame bays [3]. In other words, the crack should be detected, and precautions should be taken before the crack passes through two bay. The time history information of the crack should be known to design the panel properly according to the damage tolerance specifications.

In order to get the time history information, the geometry of the panel and the loading condition should be considered together. Generally stiffened panels are sized according to the cabin pressure loading [4] at least for the first stages of design, which causes the most critical type of loading for the panels. The geometry effect is taken into account by the normalized stress intensity factor, which is the stress intensity factor of the cracked stiffened panel divided by the stress intensity factor of the cracked infinite sheet Equations (1.1a) and (1.1b). Stress intensity factor is a powerful and important tool used in linear elastic fracture mechanics. Stress intensity factor can be used for life prediction, but in the case of complex geometries

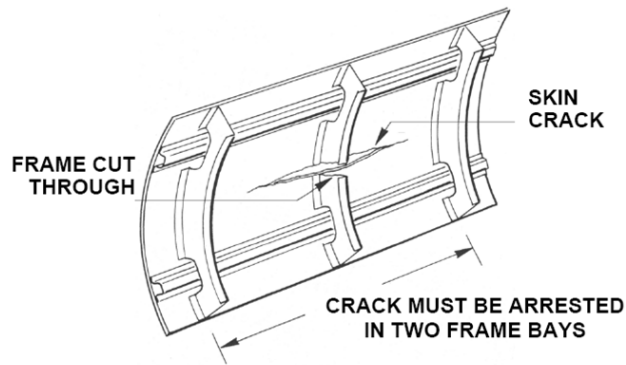


Figure 1.2: Crack should be arrested before it reaches to the critical limit, FAR 25.571 Two Bay Criteria [1]

and complex loading, determination of stress intensity factor is very difficult by analytical methods, therefore the only way to determine the SIFs is by using the finite element method. This thesis is dedicated to developing reliable methodologies for determining stress intensity factors for cracked stiffened panels both analytical method and finite element method.

## 1.2 Background and Literature Survey

Fracture mechanics analysis of stiffened panels, that are typically used in aerospace structures, is a subject that has been studied extensively in the literature. In this section some of these studies are highlighted to give an insight to the reader on the background of the subject.

Bloom and Sanders [5] investigated the effect of a rivet-attached stringer on the thin elastic cracked sheet, which is loaded at the infinity by a uniform tensile stress.

The original work, which is one of the key references on the calculation of the stress intensity factor for cracked sheets with riveted stringers, is done by Poe [6]. The variation of the stress intensity factor in the stiffened cracked sheets with the crack length for discrete rivet pitch, stringer spacing and stringer to total panel stiffness ratios are considered in this report. In his study, Poe presented an analytical formulation to determine the variation of the stress intensity factor with the cracked length, for cracks extending equally on both sides of point midway between two stringers, and crack extending equally on both sides of the stringer. On a follow-up study, Poe presented results on the effect of broken stringers on the stress intensity factor for a uniformly stiffened sheet containing a crack [7, 8]. According to Newman [9] the effect of the holes on the SIF is negligible if the crack tip is more than one diameter away from the

rivet hole. Hence, Poe neglected the rivet hole effect in the formulation.

Rooke and Cartwright [10] extended the compounding method for determining approximate stress intensity factors to stiffened sheets with cracks. The compounding method is also included in the ESDU (Engineering Sciences Data Unit) database [11]. ESDU is an engineering advisory organization based in the United Kingdom which provides validated engineering analysis tools to engineers and teachers in the aerospace engineering, process engineering and structural engineering fields.

In references [6, 7, 10, 11], rivet flexibility was not taken into account in determining the stress intensity factor. Swift [12] included fastener flexibility and bending effect in the stress intensity factor calculations, and showed that considerable error in the stress intensity factor can be produced by ignoring fastener flexibility and the stiffener offset. Swift alternatively used the Westergaard formulation in Cracks Handbook [13] for four symmetrical point forces, which is derived with the manipulation of the Westergaard formula [14]. Previous fundamental studies [6, 7, 10, 11, 12] on the fracture mechanics analysis of stiffened panels are still referenced by the damage tolerance standards of aircraft companies such as Airbus.

Finite element and boundary element methods are also frequently used in the fracture analysis of stiffened panels [15, 16, 17, 18]. *MSC/NASTRAN* developed a primitive crack tip element *CRAC2D and CRAC3D* [19] which can be used in 2D and 3D problems for extracting the SIF. The main problem with this element is about the user interface. The crack element has to be created directly from the input file, and all the nodes around the crack should be tracked very carefully. Moreover, the output produced by this element is very sensitive to mesh size, therefore SIF extraction for a crack length is not practical, and tracking SIF for a propagating crack is very painstaking.

*Franc2D/L* is a two dimensional finite element based program for simulating crack propagation for planar structures [20]. *Franc2D/L* is a very simple and useful software which is very popular among the engineers. It can simulate the planar structures for the plain stress and the plain strain cases, also it has simple rivet and cohesive elements which only takes the shear stiffness into account. The most beautiful thing about *Franc2D/L* is that it can propagate the crack automatically. Therefore in a model, there is a chance to extract SIF for different crack lengths. The only disadvantage of *Franc2D/L* in crack problems is that, it has a very simple pre-processor *CASCA*, and there are many limitations in creating the model

with CASCA. Moreover, Franc2D/L is capable of simulating limited number of layers [20]. Although there is some open source codes for translating some of the FEM input files such as ANSYS, ABAQUS, PATRAN... etc [21], it is not very practical to do this. In addition, the Kansas State University version of Franc2D/L[20] has some differences from the Cornell University version [21]. Although Franc2D/L is a very powerful tool for simulating plane problems, it can not be used for simulations in 3D space even if the plane structures are to be modeled.

*Franc3D* can be used in 3D simulations. Especially for modeling the shell structures, STAGS (SStructural Analysis of General Shells) module may be used [22]. According to Seshadri [15], there is a very good correlation between the test results and the STAGS analysis results for cracked aluminum stiffened sheet.

*ABAQUS* is also a very powerful software for a crack problem. Simulating a stationary crack in 2D or 3D structures is quite practical in Abaqus [23]. The main problem with simulating the crack problems with FEM is that, the solution is dependent on the mesh size. Therefore the crack tip should be meshed carefully. Moreover, for every single crack length a new model has to be prepared, because ABAQUS does not have the ability to propagate the crack. Although X-Fem module of the ABAQUS enables a crack growth independent of the mesh, it has some limitations [24, 25, 26, 27, 28, 29] such that;

- Only the STATIC analysis procedure is allowed.
- Only linear continuum elements are allowed (CPE4, CPS4, C3D4, C3D8) with or without reduced integration.
- No contour integrals for cracks (available in Abaqus 6.9-EF6 and later for linear brick and tetrahedron elements).
- No fatigue crack growth.
- Domain must contain single or non-interacting cracks.
- Only one crack may exist within a particular element.
- A crack may not turn more than 90 degrees within a particular element.
- A crack may not branch.

- Not available in Abaqus/Explicit.

In this thesis, for modeling cracks, ABAQUS static edge crack with contour integration module is used [23]. For the pre-determined crack paths, it can be logical to use the fracture interface elements with the virtual crack closure technique [17]. Some of the commercial FEM software such as MSC/MARC, ANSYS, ABAQUS...etc, has the ability to simulate the crack problem with the virtual crack closure technique.

Experimental methods can also be used for determining the stress intensity factor for complex geometries. Nurse, Güngör and Peterson [30] demonstrated how transmission photo-elasticity has been used to determine the stress intensity factor for stiffened plates in tension for cracks that are developed at a center hole. In the experiment, stiffeners are attached to the plate at a right angle. Because aluminum is an opaque material transmission photo-elasticity can not be used. Digital image correlation technique may be an alternative for determining the stress intensity factors for stiffened aluminum plates but unfortunately the experiment set up is not available in the METU.

### **1.3 Flight Loads on the Fuselage Panels**

During the flight, fuselage panels are exposed to complex loading, such as shear coming from torsion, transverse shear, axial stresses and bending stresses as it is illustrated in Figure 1.3. In such a complex geometry and complex loading, there is a need to do some simplifications. An engineer has to decide how to design the panel so as to be safe side and think what to consider in the calculations. Therefore in aircraft industry, it is a rule of thumb that in the initial stages of the design, the fuselage is sized considering the cabin pressure which results in a bi-axial loading, also this is the most critical load case for stiffened fuselage panels.

According to damage tolerance design philosophy, the most critical scenario has to be chosen and aircraft should be designed such that; it must remain safe even if it experiences the worst case load. As it is commonly known, the first mode, in other words the crack opening mode, is the most critical fracture mode which is responsible for the propagation of the crack. Therefore,  $K_I$  loading is the most dangerous type of loading in aerospace structures. Sources of force which can create the  $K_I$  loading are the cabin pressure load for the fuselage, lift force for wings, and other aerodynamic and inertial forces for the whole aircraft.

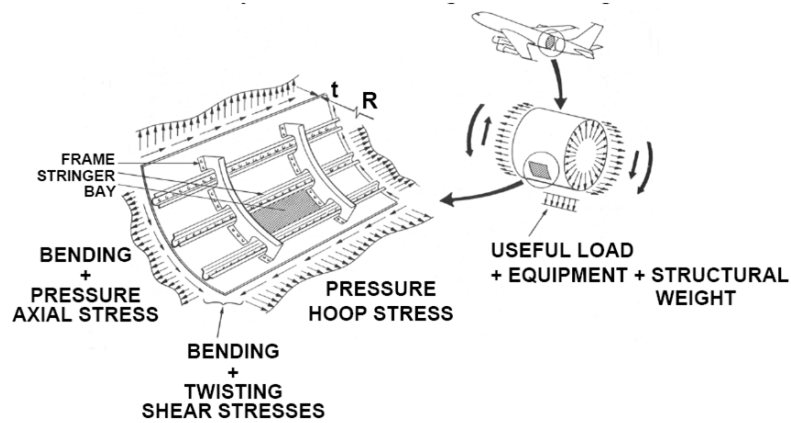


Figure 1.3: Complex loading of fuselage panels [1]

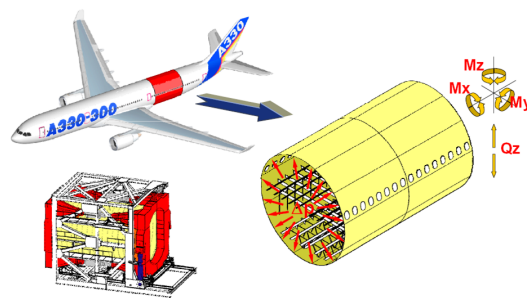


Figure 1.4: Cabin pressure [1].

Due to the cabin pressure illustrated in Figure 1.4, the fuselage panels are loaded bi-axially as it is shown in Creff:BiaxialLoading. Such a loading may lead to radial and circumferential cracks in the skin of the aircraft.

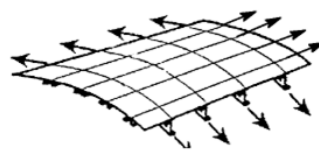


Figure 1.5: Bi-axial loading of stiffened panels due to the cabin pressure[1]

## 1.4 Critical Crack Directions

Under the bi-axial loading, the most critical crack possibilities are shown in Figure 1.6, which are longitudinal and circumferential cracks.

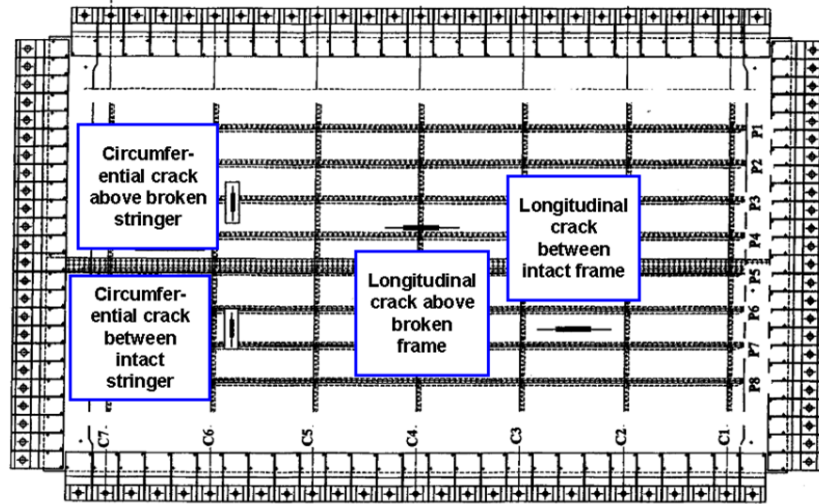


Figure 1.6: Critical crack directions under bi-axial loading [1]

## 1.5 Influence of Geometry

The effect of the geometry of the panel is taken into account with normalized stress intensity factor, which is the stress intensity of the stiffened panel divided by the stress intensity of the cracked infinite sheet. In fracture mechanics it is known as the geometry factor  $\beta$ .

$$K_N = \frac{K_I}{K_0} \quad (1.1a)$$

$$K_N = \frac{\beta\sigma\sqrt{\pi a}}{\sigma\sqrt{\pi a}} = \beta \quad (1.1b)$$

## 1.6 Contribution of the Thesis to Literature

This thesis has the following contributions to the area of determining stress intensity factors in the stiffened panels:

1. Sources of the typographical errors in the original study of Poe are shown and corrections are made. A code is developed to calculate the variation of the normalized stress intensity factor with respect to crack length for any combination of geometrical parameters and stringer to sheet stiffness ratio. Poe's report gives the stress intensity curves for certain discrete values of geometrical parameters such as stringer pitch, rivet pitch,

stringer to sheet stiffness ratio etc [6, 7]. However, for the intermediate values of the geometrical and material parameters one has to interpolate from the curves which are available in Poe's reports. Therefore, the geometrical and material parameters which are outside the range studied by Poe, one needs to develop a computer program and replicate the Poe's study. One of the main contribution of the thesis is the development of the code for the determination of stress intensity factors in cracked stiffened sheets. With such a code stress intensity factor calculation can be performed for continuous variation of the geometric and material parameters. Correction of the typographical errors in the original study of Poe is another contribution which is linked to the analytical part of the study. A code based on the equations given in Poe's report gives incorrect stress intensity factors, hence without the re-derivation of the complete system of equations in Poe's report, it could not have been possible to find the sources of the typographical errors.

2. A robust finite element modeling methodology is developed with Abaqus and Franc2D/L for extracting the stress intensity factors in the stiffened panels.
3. Comparative study of the parameters which influences the stress intensity factor calculations in cracked sheets with riveted stringers is presented by Poe [6] for the intact stiffeners. In this study, formulation modification recommended in the second article of Poe [7] for the broken stiffener is included in the analytical model, parametric study is done on the effect of geometric and material parameters and the design charts for the broken stiffener model is presented, which are not available in the literature.
4. The most significant effect on the stress intensity factor is seen when stringer-cracked sheet offset is included in the analysis model.
5. Analytical modeling is checked with finite element modeling techniques, and in general, very good agreement is observed between the analytical, Franc2D/L and Abaqus results for the various case studies that are conducted, therefore reliability of the analytical method is checked with finite element study.
6. Analytical tool is developed for the determination of the stress intensity factors for the stiffened panels. This tool may be used by the industry after a couple of improvement such as including the effect of stiffener geometry, offset effect, and the rivet flexibility effect explained in detail respectively in Sections 3.1.2.1 and 3.2.1.2.

## 1.7 Scope of the Thesis

To produce continuous data for the stress intensity factor, the formulation given in the report has to be coded.

In the first part of the present study, it is shown that in the report prepared by Poe [6] there are two typographical errors in the expressions for the calculation of the influence coefficients of the cracked sheet and the stringer, respectively. In the thesis, the complete system of equations in Poe's report are re-derived and the sources of the typographical errors are identified. Typographical errors are then corrected and the selected stress intensity factor curves calculated with the original and corrected expressions are compared.

The second part of the thesis is devoted to the finite element modeling and fracture mechanics analysis of stiffened cracked sheets. Franc2D/L [20] and commercial FE software Abaqus [23] are used to model stiffened cracked sheets to determine the variation of the stress intensity factor with the crack length. In the first part of analysis, no rivet flexibility and stiffener offset is considered and an appropriate model is generated to replicate the analytical solution of Poe [6]. Second part of finite element based analysis is performed by incorporating fastener flexibility and stringer offset.

The effect of more accurate modeling of the fastener/stiffener/cracked sheet combination on the variation of the stress intensity factor with the crack length is studied. The differences between the stress intensity factor values obtained by more accurate finite element modeling of cracked sheets with riveted stringers and the analytically obtained stress intensity factor values by Poe [6] are calculated, and conclusions are inferred with regard to the effect of fastener flexibility and stringer offset on the stress intensity factor in stiffened cracked sheets.

## CHAPTER 2

### ANALYTICAL STUDY

#### 2.1 Formulation of the Problem

In this section, firstly the original analytical solution presented by Poe [6] is described briefly, secondly the effect of broken stiffener on the stress intensity is taken into account by modifying the equations which is explained in another article presented by Poe [7].

##### 2.1.1 Stiffened panel with intact stiffeners

A stiffened sheet with equally spaced stringers which is exposed to uni-axial stress is illustrated in Figure 2.1. Assuming that the stiffened panel is a monolithic structure, it can be concluded that the displacements in the stiffener and the crack sheet at the far field are equal to each other. Hence sheet and the stiffener share the stress proportional to their stiffness's. As it can be seen from the Figure 2.1a, there are two critical crack possibilities. These are crack between two intact stiffeners, and crack under the intact stiffener.

According to Poe [6], at the rivet points, the displacements of the cracked sheet and the stiffener must be the same. It should be noted that since the displacements at the far field are the same, without the crack there are no rivet forces. However as the crack forms and propagates, the sheet starts to transfer some of the loads to stringers, therefore forces occur on the rivets due to the load transfer between cracked sheet and the stiffener. Poe presented a method [6] for calculating the unknown rivet forces. In Poe's work, by making use of the Westergaard [13] or Muskehlshvili's methods [31], stress intensity factor due to the rivet forces can be determined.

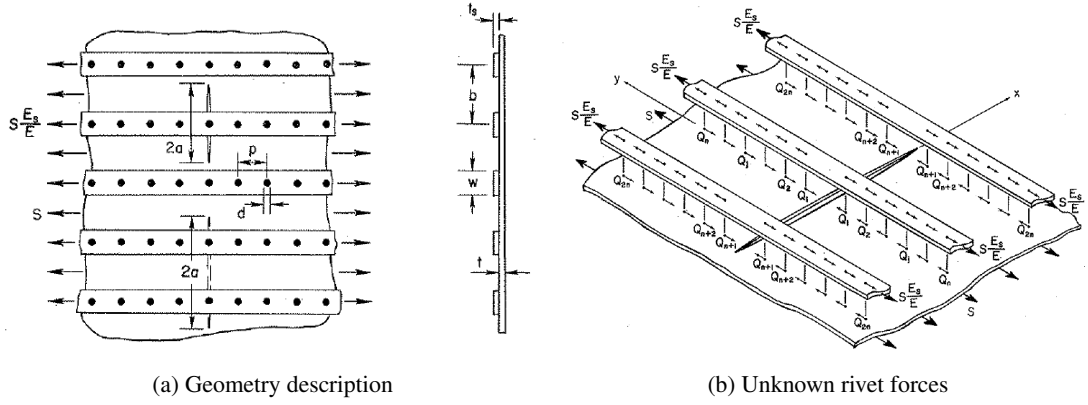


Figure 2.1: Definition of the problem [6]

By superposing the stress intensity factor due to the uni-axial stress and rivet forces, the total SIF in the crack sheet is determined.

The displacements at the rivet points on the stringer  $v_i^s$  and the sheet  $v_i$  should be equated in order to solve for the unknown rivet forces  $Q_j$ 's. This is the fundamental assumption which is used by Poe in solving for the unknown rivet forces. Hence, in the calculation of the displacements, rivet forces on the sheet and stringers are assumed to act at the mid-plane of the sheet, and no offset is considered between the stringer and the sheet. Moreover, Poe's assumption also implies that rivets are rigid.

$$v_i = - \sum_j A_{ij} Q_j + B_i S \quad (2.1a)$$

$$v_i^s = \sum_j A_{ij}^s Q_j + B_i^s \frac{E_s}{E} S \quad (2.1b)$$

where  $A_{ij}$ , and  $A_{ij}^s$  are the influence coefficient for the sheet, and stiffener, respectively. Influence coefficients represents the displacement at the  $i$ 'th rivet due to the force at the  $j$ 'th rivet.  $E$  is the Young's Modulus for the sheet, and  $E_s$  denotes the Young's Modulus for the stiffeners.  $B_i$  and  $B_i^s$  are the influence coefficients for the sheet, and the stringer respectively due to the uni-axial force  $S$ .

Equating Equation (2.1a) to Equation (2.1b) and rearranging the equations, the general equation for the unknown rivet forces in the stiffened plate is derived as it is given in Equation (2.2).

$$\sum_j (A_{ij} + A_{ij}^s) Q_j - (B_i - \frac{E_s}{E} B_i^s) S = 0 \text{ for } i = 1, 2, 3, \dots \quad (2.2)$$

Unknown rivet forces  $Q_j$  are determined solving Equation (2.2). After obtaining the unknown rivet forces, the stress intensity factors for the cracked stiffened sheet can be determined by utilizing the Mushkelisvili's equation given in Equation (2.3). The first term in Equation (2.3a) accounts for the SIF due to axial load, and the second term accounts for the contribution of the rivet forces to the stress intensity factor. The stress intensity factors for the symmetrical set of rivet forces shown in Figure 2.2 is calculated from Equation (2.3b).

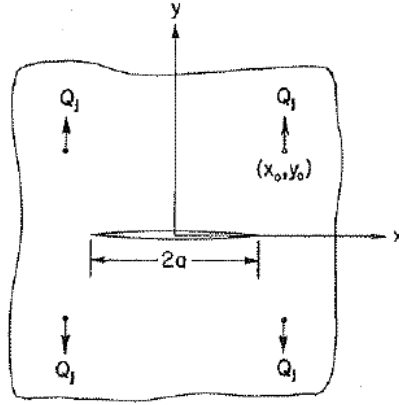


Figure 2.2: Symmetrical rivet forces acting on the cracked sheet [6]

$$K = S \sqrt{\pi a} + \sum_j \bar{K}_j Q_j \quad (2.3a)$$

$$\bar{K} = \frac{\sqrt{\pi a}}{\pi t} [(3 + \nu)\Phi_1 - (1 + \nu)\Phi_2] \quad (2.3b)$$

where,

$$\Phi_1 = \frac{\gamma}{\sqrt{(x_0^2 - y_0^2 - a^2)^2 + 4x_0^2 y_0^2}} \quad (2.3c)$$

$$\Phi_2 = \frac{[(x_0^2 + a^2)y_0^2 + (x_0^2 - a^2)^2] \gamma^2 + x_0^2 y_0^2 (x_0^2 + y_0^2 - a^2)}{\gamma [(x_0^2 - y_0^2 - a^2)^2 + 4x_0^2 y_0^2]^{1.5}} \quad (2.3d)$$

$$\gamma = \frac{1}{\sqrt{2}} \left[ \sqrt{(x_0^2 - y_0^2 - a^2)^2 + 4x_0^2 y_0^2} - (x_0^2 - y_0^2 - a^2) \right]^{0.5} \quad (2.3e)$$



The displacements of the rivets for the broken stiffeners can be written in the form of Equation (2.4).

$$v_i^{bs} = v_1 + \bar{v}_i^{bs} \quad (i = 1, 2, 3, \dots, n) \quad (2.4)$$

where,  $n$  is the number of rivets on the broken stiffener,  $v_i^{bs}$  are displacements of rivet points in the broken stiffener,  $v_1$  is the displacement of the sheet at the first rivet, and  $\bar{v}_i^{bs}$  are displacements of the  $i$ 'th rivet relative to the first rivet.

The displacement  $\bar{v}_i^{bs}$  is expressed in terms of influence coefficients is given in Equation (2.5).

$$\bar{v}_i^{bs} = \sum_{j=2}^n (\bar{A}_{ij}^s Q_j) + \bar{B}_i^s S E_s / E \quad (i = 1, 2, 3, \dots, n) \quad (2.5)$$

$\bar{A}_{ij}^s$  and  $\bar{B}_i^s$  are the influence coefficients for the relative displacements of the desired riveting point with respect to the first rivet point. The derivation of the influence coefficients for the relative displacements are explained in detail in the Section 2.2.5 and Section 2.2.6.

Equating the displacements of the sheet and the stringers at the rivet locations in the same manner as for the intact stringers, and using Equation (2.4) for the broken stiffener, the general equations for the unknown rivet forces becomes Equations (2.6) and (2.7).

$$\sum_{j=2}^n (\bar{A}_{ij} + \bar{A}_{ij}^s) Q_j + \sum_{j=n+1}^N (A_{ij} - A_{1j}) Q_j + \left[ \bar{B}_i^s E_s / E - B_i + B_1 - (A_{i1} - A_{11}) w t_s E_s / E \right] S = 0 \quad i = 2, 3, 4, \dots, n \quad (2.6)$$

$$\sum_{j=2}^n (A_{ij} - A_{1j}) Q_j + \sum_{j=n+1}^N (A_{ij}^s + A_{ij}) Q_j + \left[ B_i^s E_s / E - B_i - A_{i1} w t_s E_s / E \right] S = 0 \quad i = n + 1, n + 2, \dots, N \quad (2.7)$$

It should be noted that for the force equilibrium to be satisfied, the Equation (2.8) should be satisfied for the broken stiffener.

$$\sum_{j=1}^n Q_j + S E_s w t_s / E = 0 \quad (2.8)$$

In the article presented by Poe [7], the modifications are given for two broken stiffeners. However in the Chapter 1 it is explained that for sizing of the aircraft it is critical to satisfy the two bay criteria which brings the need of determining the stress intensity factors for only one broken stiffener. Therefore, the modifications recommended in the Poe's article [7] is re-arranged for the one broken stiffener under the cracked sheet. The equations given in this section and in Section 2.2.5 and Section 2.2.6 can be extended to any number of broken stringers.

## 2.2 Influence Coefficients

In this section derivation of the influence coefficients of the stiffened cracked sheets with intact and broken stiffeners is explained in detail.

### 2.2.1 $A_{ij}$ Coefficient-Displacement at the $i$ th Rivet on the Cracked Sheet due to the Unit Force at the $j$ th Rivet

As explained in Section 2.1.1, stress intensity factor for the infinite size cracked sheet, with crack extending equally on both sides of point midway between two stringers, is determined by superimposing the stress intensity factors calculated for the symmetrically applied rivet forces, shown in part c of Figure 2.4, and for the applied far field stress. The displacements for the cracked sheet with symmetrically applied forces can be obtained by superposing the displacement for the point forces applied to the sheet which has no crack as shown in part a of Figure 2.4, and displacement for the stress which has to be applied at the crack line due to the point forces for the no-crack case. As shown in part c of Figure 2.4, since there is no traction at the crack surface, the stress applied in part b of Figure 2.4 must be in equal magnitude and distribution but in opposite direction to the stress due to symmetrically applied rivet forces shown in part a of Figure 2.4.

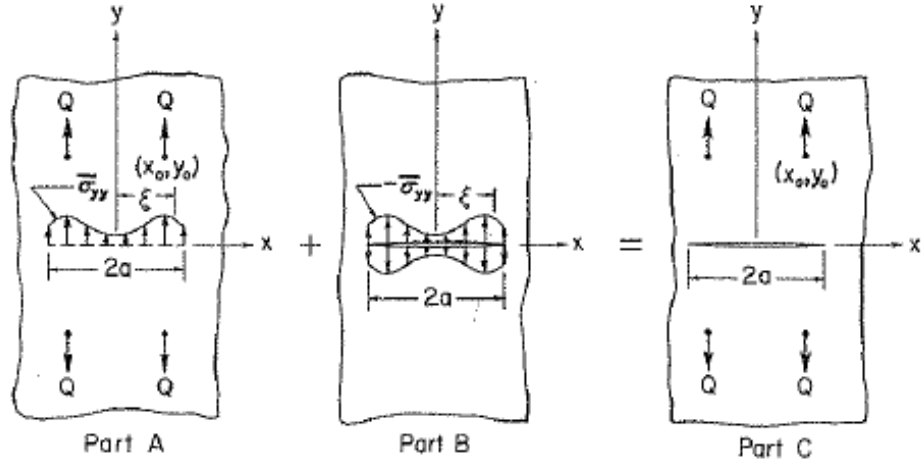


Figure 2.4: Superposition for  $A_{ij}$  Coefficient [6]

Part a of the solution starts with the Love solution for infinite sheets [32], which has a point force at the origin of the infinite sheet.

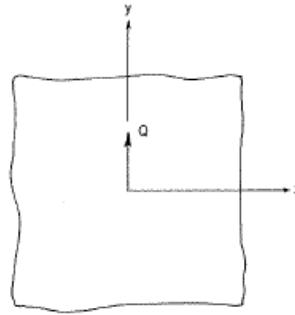


Figure 2.5: Point force at the origin [6]

Firstly, as shown in Figure 2.5, displacements and stresses are obtained from the Love Solution for single point force as:

$$v = -\frac{(1+\nu)Q}{4\pi t E} \left[ \frac{1}{2}(3-\nu) \ln(x^2 + y^2) + (1+\nu) \left( \frac{x^2}{x^2 + y^2} \right) \right] \quad (2.9)$$

$$\sigma_{yy} = -\frac{(1+\nu)Q}{4\pi t} \left( \frac{y}{x^2 + y^2} \right) \left( \frac{3+\nu}{1+\nu} - \frac{2x^2}{x^2 + y^2} \right) \quad (2.10)$$

It is clearly seen from the Equation (2.9) that there is singularity at the origin. Therefore, in order to get rid of the singularity, point force  $Q$  is assumed to be distributed over the rivet diameter uniformly. As shown in Figure 2.6, replacing  $x$  by  $x - \bar{x}$  in Equation (2.9) and

integrating from  $-\frac{1}{2}d$  to  $\frac{1}{2}d$ , Equation (2.12) is obtained. Derivation of the Equation (2.9) and Equation (2.10) is described respectively in Appendix A.3.1 and Appendix A.3.2.

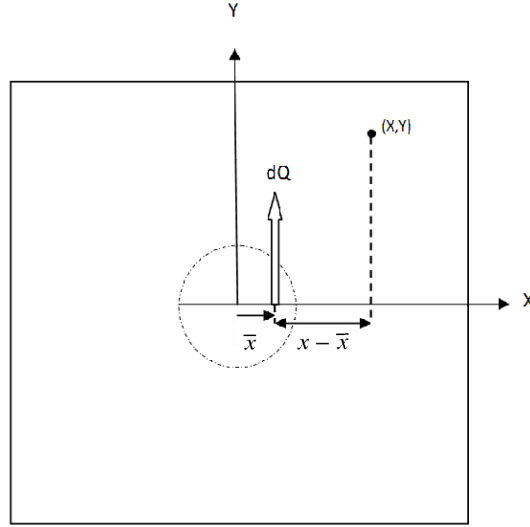


Figure 2.6: Distributing the point rivet force over the rivet diameter

It should be noted since the rivet force  $Q$  is assumed to be distributed uniformly over the rivet diameter, vertical displacement of the sheet is determined by obtaining the displacement due to  $(Q/2d)d\bar{x}$  and integrating with respect to  $\bar{x}$  from  $\bar{x} = -d/2$  to  $\bar{x} = d/2$ .

$$v = -\frac{(1+\nu)Q}{8d\pi tE} \int_{-d/2}^{d/2} \left[ \frac{1}{2}(3-\nu) \ln((x-\bar{x})^2 + y^2) + (1+\nu) \left( \frac{(x-\bar{x})^2}{(x-\bar{x})^2 + y^2} \right) \right] d\bar{x} \quad (2.11)$$

Integrating Equation (2.11), Equation (2.12) is obtained for a single point force which is distributed over the diameter at the origin (0, 0).

$$v = -\frac{(1+\nu)(3-\nu)Q}{16\pi tE} \left\{ \left( \frac{2x}{d} + 1 \right) \ln \left[ \left( \frac{2x}{d} + 1 \right)^2 + \frac{4y^2}{d^2} \right] - \left( \frac{2x}{d} - 1 \right) \ln \left[ \left( \frac{2x}{d} - 1 \right)^2 + \frac{4y^2}{d^2} \right] + \left( \frac{1-\nu}{3-\nu} \right) \left( \frac{8y}{d} \right) \left[ \arctan \frac{\frac{y}{d}}{\frac{x^2}{d^2} + \frac{y^2}{d^2} - \frac{1}{4}} \right] \right\} \quad (2.12)$$

In order to get solution for the case for four point forces shown in Figure 2.2, point forces must be translated to  $(\mp x_0, \mp y_0)$  and displacements due four point forces must be superimposed.

To translate the point forces to  $(\mp x_0, \mp y_0)$   $x$  should be replaced by  $x \mp x_0$  and  $y$  should be replaced by  $y \mp y_0$ . For instance, to translate the first point force from origin to  $(x_0, y_0)$ , in

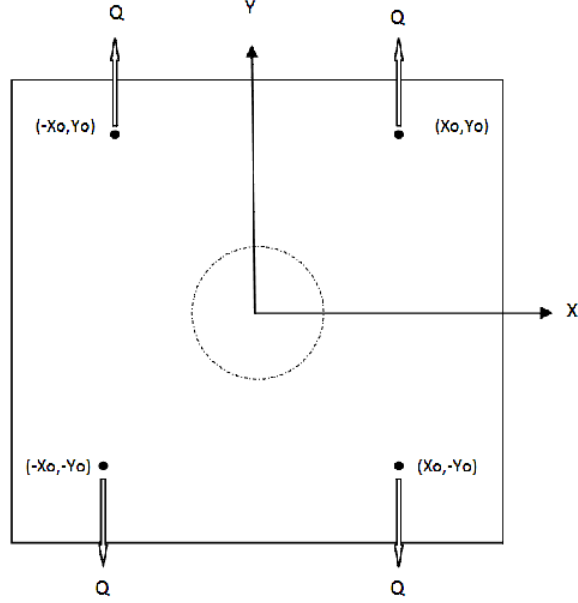


Figure 2.7: Symmetrical four point forces acting on four quadrant

Equation (2.12)  $x$  should be replaced by  $x - x_0$  and  $y$  should be replaced by  $y - y_0$ .

$$v = -\frac{(1-\nu)(3-\nu)Q}{4\pi tE} \left\{ \left[ \frac{2(x-x_0)}{d} + 1 \right] \ln \left[ \left( \frac{2(x-x_0)}{d} + 1 \right)^2 + \frac{4(y-y_0)^2}{d^2} \right] - \left[ \frac{2(x-x_0)}{d} - 1 \right] \ln \left[ \left( \frac{2(x-x_0)}{d} + 1 \right)^2 + \frac{4(y-y_0)^2}{d^2} \right] + \frac{1-\nu}{3-\nu} \left( \frac{8(y-y_0)}{d} \right) \arctan \left[ \frac{\frac{y-y_0}{d}}{\frac{(x-x_0)^2}{d^2} + \frac{(y-y_0)^2}{d^2} - \frac{1}{4}} \right] \right\} \quad (2.13)$$

Finally, after the superposition of the displacements due to four point forces, displacement field for part a of Figure 2.4 can be written as:

$$v_a = \frac{(1+\nu)(3-\nu)Q}{16\pi tE} \Omega \quad (2.14)$$

where,  $\Omega$  is given in Equation (2.15).

$$\begin{aligned}
\Omega = & (\alpha_1 + 1) \ln \left[ \frac{(\alpha_1 + 1)^2 + \alpha_4^2}{(\alpha_1 + 1)^2 + \alpha_3^2} \right] - (\alpha_1 - 1) \ln \left[ \frac{(\alpha_1 - 1)^2 + \alpha_4^2}{(\alpha_1 - 1)^2 + \alpha_3^2} \right] \\
& + (\alpha_2 + 1) \ln \left[ \frac{(\alpha_2 + 1)^2 + \alpha_4^2}{(\alpha_2 + 1)^2 + \alpha_3^2} \right] - (\alpha_2 - 1) \ln \left[ \frac{(\alpha_2 - 1)^2 + \alpha_4^2}{(\alpha_2 - 1)^2 + \alpha_3^2} \right] \\
& + 4 \left( \frac{1 - \nu}{3 - \nu} \right) \left\{ \alpha_4 \left[ \arctan \left( \frac{2\alpha_4}{\alpha_1^2 + \alpha_4^2 - 1} \right) + \arctan \left( \frac{2\alpha_4}{\alpha_2^2 + \alpha_4^2 - 1} \right) \right] \right. \\
& \quad \left. - \alpha_3 \left[ \arctan \left( \frac{2\alpha_3}{\alpha_1^2 + \alpha_3^2 - 1} \right) + \arctan \left( \frac{2\alpha_3}{\alpha_2^2 + \alpha_3^2 - 1} \right) \right] \right\} \quad (2.15)
\end{aligned}$$

The  $\alpha$  coefficients which are used in Equation (2.15) are given by:

$$\begin{aligned}
\alpha_1 &= \frac{2(x - x_0)}{d} \\
\alpha_2 &= \frac{2(x + x_0)}{d} \\
\alpha_3 &= \frac{2(y - y_0)}{d} \\
\alpha_4 &= \frac{2(y + y_0)}{d}
\end{aligned}$$

At this point displacement, in the line of action of the point forces applied, due to four symmetrically placed point forces in an intact sheet is calculated. Following the same procedure and Equation (2.10), stress in part a of Figure 2.4 can be written as in Equation (2.16). The derivation of the Equation (2.14) is included in Appendix A.3.3.

$$\begin{aligned}
\sigma_{yy} = & \frac{(1 + \nu)Q}{\pi t d} \left\{ \frac{1}{2} \left( \frac{1 - \nu}{1 + \nu} \right) \left( \frac{\alpha_4}{\alpha_1^2 + \alpha_4^2} + \frac{\alpha_4}{\alpha_2^2 + \alpha_4^2} - \frac{\alpha_3}{\alpha_1^2 + \alpha_3^2} - \frac{\alpha_3}{\alpha_2^2 + \alpha_3^2} \right) \right. \\
& \left. + \alpha_4 \left[ \left( \frac{\alpha_4}{\alpha_1^2 + \alpha_4^2} \right)^2 + \left( \frac{\alpha_4}{\alpha_2^2 + \alpha_4^2} \right)^2 \right] - \alpha_3 \left[ \left( \frac{\alpha_3}{\alpha_1^2 + \alpha_3^2} \right)^2 + \left( \frac{\alpha_3}{\alpha_2^2 + \alpha_3^2} \right)^2 \right] \right\} \quad (2.16)
\end{aligned}$$

Thus, from the full field stress field, the stresses on the  $y = 0, x = \zeta$  line can be easily determined for the intact sheet. This is the stress  $\bar{\sigma}_{yy}$  that must be removed in part a of Figure 2.4. Substituting  $y = 0, x = \zeta$  in Equation (2.16), Equation (2.17) is obtained, the derivation of the Equation (2.17) is explained in Appendix A.3.4 in detail.

$$\bar{\sigma}_{yy}(\zeta, 0) = \frac{(1 + \nu)Qy_0}{2\pi t} \Gamma \quad (2.17)$$

where,

$$\Gamma = \frac{1-\nu}{1+\nu} \left[ \frac{1}{(\zeta-x_0)^2+y_0^2} + \frac{1}{(\zeta+x_0)^2+y_0^2} \right] + \underbrace{2y_0^2}_{\text{Corrected Exp.}} \left\{ \left[ \frac{1}{(\zeta-x_0)^2+y_0^2} \right]^2 + \left[ \frac{1}{(\zeta+x_0)^2+y_0^2} \right]^2 \right\} \quad (2.18)$$

As shown in the expression for  $\nu$ , the first correction is on the exponent of in the second term of  $\nu$ . In the original report by Poe the exponent is 1 whereas the correct exponent should be 2. It should be noted that without a complete re-derivation of the full set of equations, it would be impossible to identify the error in the expression for  $\nu$ . Derivation of the  $A_{ij}$  coefficient with the sources of errors is explained in Appendix A.3 in detail.

The stress field around  $-a < x < a$  and  $y = 0$  line due to the applied symmetrical forces is known from Equation (2.17). Because the crack faces are traction free, the negative of  $\bar{\sigma}_{yy}$  should be applied to the crack line to get zero traction. Therefore, the displacement due to negative  $\bar{\sigma}_{yy}$  is determined and the resulting displacement is superimposed with the displacement field determined for the non-cracked sheet, as shown in Figure 2.4.

The displacement field due to  $\bar{\sigma}_{yy}$  in part b of Figure 2.4 is determined by making use of the known Westergaard solution for the four point load on the crack surface [13] shown in Figure 2.8.

Equation (2.19) gives the displacement due to four point forces applied on the crack surface case as shown in Figure 2.8 [14].

$$\nu = \frac{1}{E} \left[ 2\Im(\bar{Z}) - (1+\nu)y\Re(Z) \right] \quad (2.19)$$

where  $z = x + \Im(y)$ ,  $\bar{Z}$  is the first integral of the  $Z$ , and  $Z$  is the complex function given by Equation (2.20) [13].

$$Z = \frac{2Pz}{\pi t(z^2 - \zeta^2)} \sqrt{\frac{a^2 - \zeta^2}{z^2 - a^2}} \quad (2.20)$$

Substituting Equation (2.20) into Equation (2.19), Equation (2.21) is derived.

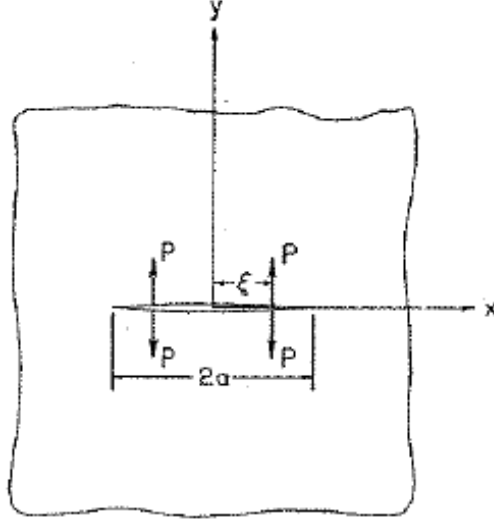


Figure 2.8: Westergaard solution for symmetrical four point forces applied on the crack surface [6]

$$v = \frac{P}{\pi t E} \Lambda \quad (2.21)$$

where,

$$\Lambda = \ln \left( \frac{a^2 - \zeta^2 + 2\sqrt{a^2 - \zeta^2} \sqrt{C_1 + C_2} + 2C_2}{a^2 - \zeta^2 - 2\sqrt{a^2 - \zeta^2} \sqrt{C_1 + C_2} + 2C_2} \right) - \frac{(1 + \nu)y \sqrt{a^2 - \zeta^2}}{C_2} \left( \frac{x(x^2 + y^2 - \zeta^2) \sqrt{C_2 - C_1} - y(x^2 + y^2 + \zeta^2) \sqrt{C_1 + C_2}}{(x^2 - y^2 - \zeta^2)^2 + 4x^2y^2} \right) \quad (2.22)$$

where,

$$C_1 = \frac{1}{2}(a^2 + y^2 - x^2)$$

$$C_2 = \sqrt{C_1^2 + x^2y^2}$$

The displacement equation for four point load is derived, but for the real problem, the displacement for the  $\bar{\sigma}_{yy}$  is needed. Therefore, in Equation (2.21) point load is replaced by  $t\bar{\sigma}_{yy}d\epsilon$  as shown in Figure 2.9 and by making use of the Westergaard solution for the four point load applied on the crack surface, and using Equation (2.17), Figure 2.9 is derived.

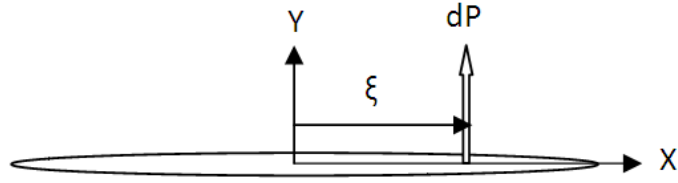


Figure 2.9: Distributing the point load so as to simulate the  $\overline{\sigma}_{yy}$  on Figure 2.4

$$\begin{aligned}
 dP &= t\overline{\sigma}_{yy}(\zeta, 0)d\zeta \\
 v_B &= \frac{1}{\pi E} \int_0^a \overline{\sigma}_{yy}(\zeta, 0)\Lambda d\zeta \\
 v_B &= \frac{(1+\nu)Qy_0}{2\pi^2 tE} \int_0^a \Lambda\Gamma d\zeta
 \end{aligned} \tag{2.23}$$

By adding the displacements of the parts a and b in Figure 2.4, displacement of part c of Figure 2.4 is obtained. Thus, for a cracked sheet with symmetrically applied point forces, the displacement and the influence coefficients  $A_{ij}$  for unit load  $Q$  is given by Equation (2.25).

$$v_B = \frac{(1+\nu)Q}{16\pi tE} \left\{ (3-\nu)\Omega + \frac{8y_0}{\pi} \int_0^a \Lambda\Gamma d\zeta \right\} \tag{2.24}$$

$$A_{ij} = \frac{(1+\nu)}{16\pi tE} \left\{ (3-\nu)\Omega + \frac{8y_0}{\pi} \int_0^a \Lambda\Gamma d\zeta \right\} \tag{2.25}$$

At this point, it should be noted that there is also an alternative way to determine the displacements and stress intensity factor for the cracked sheet with symmetrically applied point forces using the Equation (2.26), which is described in the article of Westergaard [14]. The complex functions which are needed for the Westergaard formulation is provided from the Cracks Handbook [13].

$$v = \frac{1}{2\mu} \left\{ \frac{\kappa+1}{2} \Im\bar{Z} - y\Re Z \right\} \tag{2.26}$$

where,

$$\kappa = \begin{cases} (3 - \nu)/(1 + \nu) & \text{Plane stress} \\ 3 - 4\nu & \text{Plane strain} \end{cases}$$

$$\mu = \frac{E}{2(1 + \nu)}$$

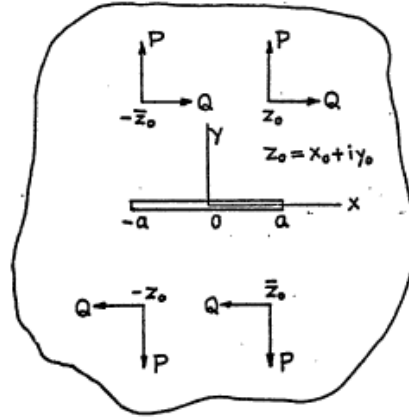


Figure 2.10: Cracks Handbook Formulation for symmetrical four point forces acting on a cracked sheet [13]

$$Z_I(z) = \frac{1}{\pi} P \left[ 1 - \alpha y_0 \frac{\partial}{\partial y_0} \right] \left\{ \left( \frac{\sqrt{a^2 - z_0^2}}{z^2 - z_0^2} + \frac{\sqrt{a^2 - \bar{z}_0^2}}{z^2 - \bar{z}_0^2} \right) \frac{1}{\sqrt{1 - (a/z)^2}} - q(z, z_0, \bar{z}_0) \right\} \quad (2.27a)$$

$$\bar{Z}_I(z) = \frac{1}{\pi} P \left[ 1 - \alpha y_0 \frac{\partial}{\partial y_0} \right] \left\{ \arctan \sqrt{\frac{z^2 - a^2}{a^2 - z_0^2}} + \arctan \sqrt{\frac{z^2 - a^2}{a^2 - \bar{z}_0^2}} - \left( \arctan \mathfrak{I} \frac{z}{z_0} - \arctan \mathfrak{I} \frac{z}{\bar{z}_0} \right) \right\} \quad (2.27b)$$

$$K_I = \frac{1}{\sqrt{\pi a}} P \left[ 1 - \alpha y_0 \frac{\partial}{\partial y_0} \right] \left\{ \frac{a}{\sqrt{z^2 - z_0^2}} + \frac{a}{\sqrt{z^2 - \bar{z}_0^2}} \right\} \quad (2.27c)$$

$$q(z, z_0, \bar{z}_0) = \frac{1}{\mathfrak{I}} \left( \frac{z_0}{z^2 - z_0^2} - \frac{\bar{z}_0}{z^2 - \bar{z}_0^2} \right) \quad (2.27d)$$

where,

$$\alpha = \begin{cases} \frac{1}{2}(1 + \nu) & \text{Plane stress} \\ \frac{1}{2}\left(\frac{1}{1-\nu}\right) & \text{Plane strain} \end{cases}$$

It is clearly seen that, the Equations (2.27a) and (2.27b) are singular at the origin, therefore, again the same procedure should be followed and point loads should be distributed over the crack length.

### 2.2.2 $A_{ij}^s$ Coefficient-Displacement at the $i$ th Rivet on the Stiffener due to the Unit Force at the $j$ th Rivet

According to Poe [6], the stiffener with the finite width can be approximated by the infinite sheet subjected to equal spaced loading  $Q$  as shown in Figure 2.11. The only boundary condition that is not satisfied is  $\sigma_{xx} = 0$  along  $x = \mp w/2$ .

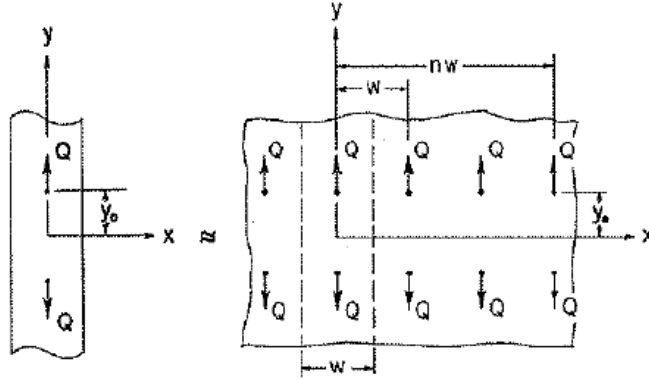


Figure 2.11: Approximating a finite width stringer by an infinite size sheet [6]

The displacement at a rivet location  $y$  due to the rivet force  $Q$  applied at  $y_0$  is obtained by superimposing Equation (2.14) for  $(\mp nw, \mp y_0)$ . However, it should be noted that since Equation (2.14) is valid for four equally spaced point forces, the term for  $x = 0$  in the series summation should be divided by two since there are only two point forces. Superimposing Equation (2.14) for  $(\mp nw, \mp y_0)$ , after manipulation, yields Equation (2.28).

$$v = \frac{(1 + \nu)(3 - \nu)Q}{8\pi t_s E_s} \sum_{n=0}^{\infty} \Psi_n \quad (2.28)$$

where,

$$\Psi_0 = \ln\left(\frac{1 + \alpha_4^2}{1 + \alpha_3^2}\right) + 2\left(\frac{1 - \nu}{3 - \nu}\right)\left[\alpha_4 \arctan\left(\frac{2\alpha_4}{\alpha_4^2 - 1}\right) - \alpha_3 \arctan\left(\frac{2\alpha_3}{\alpha_3^2 - 1}\right)\right] \quad (2.29)$$

$$\begin{aligned} \Psi_n = & \left(1 - \frac{2nw}{d}\right) \ln\left[\frac{\left(1 - \frac{2nw}{d}\right)^2 + \alpha_4^2}{\left(1 - \frac{2nw}{d}\right)^2 + \alpha_3^2}\right] + \left(1 + \frac{2nw}{d}\right) \ln\left[\frac{\left(1 + \frac{2nw}{d}\right)^2 + \alpha_4^2}{\left(1 + \frac{2nw}{d}\right)^2 + \alpha_3^2}\right] \\ & + \underbrace{\text{Corr. Exp.}}_4 * \left(\frac{1 - \nu}{3 - \nu}\right) \left\{ \alpha_4 \arctan \frac{2\alpha_4}{\left(\frac{2nw}{d}\right)^2 + \alpha_4^2 - 1} - \alpha_3 \arctan \frac{2\alpha_3}{\left(\frac{2nw}{d}\right)^2 + \alpha_3^2 - 1} \right\} \quad (2.30) \end{aligned}$$

In Equation (2.30) the second major correction is shown. The 4 factor in Equation (2.30) is missing in the report by Poe [6]. The derivation of the  $A_{ij}^s$  coefficient and the sources of errors is explained in Appendix A.2 in detail. It should be noted that without the corrections presented in this chapter, it is not possible to reproduce the normalized stress intensity versus crack length curves that are given in the appendix of the report by Poe. It should also be noted that with the corrected expressions stress intensity versus crack length data can be obtained for any stiffened crack sheet configuration such as for any stringer pitch, rivet pitch, ratio of total stringer stiffness to total panel stiffness.

### 2.2.3 $B_i$ Coefficient-Displacement on the Cracked Sheet at the $i$ 'th Rivet due to the Uni-axial Loading

In this section the displacement on the cracked sheet due to uni-axial loading is presented. Figure 2.12 shows the cracked sheet subject to uni-axial loading.  $B_i$  coefficient is defined as the displacement at the  $i$ 'th rivet location due to unit uni-axial load  $S$ .

Using the Stanford complex function [33] and Westergaard method [14], the displacement for the cracked sheet exposed to uni-axial loading can be derived. Equation (2.31) gives the displacement in the cracked sheet due to a uni-axial stress  $S$ , and Equation (2.32) gives the  $B_i$  coefficient which is displacement on the cracked sheet due to unit value of the uni-axial stress.

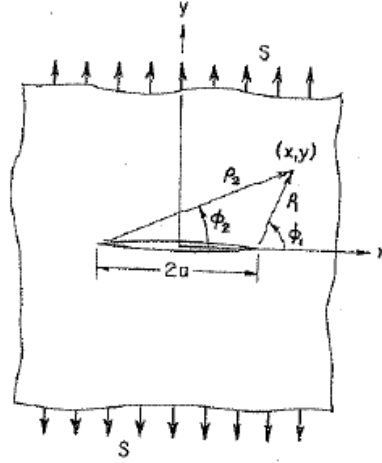


Figure 2.12: Cracked sheet subject to uni-axial loading [6]

$$v = \frac{S}{E} \left[ 2 \sqrt{\rho_1 \rho_2} \sin\left(\frac{\Phi_1 + \Phi_2}{2}\right) - y - (1 + \nu) \frac{y}{\sqrt{\rho_1 \rho_2}} \left( x \cos\left(\frac{\Phi_1 + \Phi_2}{2}\right) + y \sin\left(\frac{\Phi_1 + \Phi_2}{2}\right) - \sqrt{\rho_1 \rho_2} \right) \right] \quad (2.31)$$

$$B_i = \frac{1}{E} \left[ 2 \sqrt{\rho_1 \rho_2} \sin\left(\frac{\Phi_1 + \Phi_2}{2}\right) - y - (1 + \nu) \frac{y}{\sqrt{\rho_1 \rho_2}} \left( x \cos\left(\frac{\Phi_1 + \Phi_2}{2}\right) + y \sin\left(\frac{\Phi_1 + \Phi_2}{2}\right) - \sqrt{\rho_1 \rho_2} \right) \right] \quad (2.32)$$

where  $\rho_1, \rho_2, \Phi_1, \Phi_2$  are given by:

$$\rho_1 = \sqrt{(x - a)^2 + y^2} \quad \phi_1 = \arctan\left(\frac{y}{x - a}\right) \quad (2.33)$$

$$\rho_2 = \sqrt{(x + a)^2 + y^2} \quad \phi_2 = \arctan\left(\frac{y}{x + a}\right) \quad (2.34)$$

The derivation of the  $B_i$  influence coefficient is derived in Appendix A.1, using the Westergaard approach described in the article Bearing Pressures and Cracks [14] with Stanford Function which is quoted from the ME-583 lecture notes [33].

### 2.2.4 $B_i^s$ Coefficient-Displacement on the Stiffener at the $i$ 'th Rivet due to the Uni-axial Loading

The  $y$  displacement on the stiffeners due to applied uni-axial stress  $S * E_s/E$  as shown in Figure 2.13 is given by the Equation (2.35).

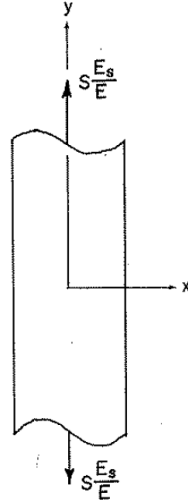


Figure 2.13: Displacement of the stiffener under uni-axial loading [6]

$$v = \frac{S y}{E} \quad (2.35)$$

The influence coefficients  $B_i^s$  are determined from Equation (2.35) by setting  $S * E_s/E = 1$ .

$$B_i^s = \frac{y}{E_s} \quad (2.36)$$

### 2.2.5 $\bar{A}_{ij}^s$ Coefficient-Displacement at the $i$ th Rivet on the Broken Stiffener due to the Unit Force at the $j$ th Rivet

$\bar{A}_{ij}^s$  is the influence coefficient which defines the displacement at the  $i$ 'th rivet location due to a unit force applied at the  $j$ 'th rivet relative to the first rivet. Figure 2.14 shows the superposition applied to determine the influence coefficient  $\bar{A}_{ij}^s$ . It is seen from the Figure 2.14 that, relative displacement in the broken stiffener can be approximated as the superposition of the displacements in parts a and b of Figure 2.14. Thus, the influence coefficient  $\bar{A}_{ij}^s$  can be expressed with Equation (2.37).

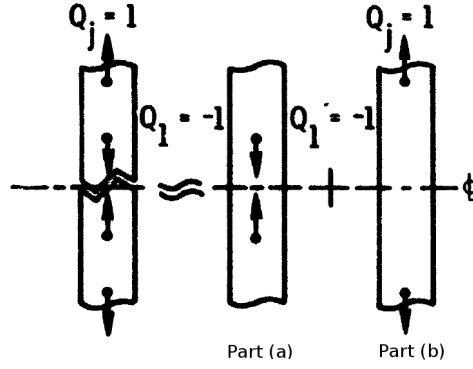


Figure 2.14: Superposition for  $\bar{A}_{ij}^s$  Coefficient [7]

$$\text{Figure 2.14 Part (b)} \quad \text{Figure 2.14 Part (a)}$$

$$\bar{A}_{ij}^s = \overbrace{(A_{ij}^s - A_{1j}^s)} - \overbrace{(A_{i1}^s - A_{11}^s)} \quad (2.37)$$

### 2.2.6 $\bar{B}_i^s$ Coefficient

$\bar{B}_i^s$  is the influence coefficient which defines the displacement at the  $i$ 'th rivet location, due to the unit axial stress applied, relative to the first rivet. Figure 2.15 shows the superposition applied to determine the influence coefficient  $\bar{B}_i^s$ .

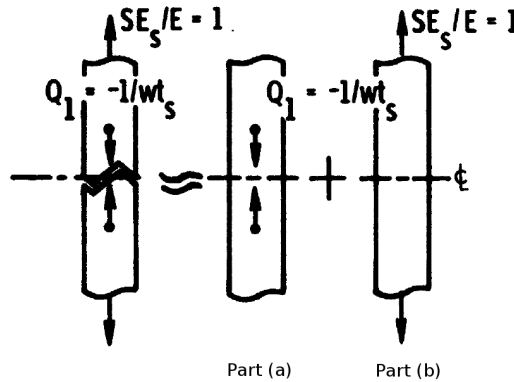


Figure 2.15: Superposition for  $\bar{B}_i^s$  Coefficient [7]

From Figure 2.15 it is seen that relative displacement in the broken stiffener can be approximated as the superposition of the displacements in parts a and b of Figure 2.15. Thus, the influence coefficient  $\bar{B}_i^s$ , due to unit axial stress, can be expressed as as in the Equation (2.38).

$$\text{Figure 2.15 Part (b)} \quad \text{Figure 2.15 Part (a)}$$

$$\bar{B}_i^s = \overbrace{(B_i^s - B_1^s)} - \overbrace{(wt_s A_{i1}^s - wt_s A_{11}^s)} \quad (2.38)$$

### 2.3 Results of the analytical solution

The effect of the two major corrections, described in the previous sections, is demonstrated in Figure 2.16 which shows the variation of the total normalized stress intensity factor  $K_N$  with the ratio of the crack length  $a$  to the stringer pitch  $b$ . Stress intensity factors are calculated for different rivet pitch  $p$  to stringer pitch  $b$  ratios and for different total stringer stiffness  $wtsE_s$  to total panel stiffness  $(wtsE_s + btE)$  ratios denoted by  $\mu$ . Calculations are performed for a Poisson's ratio of 0.3 for both stringer and the sheet which are assumed to be made of Aluminum. In Figure 2.16, continuous curves give the correct  $K_N$  values, and dotted curves give the  $K_N$  values which are calculated by the expressions given in the report by Poe [6]. Figure 2.16 clearly shows that the effect of corrections on the normalized stress intensity factor is very significant. Thus, with the corrected expressions it is possible to produce stress intensity factor curves for any combination of rivet pitch, stringer spacing and ratio of total stringer stiffness to total panel stiffness.

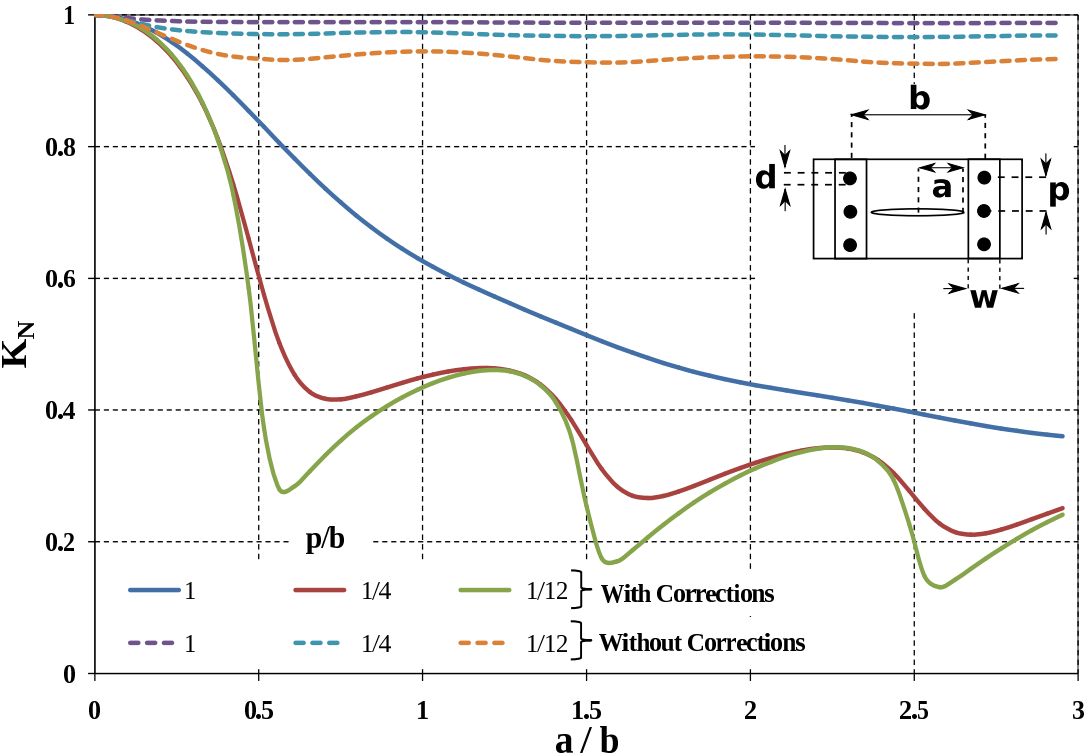


Figure 2.16: Normalized stress intensity factor vs crack length,  $\mu = 1$

### 2.3.1 Variation of stress intensity factor for different crack configurations

In this section, variation of normalized stress intensity factor with the cracked length is presented for different stiffened cracked sheet configurations, and comparisons are made. Results are presented in Figures 2.17 to 2.19 where the vertical red lines denote the stiffener positions, and crack is assumed to exist at  $a/b = 0$ .

The *configuration one*, as shown in Figure 2.17 is the central crack configuration which has an origin at  $a/b = 0$  in between the two intact stiffeners. In real engineering applications, although this case is not the most critical, it is still referenced in the technical notes of Airbus Company.

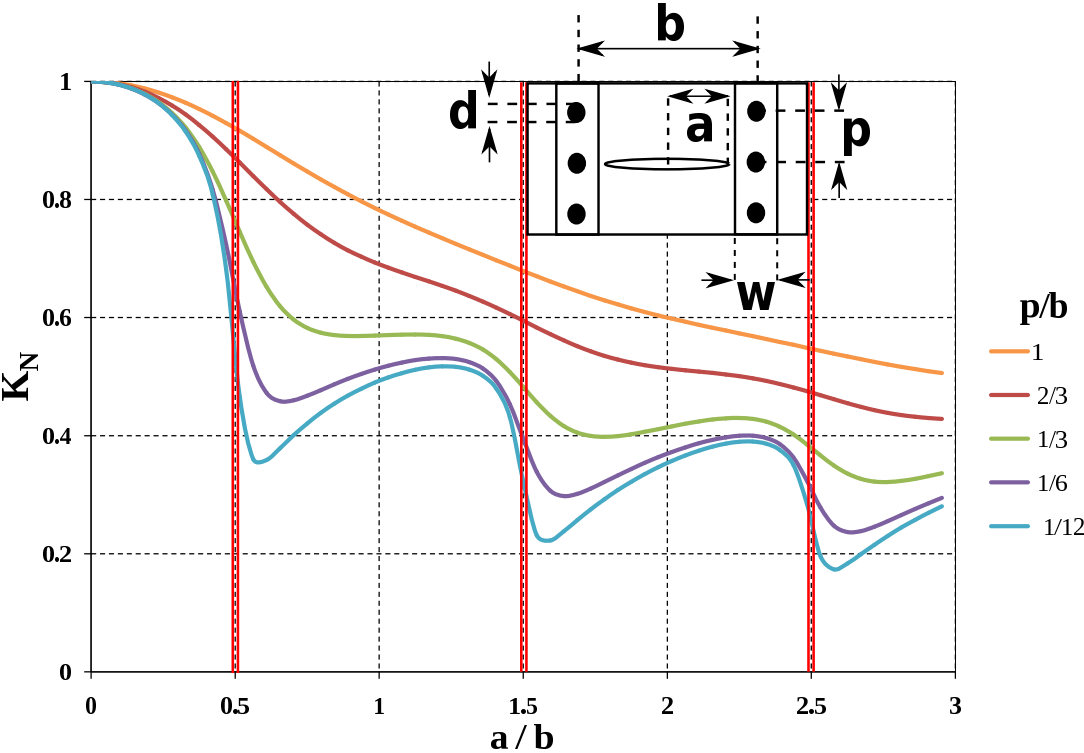


Figure 2.17: Normalized stress intensity factor for the crack between two intact stiffeners,  $\mu = 0.5, d/p = 0.25$

The *configuration two* as shown in Figure 2.18 is the central crack configuration where the crack originates under the intact stiffener. In this configuration, although the sheet under the stiffener is cracked, it is assumed the stiffener remains intact during the crack growth. Again, in real engineering applications this case is not the most critical case.

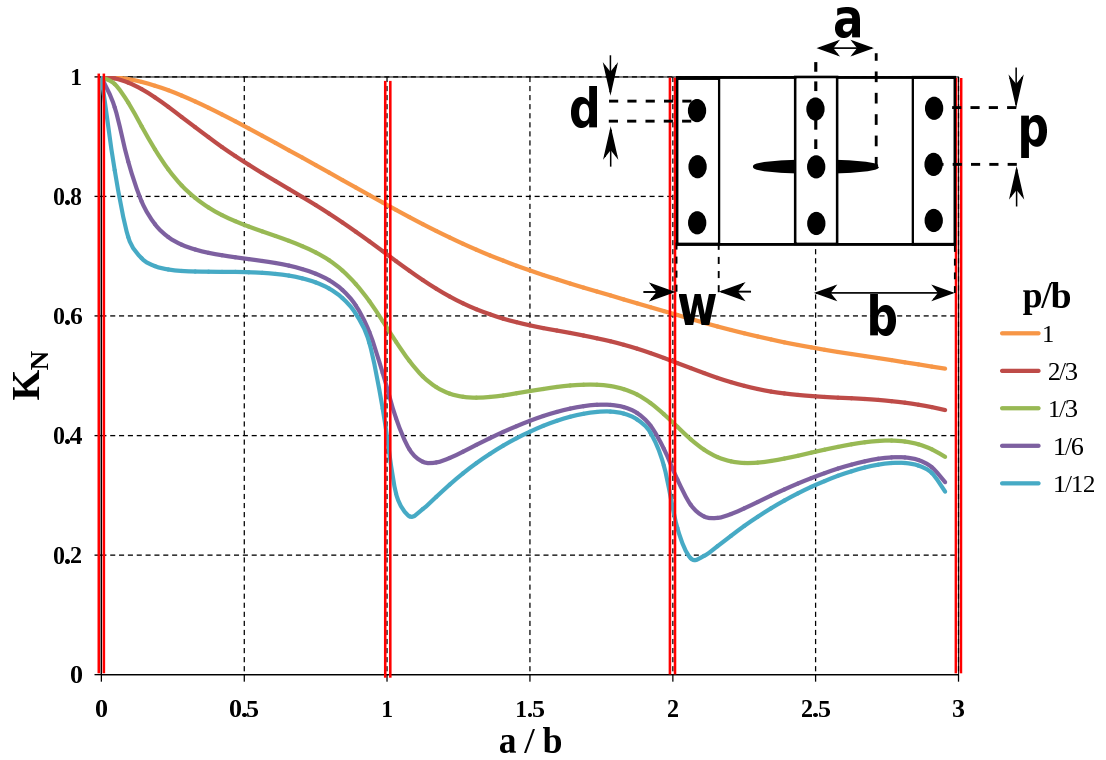


Figure 2.18: Normalized stress intensity factor for the crack under intact stiffener,  $\mu = 0.5$ ,  $d/p = 0.25$

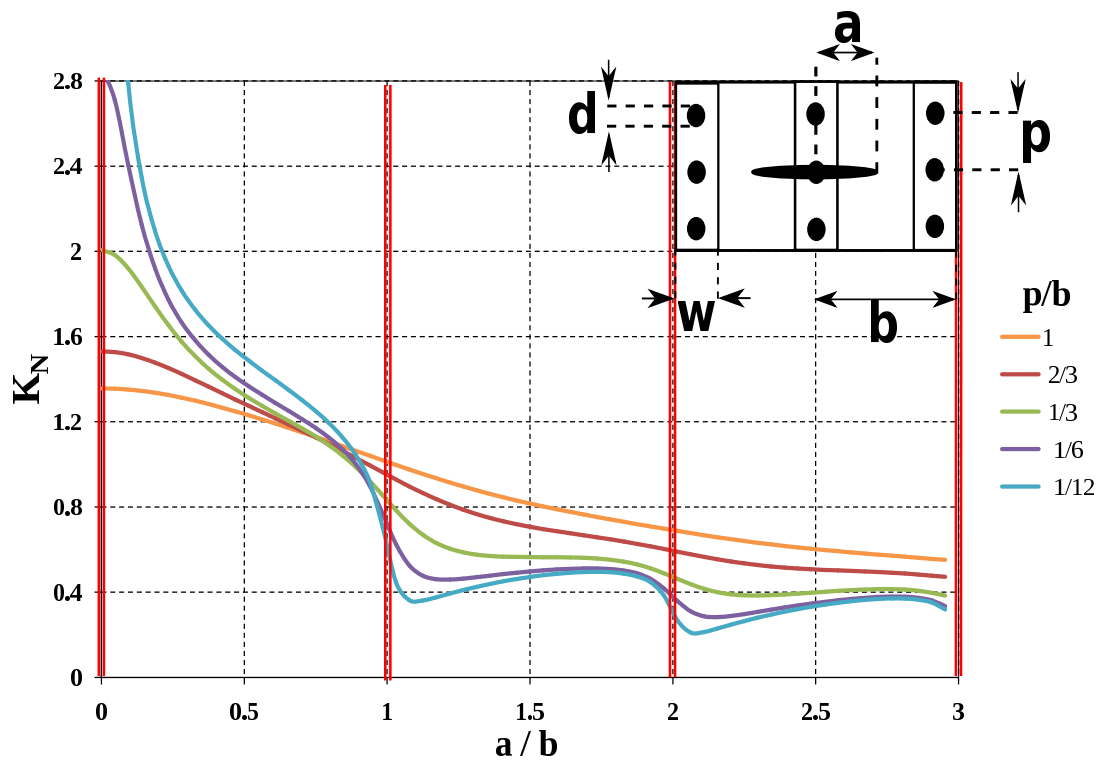


Figure 2.19: Normalized stress intensity factor for the crack under broken stiffener,  $\mu = 0.5$ ,  $d/p = 0.25$

The *configuration three* as illustrated in Figure 2.19 is the most critical case for the stiffened panels for the single crack case. This case corresponds to the crack under the broken stiffener. This is the most critical case, because when the stiffener is broken there is no structure to support the sheet anymore. Moreover, stiffener also forces the crack to propagate, and as a result of this the crack growth speed increases considerably. In the inspection and maintenance, some of the aircraft companies treats the crack under intact stiffener case as the crack under broken stiffener, because this is the most critical scenario for the stiffened panels. It should also be noted that sometimes inspection of the stiffener under the sheet can be hard

Figures 2.17 to 2.19 give the variation of the normalized stress intensity factor with the ratio of the crack length  $a$  to stringer pitch  $b$  for different rivet pitch  $p$  to stringer pitch  $b$  ratios. Stress intensity factor curves are produced by the analytical relations all of which are re-derived and summarized in this chapter. For the three crack configurations given in Figures 2.17 to 2.19, the total stringer stiffness ( $wtsEs$ ) to total panel stiffness ( $wtsEs + btE$ ) ratio, which is denoted by  $\mu$  is taken as 0.5, and the ratio of the rivet diameter  $d$  to rivet pitch  $p$  is taken as 0.25. Calculations are performed for a Poisson's ratio of 0.3 for both stringer and the sheet which are assumed to be made of Aluminum.

### 2.3.2 Variation of $K_N$ with the normalized crack length $a/b$

Figures 2.17 to 2.19 show that normalized stress intensity factor decreases as the crack propagates for all rivet and stringer configurations. It is also observed that when the crack tip approaches to the stiffener  $K_N$  starts to decrease, and when the crack tip passes the stiffener the  $K_N$  starts to increase. When the crack tip approaches to the stiffener, it gets closer to the rivets, which exert a force to close the crack. Therefore, rivets close to the crack tip has a stress relieving effect which results in decrease in  $K_N$ .

### 2.3.3 The effect of the rivet pitch to stringer pitch $p/b$ on $K_N$

Looking at the Figures 2.17 to 2.19 one can deduce that, with increasing  $p/b$ ,  $K_N$  also increases as expected. For large values of  $p/b$ , a steady decrease of  $K_N$  is observed, whereas, when the rivet pitch is decreased,  $K_N$  starts to fluctuate, as it can be seen clearly for low values of  $p/b$  in Figures 2.17 to 2.19. For large values of rivet pitch to stringer pitch ratio, rivet

forces cause a steady decrease in  $K_N$  because crack tip is farther away from the closest rivet. On the other hand, there is not a steady decrease of  $K_N$  when  $p/b$  is decreased. For small values of  $p/b$ ,  $K_N$  starts to show wavy behavior, and  $K_N$  increases when the crack moves away from a stringer. This is because, since rivets are closer to the crack tip, rivet forces are more influential on the crack tip stresses and stringer can support the sheet better. Therefore, when the crack moves away from a stringer, normalized stress intensity factor increases because of the increase in stress in the vicinity of the crack tip.

### 2.3.4 The effect of the *Stiffness Ratio* on $K_N$

This section presents the stiffness ratio effect on the normalized stress intensity factor for all configurations. Figures 2.20 to 2.23 show the influence of the stiffness ratio on the normalized stress intensity factor for configuration one, which is the central crack in between two intact stiffener case. From Figures 2.20 to 2.23, it can be deduced that with increasing stiffness ratio, in other words as the stiffener gets stiffer, the stress intensity factor tends to decrease, as expected.

Figure 2.20 shows the case for which the stiffness ratio is zero which implies that there is no stiffener, and stiffness ratio is the lowest. For this case, it is seen that for all  $p/b$  ratios,  $K_N$  asymptotically approaches its limit value of one. On the other hand, as shown in Figure 2.23, for the largest stiffness ratio of one,  $K_N$  values are the lowest among the configurations that have the same  $p/b$  ratios.

The variation of the normalized stress intensity factor with the crack length for different stiffness ratios are all compared in Figure 2.28 for a  $p/b$  ratio of 1/12. Figure 2.28 shows that as  $\mu$  approaches zero, which means there is no stiffener,  $K_N$  approaches to its asymptotic value of one. As  $\mu$  approaches one, which means that stiffener is infinitely stiff,  $K_N$  has the minimum value as it is seen in Figure 2.28.

For configuration two, the behavior of the curves are the same as the ones in configuration one. As the stiffness ratio increases,  $K_N$  tends to decrease, and again the normalized stress intensity factor approaches to the bounding values for for  $\mu = 0$  and  $\mu = 1$ .

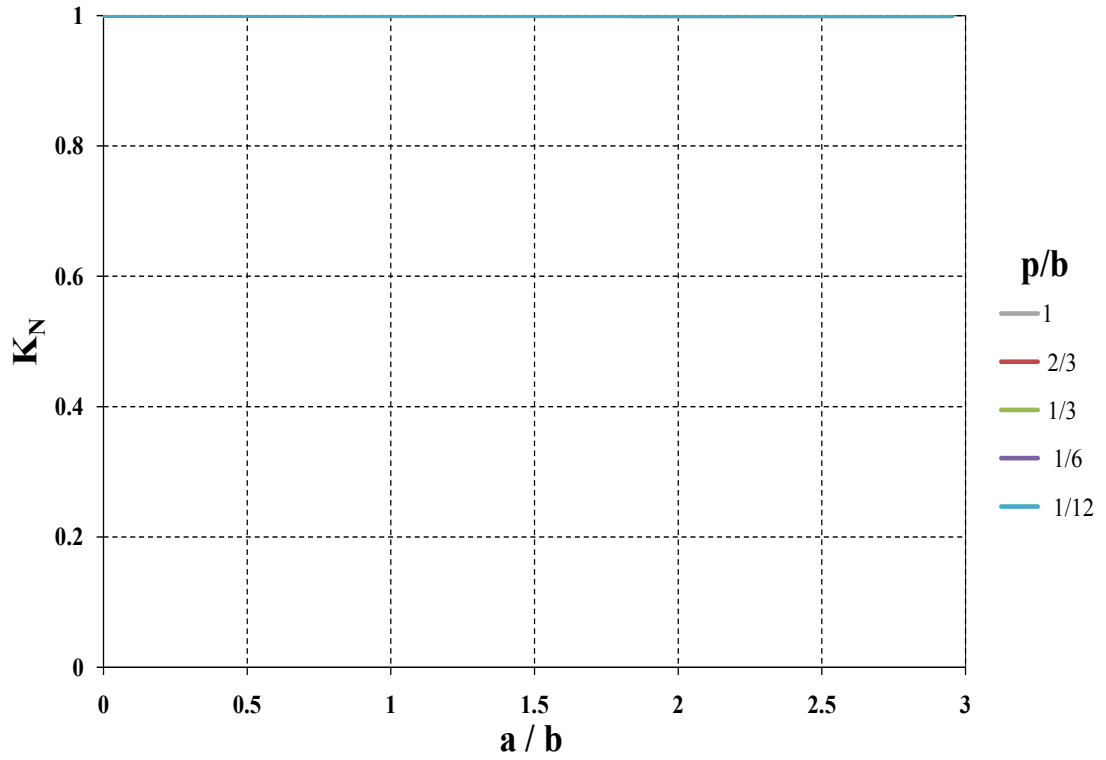


Figure 2.20: Configuration one,  $\mu = 0$

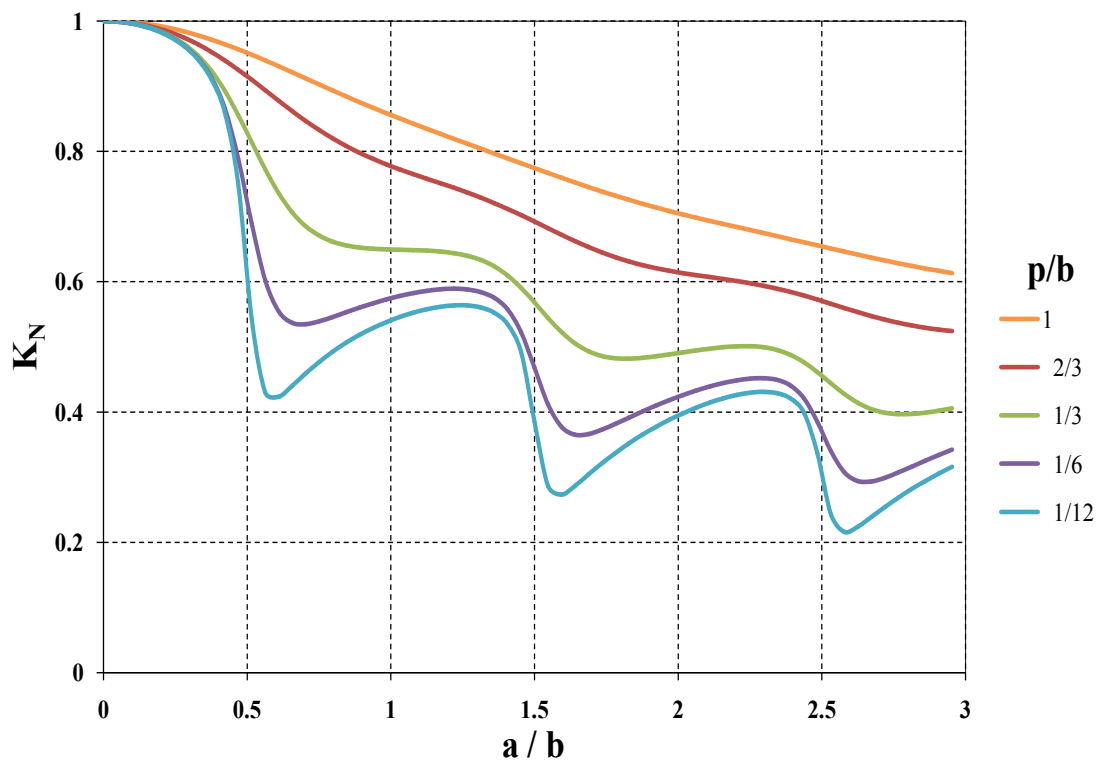


Figure 2.21: Configuration one,  $\mu = 0.3$

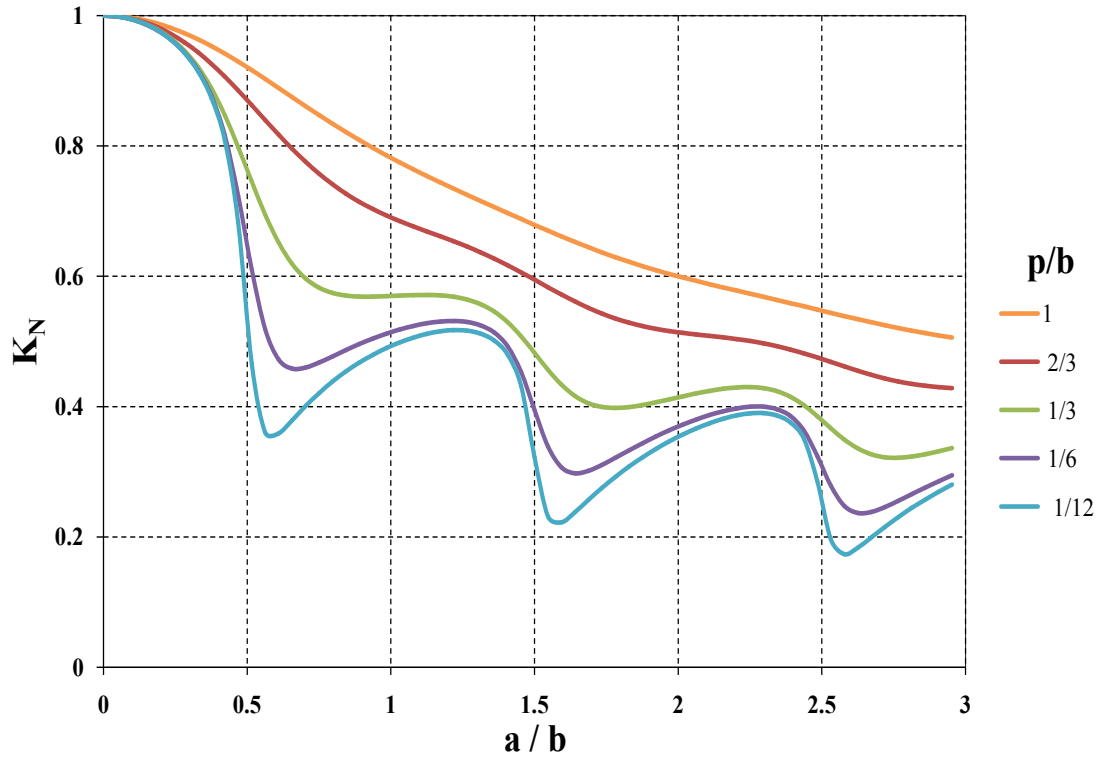


Figure 2.22: Configuration one,  $\mu = 0.5$

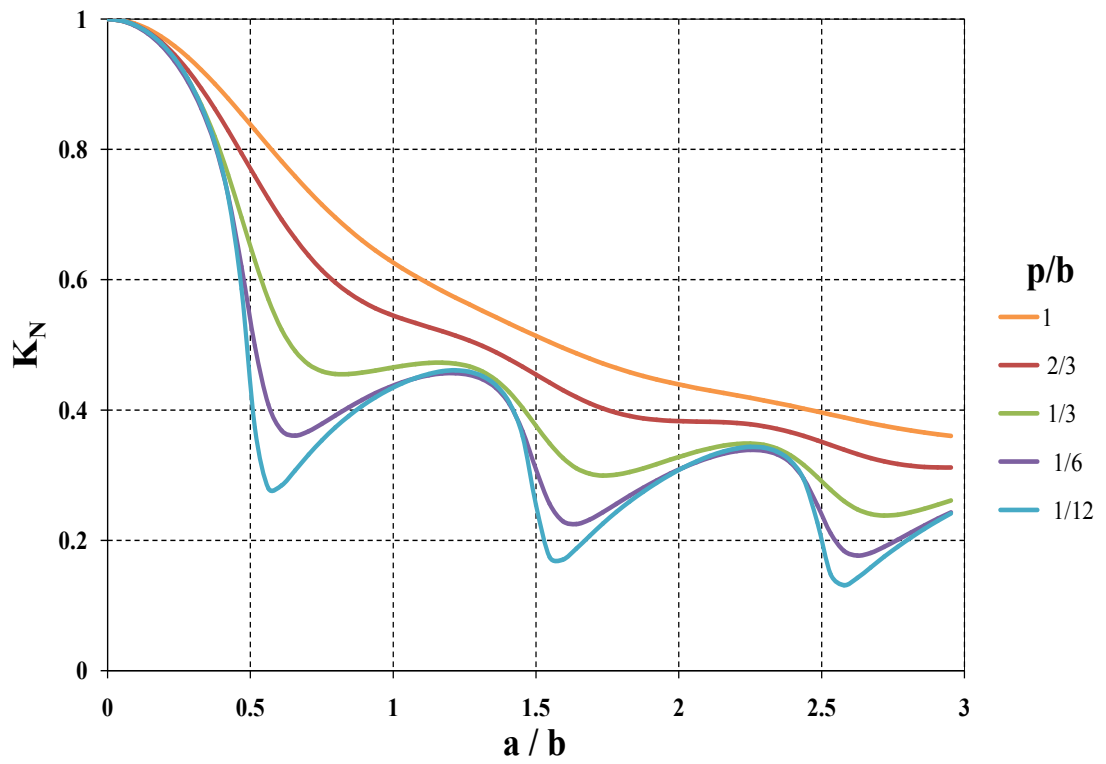


Figure 2.23: Configuration one,  $\mu = 1$

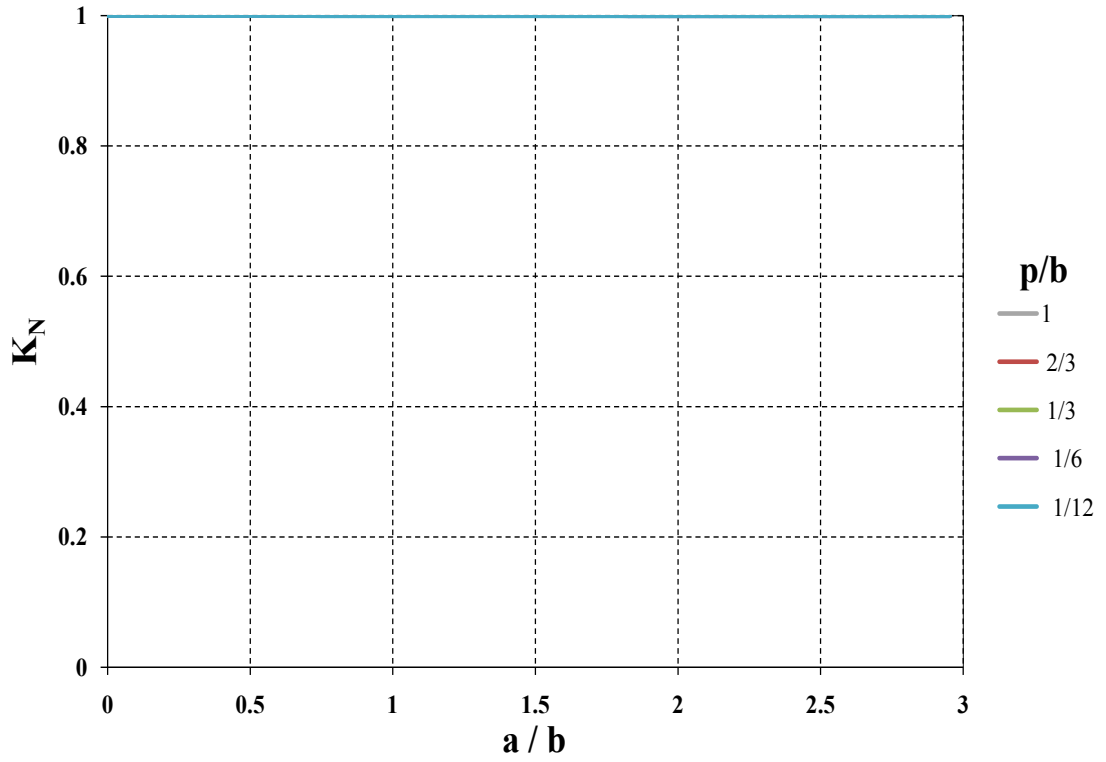


Figure 2.24: Configuration three,  $\mu = 0$

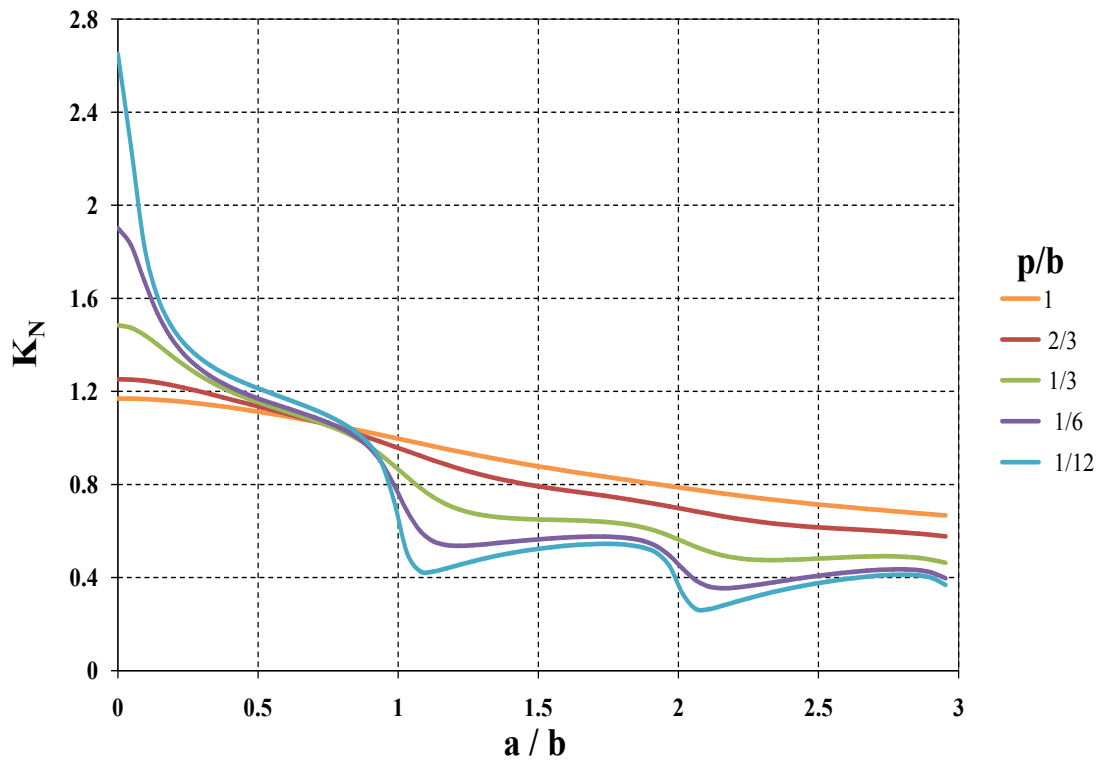


Figure 2.25: Configuration three,  $\mu = 0.3$

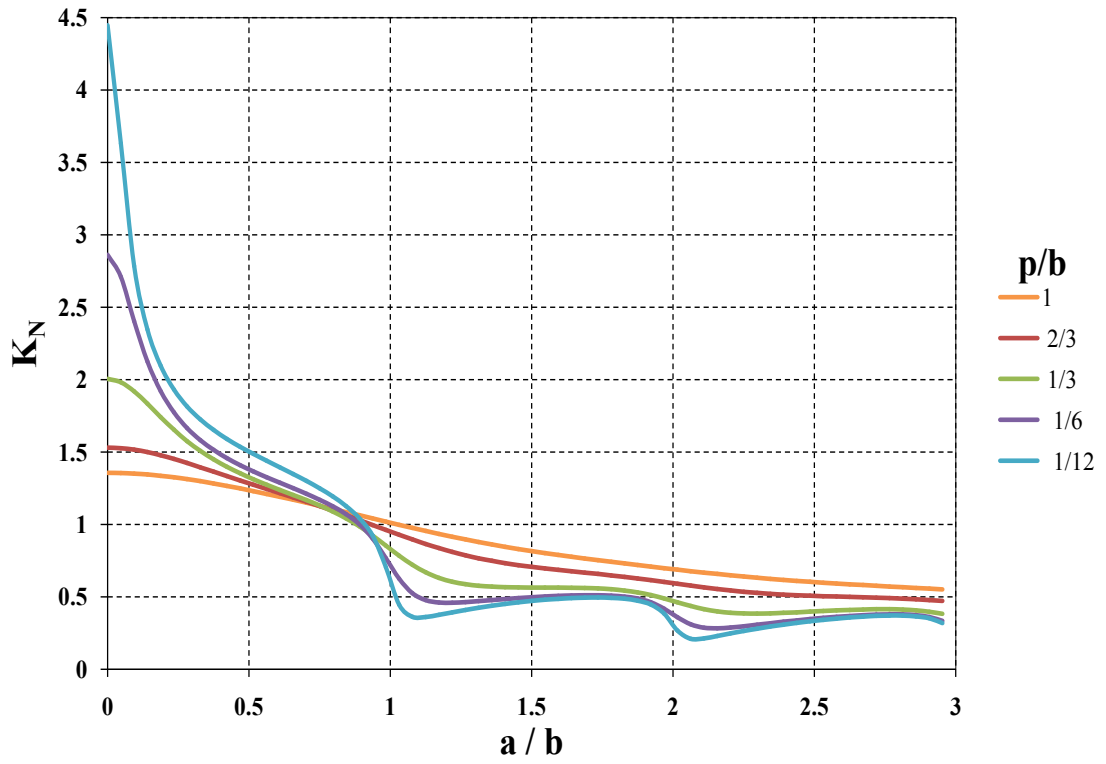


Figure 2.26: Configuration three,  $\mu = 0.5$

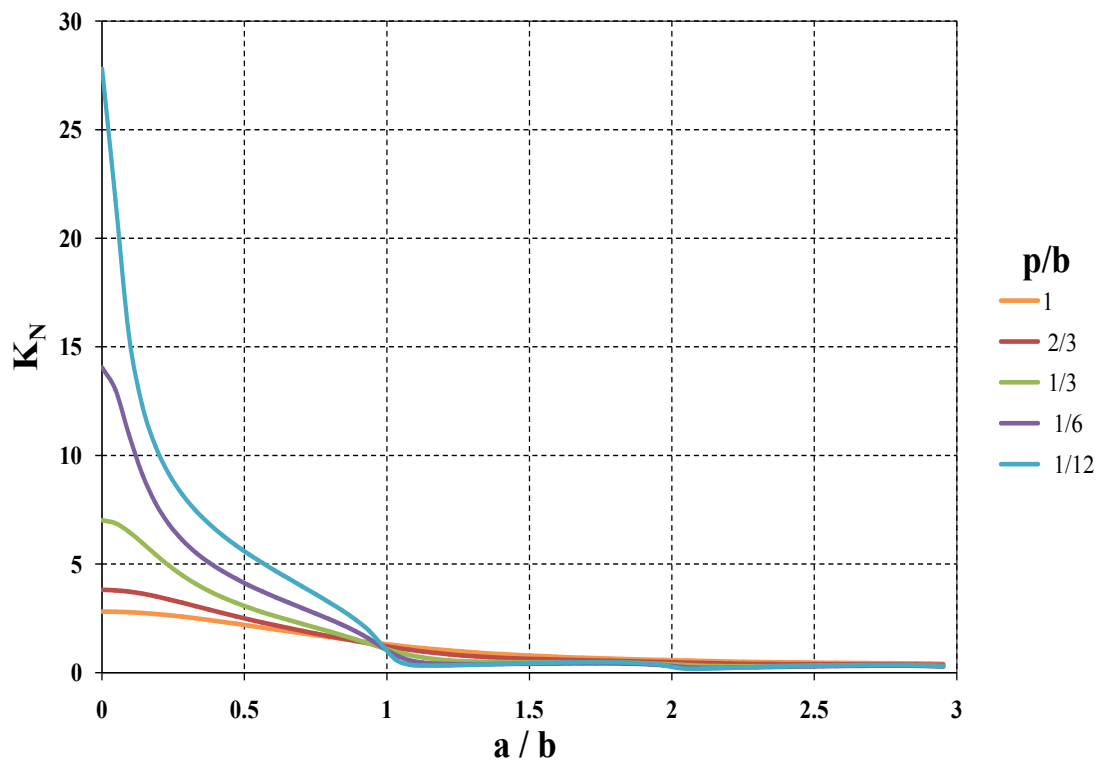


Figure 2.27: Configuration three,  $\mu = 0.9$

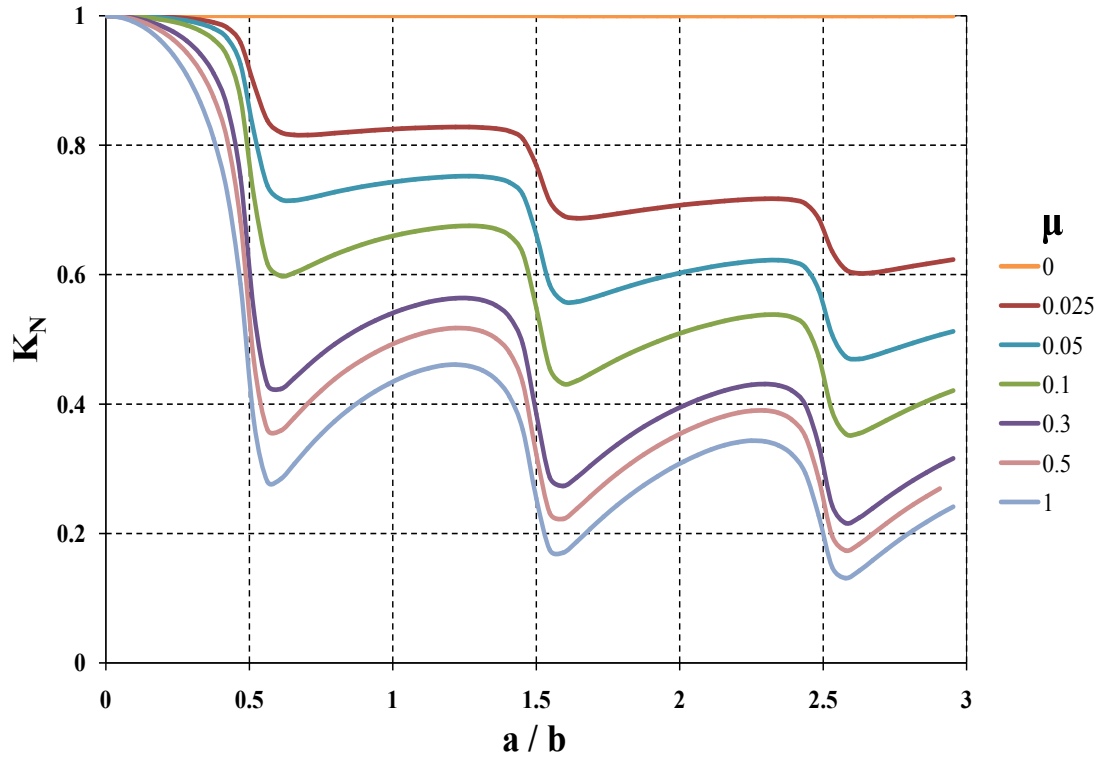


Figure 2.28: Stiffness ratio comparison for configuration one,  $p/b = 1/12$

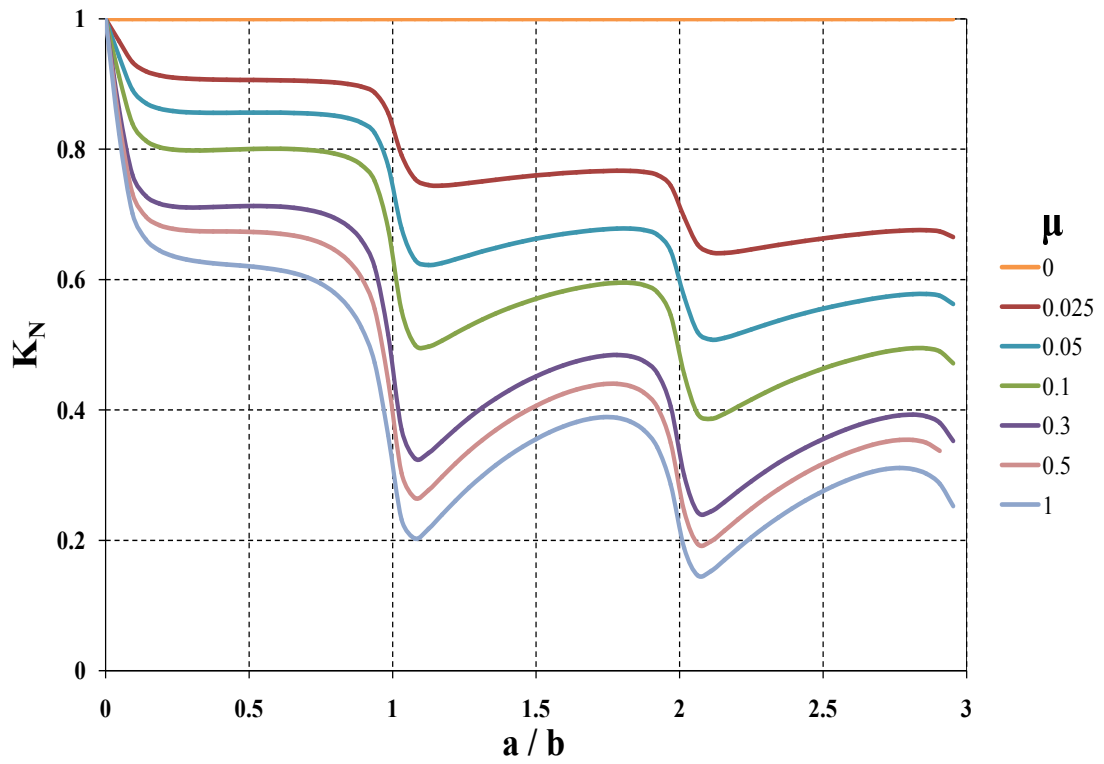


Figure 2.29: Stiffness ratio comparison for configuration two,  $p/b = 1/12$

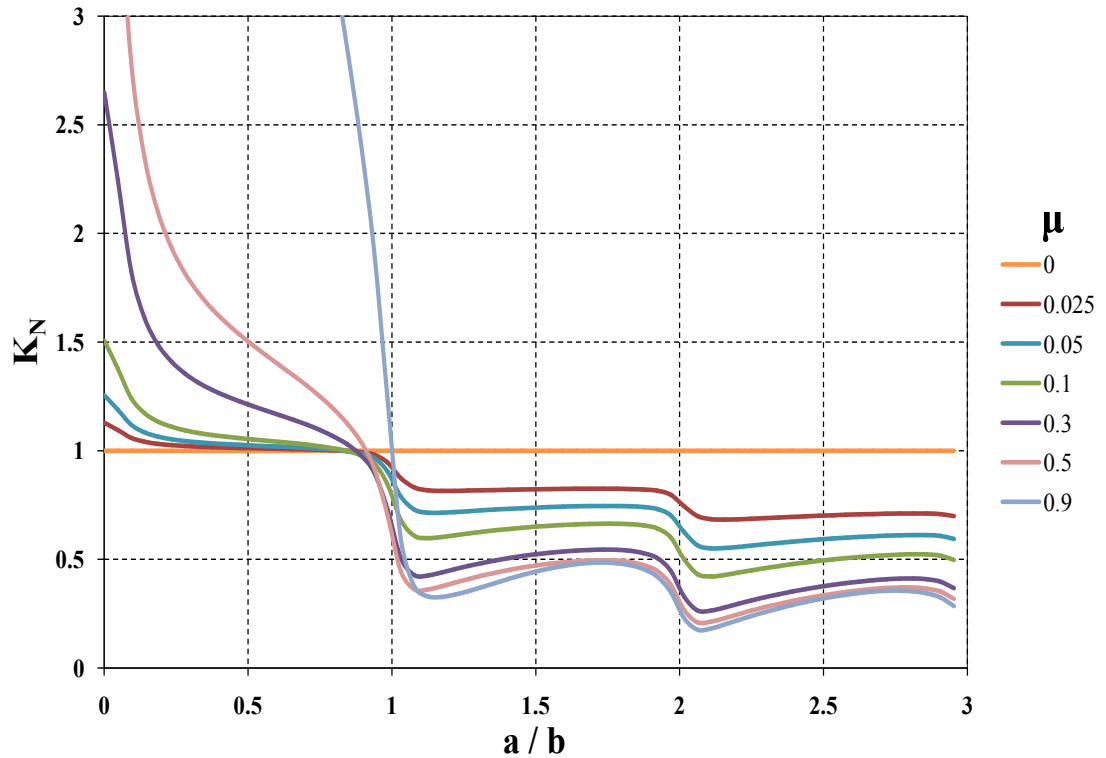


Figure 2.30: Stiffness ratio comparison for configuration three,  $p/b = 1/12$

For the broken stiffener configuration, Figures 2.24 to 2.27 and 2.30 show the variation of the normalized stress intensity factor with the crack length for different stiffness ratios  $\mu$ . Again zero  $\mu$  value corresponds to the no stiffener case which ultimately implies that normalized stress intensity factor is unity along the crack front. For the broken stiffener case, as the stiffener gets stiffer and when the crack tip is close to the broken stiffener, implying low  $a/B$  ratio, the stress intensity factor becomes very high, as shown in Figure 2.27. The increase of the normalized stress intensity factor near the broken stiffener is considered to be mainly due to the fact stiffer stringers carry more load, and the broken stiffener tends to open up the crack. It should be noted that in order for the far field strains to be same in the sheet and the stringers, the stringers are loaded by  $SE_s/E$ . Therefore, in the broken stiffener the rivet forces, which become very high, tend to open up the crack in the sheet causing the stress intensity factor to increase sharply near the broken stiffener. However, away from the broken stiffener the rivet forces in the intact stiffeners act on the sheet such that they tend to close the crack. Since the stiffer stringer is loaded more compared to the less stiff stringer, away from the broken stiffener stress intensity factor becomes less for the sheet reinforced with stiffener stringers, compared to the stress intensity factor for the sheet reinforced with less stiff stringers.

### 2.3.5 The effect of the *rivet diameter* on $K_N$

In the analytical study of Poe [6], rivet diameter enters into the formulation in the calculation of the influence coefficient  $A_{ij}$ . During the derivation of the influence coefficient, the rivet force is distributed uniformly over the rivet diameter  $d$ , and this is how the rivet diameter is included in the analysis. In the thesis, the effect of the rivet diameter on the normalized stress intensity factor is also studied. Results are presented for the central crack between the two stiffener case (configuration 1).

Figures 2.31 and 2.32 show that with increasing rivet diameter,  $K_N$  slightly decreases. It is seen that for small rivet pitch to stringer pitch ratio ( $p/b$ ), the effect of the rivet diameter on the stress intensity factor is more influential near the stiffeners, and away from the stiffeners the effect of the rivet diameter becomes less. However, for high  $p/b$ , the effect of rivet diameter on the stress intensity factor is less influenced by the stiffener. For large values of  $p/b$ , rivet forces cause a steady decrease in the stress intensity factor because crack tip is farther away from the closest rivet, and the effect of the rivet diameter on the stress intensity factor is not affected from the closeness of the crack to the stiffener.

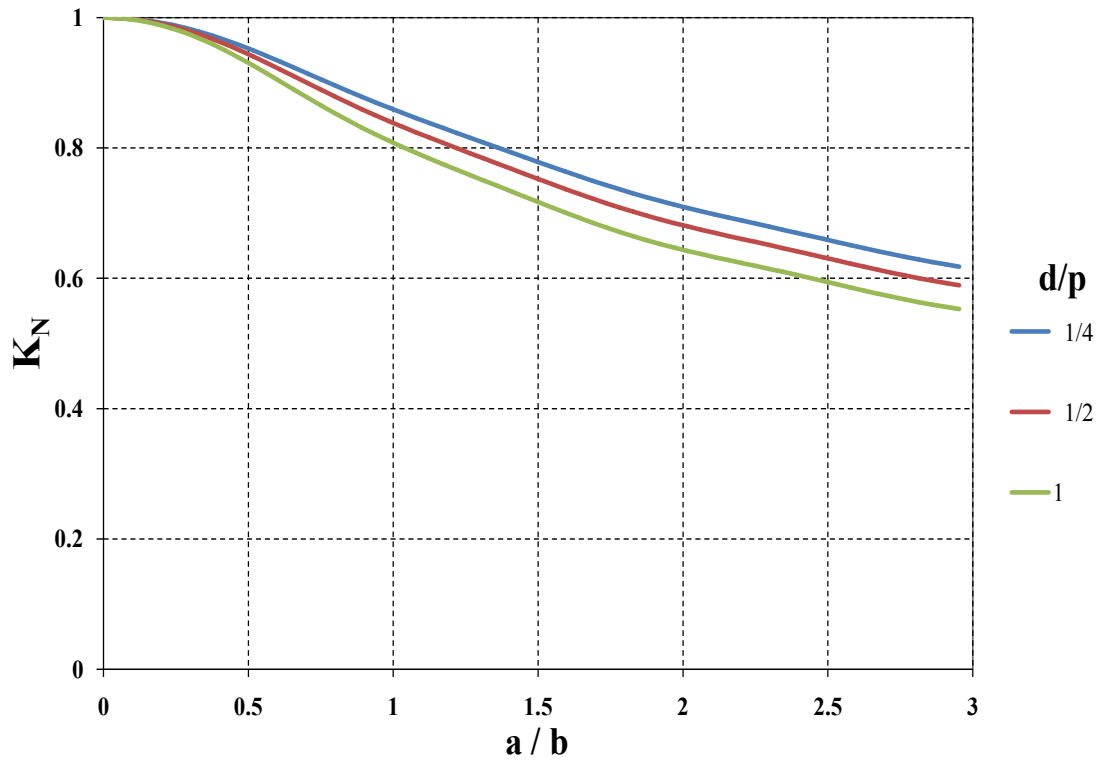


Figure 2.31: Comparison of rivet diameters, configuration one,  $\mu = 0.3, p/b = 1$

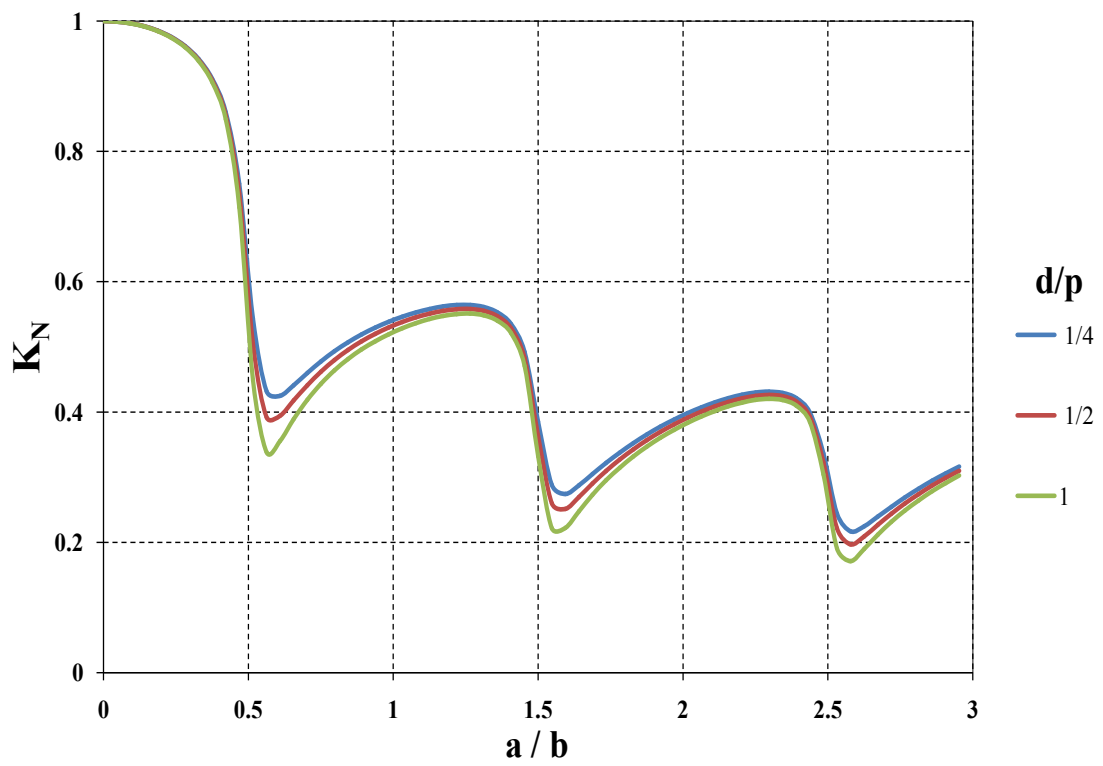


Figure 2.32: Comparison of rivet diameters, configuration one,  $\mu = 0.3, p/b = 1/12$

## CHAPTER 3

### DETERMINATION OF THE STRESS INTENSITY FACTOR BY THE FINITE ELEMENT METHOD

#### 3.1 Determination of Stress Intensity Factors by Franc2D/L Analysis

Calculation of SIF in cracked stiffened sheets by the finite element method is first carried out by Franc2D/L [20], and analytical solution of Poe is replicated. For this purpose, a very wide sheet, containing many stiffeners, is modeled. Calculations are done for a stiffened sheet with a crack extending equally on both sides of point midway between two stringers, which is configuration one and the broken stiffener case, which is configuration three. Although SIF's are calculated for the crack propagating up to  $a/b$  ratio of 3, to eliminate the effect of the boundary and to simulate an infinite size sheet, 25 stringers are created in the half symmetric model.

Figure 3.1 shows a small portion of the finite element mesh with riveted stringers. Franc2D/L simulates crack growth in layered structures but the total number of layers is limited with a default value of ten. Because there is a need for high number of stringers in the half model, in the current study a distinct layer allocation could not be made for each stringer. Therefore, all stringers are included in a single layer, which has two distinct material zones denoted by two and three in Figure 3.1. In Figure 3.1 part (b), zone two represents stringers which are shown by the shaded regions, and zone three is a very weak material with a very low Young's modulus and a Poisson's ratio of zero, which implies a region without any material. With such a modeling technique, all the stringers are included in a single layer and the maximum number of layer limitation of Franc2D/L is bypassed.

### 3.1.1 Model Definition

#### 3.1.1.1 Intact stiffener model

Figure 3.1 shows the finite element model for configuration one. As shown in Figure 3.1 part (b), cracked sheet is modeled in layer 1 with a crack that is introduced at the symmetry plane, and crack is allowed to propagate along the crack line shown in Figure 3.1 part (a). The two layers, cracked sheet and stringers, are represented with separate meshes which overlap with each other and layers are connected with rivet elements. In Franc2D/L, rivets are treated as elastic shear springs, shown by triangles in Figure 3.1, which connect two layers at the nodes.

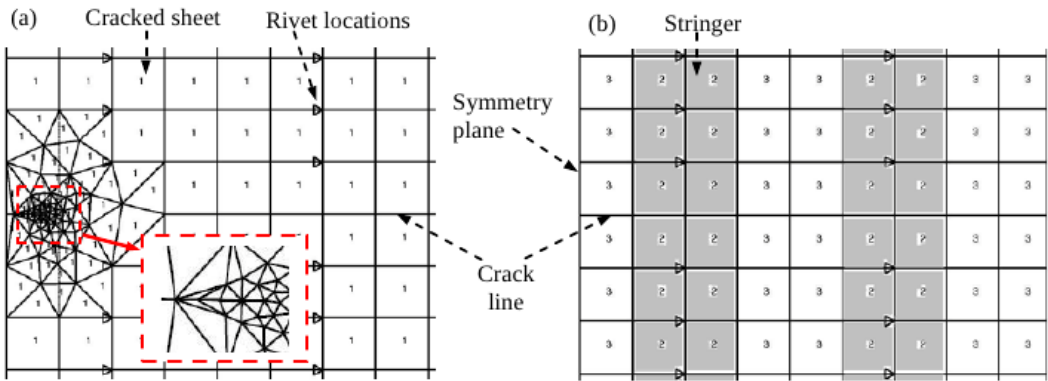


Figure 3.1: Finite element model of cracked sheet with riveted stringers (a) Layer 1: Cracked sheet (b) Layer 2: with two distinct material zones; 2:Stringer material, 3:Weak material

Stress intensity factors are calculated by assigning different shear modulus to the rivet element. To replicate the analytical solution of Poe, initial calculations are done for rigid connection between the stringers and the cracked sheet at the rivet locations. For this purpose, a very high shear modulus is assigned to the rivet element and SIFs are calculated, at incremental crack lengths, by the modified crack closure technique.

#### 3.1.1.2 Broken stiffener model

A very simple modification is done for the broken stiffener case. As it is shown on Figure 3.2, the neighboring elements to the crack on the first stiffener are modeled with very low stiffness material. Thus, the first stiffener on the crack in the sheet behaves like a broken stiffener. In the present study, only the stiffener at the symmetry plane is modeled as broken stiffener. The number of broken stiffeners can be increased easily by following the same modeling approach.

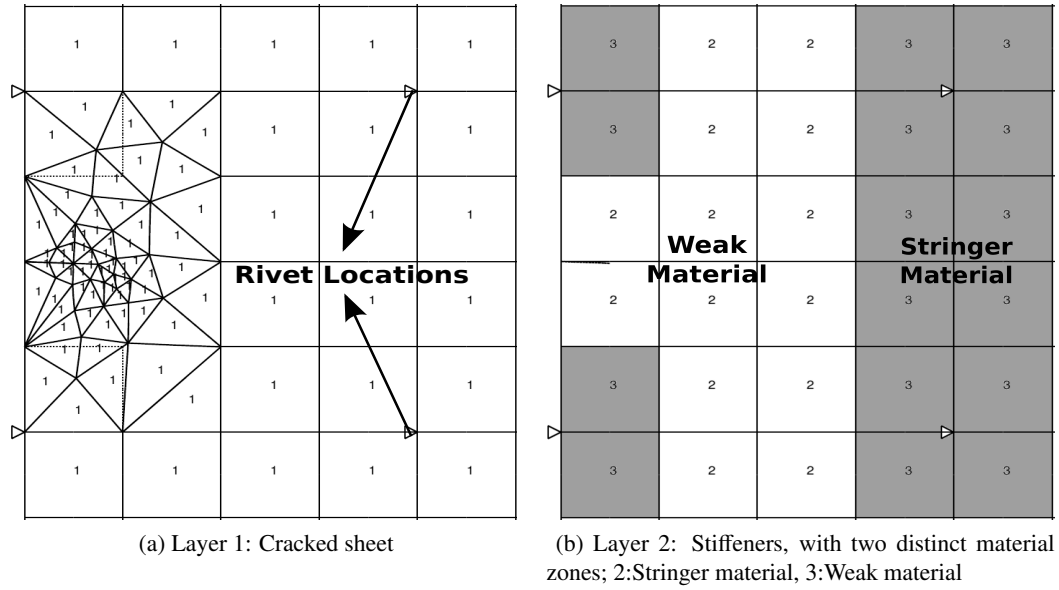


Figure 3.2: Finite element model of the cracked sheet with broken stiffener

### 3.1.2 Analysis results of Franc2D/L for the intact and broken stiffener configurations

Figure 3.3 and Figure 3.4 show the  $K_N$  versus crack length curves calculated analytically and by the finite element method for total stringer stiffness to total panel stiffness ratios of 0.33 and 0.5 for configuration one. For this analysis the rivet diameter to rivet pitch ratio  $d/p$  is taken as  $1/4$ , as in the Poe's article. Very good agreement is seen for the  $K_N$  curves between analytical method and Franc2D/L. Franc2D/L solution gives slightly higher  $K_N$  values, because in the analytical model the rivet diameter is taken into account, however in Franc2D/L, rivets do not have physical radius, they only have shear stiffness. In addition, Franc2D/L model is a finite sized sheet, whereas analytical solution is valid for infinite size sheet.

Figures 3.5 and 3.6 show the normalized stress intensity factor versus crack length curves for the broken stiffener case. It is seen that the analytical and the finite element method also give very close results for the broken stiffener case. This study in a way verifies that the modification that was made in [7] is quite reliable. It should be noted that the analytical solution gives closer results with Franc2D/L for small rivet diameters. This is expected, because as it is stated before, in the analytical solution rivet diameter is taken into consideration, whereas in Franc2D/L rivets are assumed to exist at points with no physical radius. The effect of the rivet diameter on  $K_N$  discussed in detail in Section 3.2.1.1.

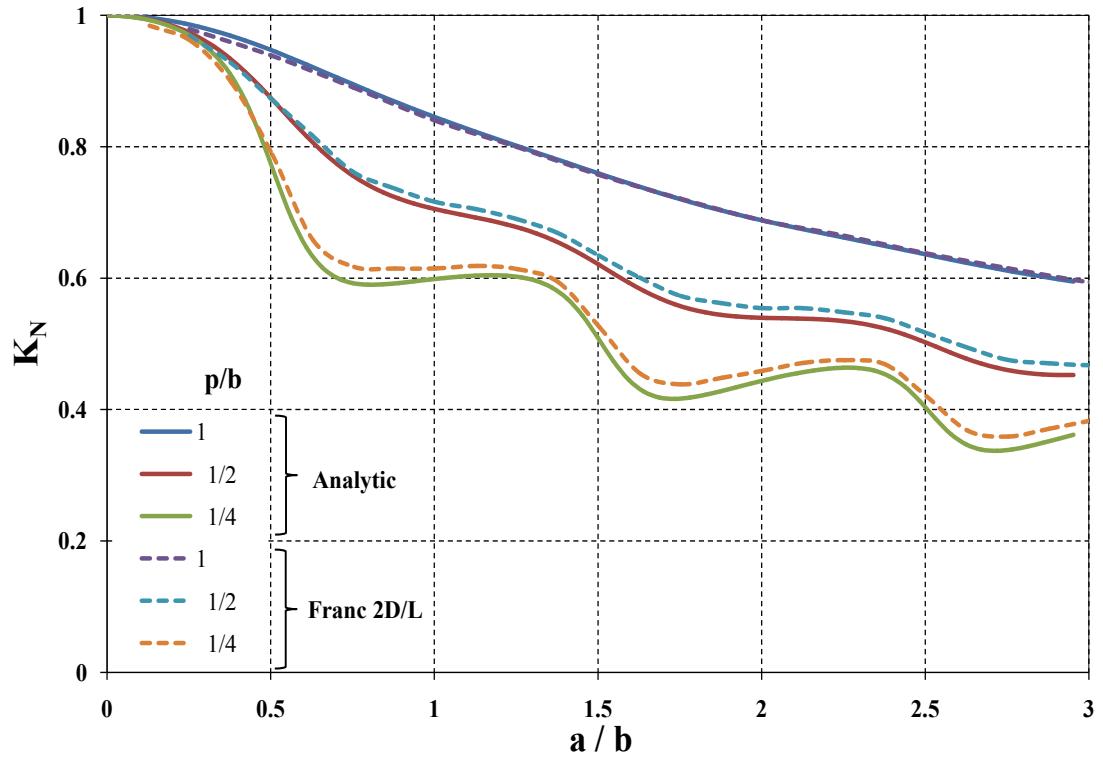


Figure 3.3: Analytical Method vs Franc 2D/L, configuration one,  $\mu = 0.33$ ,  $d/p = 0.25$

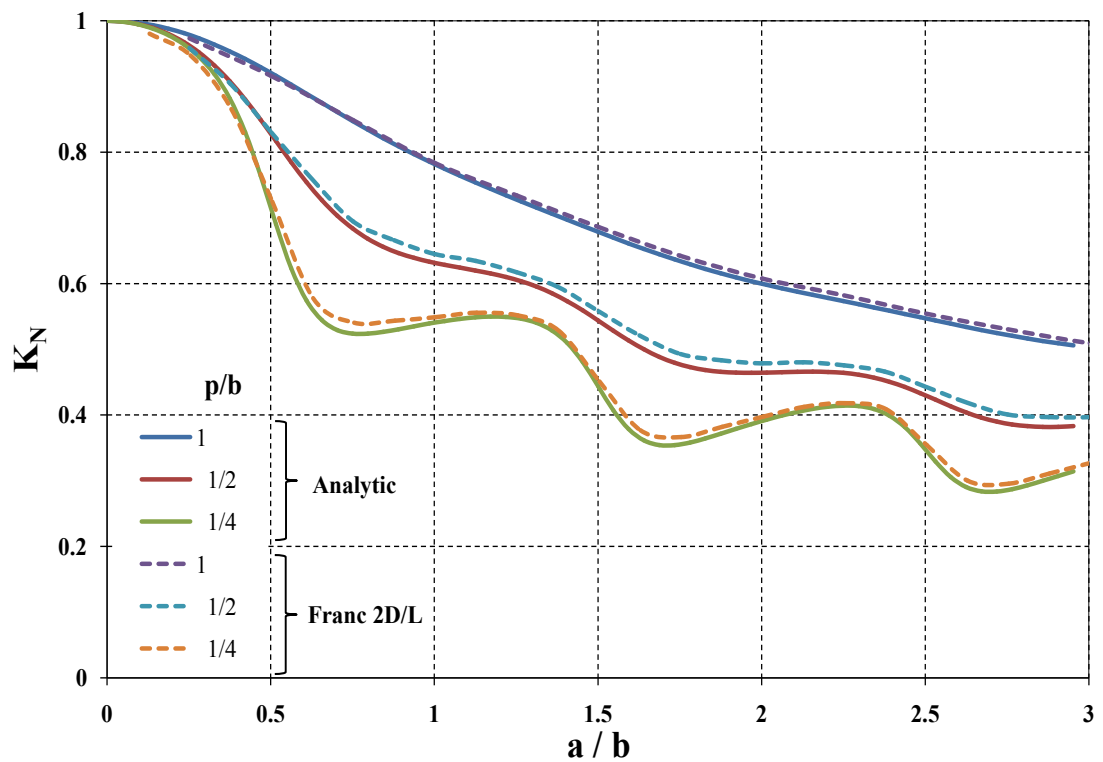


Figure 3.4: Analytical Method vs Franc 2D/L, configuration one,  $\mu = 0.5$ ,  $d/p = 0.25$

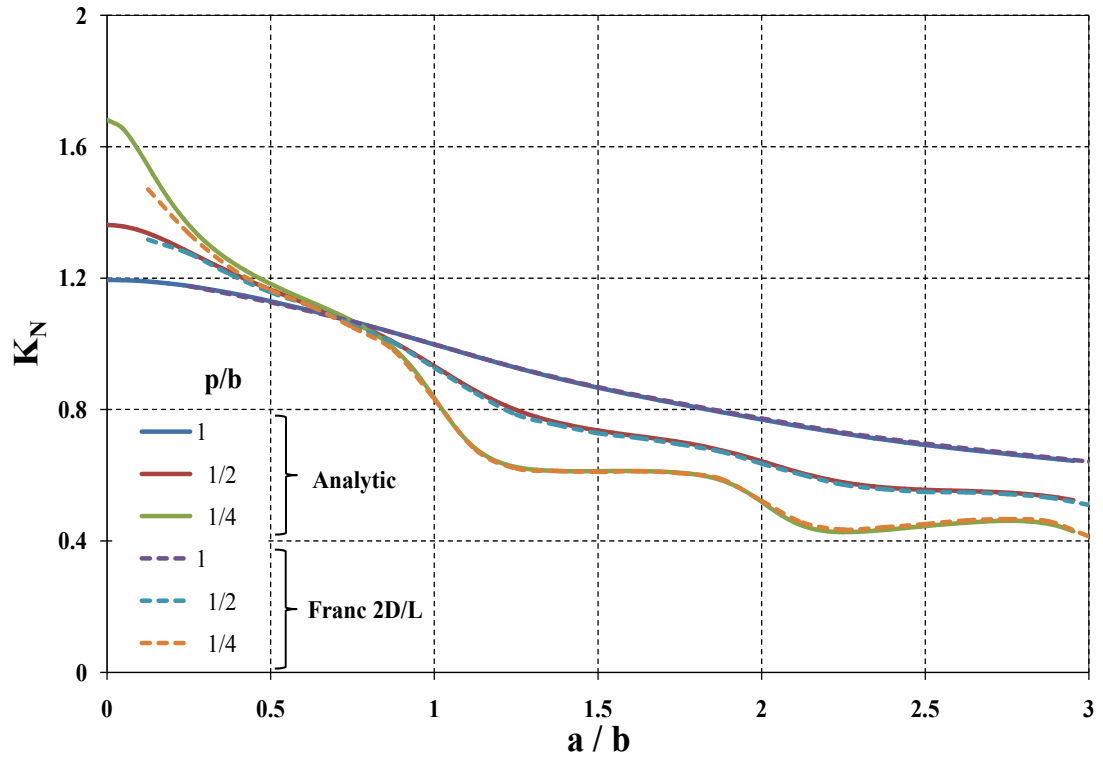


Figure 3.5: Analytical Method vs Franc 2D/L, configuration three,  $\mu = 0.33$ ,  $d/p = 0.1875$

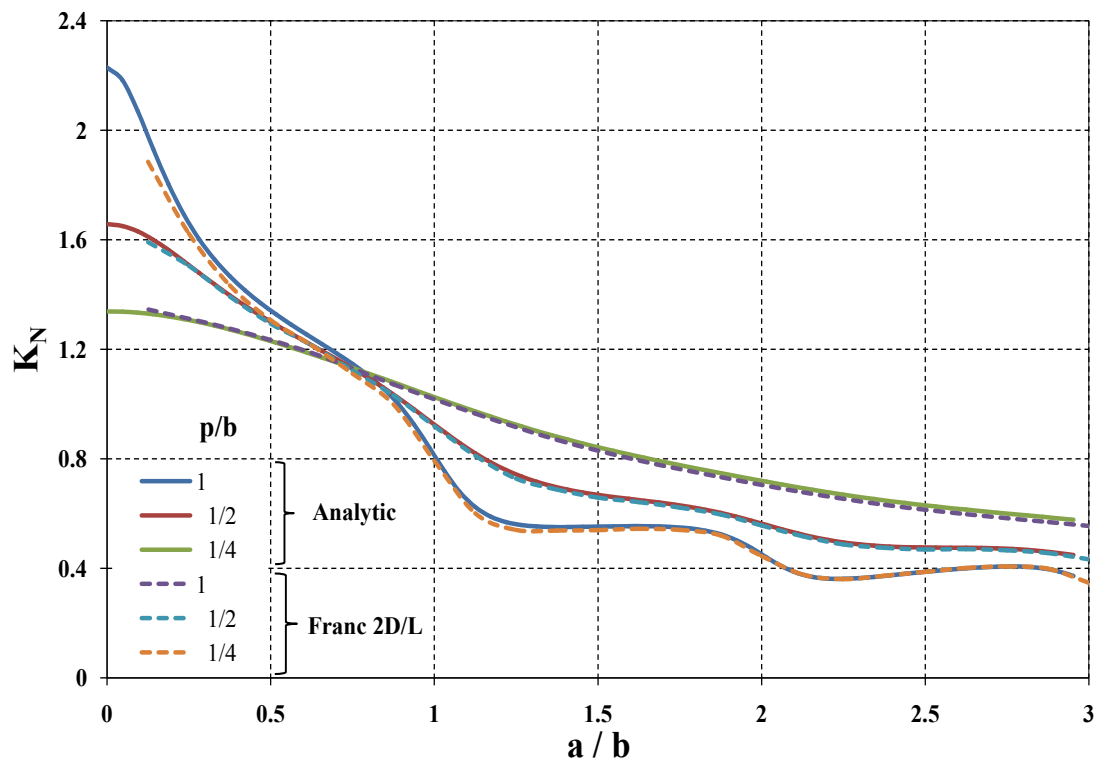


Figure 3.6: Analytical Method vs Franc 2D/L, configuration three,  $\mu = 0.5$ ,  $d/p = 0.1875$

### 3.1.2.1 The effect of rivet material

Normalized stress intensity factor versus crack length curves are also obtained for stiffened cracked sheets which use aluminum and titanium rivets in stringer-sheet connections. Stringers and the cracked sheet are assumed to be in the same plane, and Franc2D/L analysis are performed for the calculation of  $K_N$  values of stiffened cracked sheets with aluminum, titanium and rigid rivets.  $K_N$  versus crack length curves for the aluminum, titanium and rigid rivet cases are compared in Figures 3.7 and 3.8 for rivet pitch to stringer pitch ratios respectively 1 and 0.25, for  $\mu = 0.5$ . As expected, highest  $K_N$  values are obtained for the stiffened cracked sheet with aluminum rivet, which has the lowest shear modulus. Figures 3.7 and 3.8 show the impact of using fasteners with low flexibility in reducing the SIF. For stiffened cracked sheets with aluminum and titanium rivets, the absolute differences between  $K_N$  values are in the range of 0.02 – 0.04 over most of the crack length. However, when rigid rivet assumption is made, as in Poe’s analytical solution, the reduction in SIF is considerably higher.

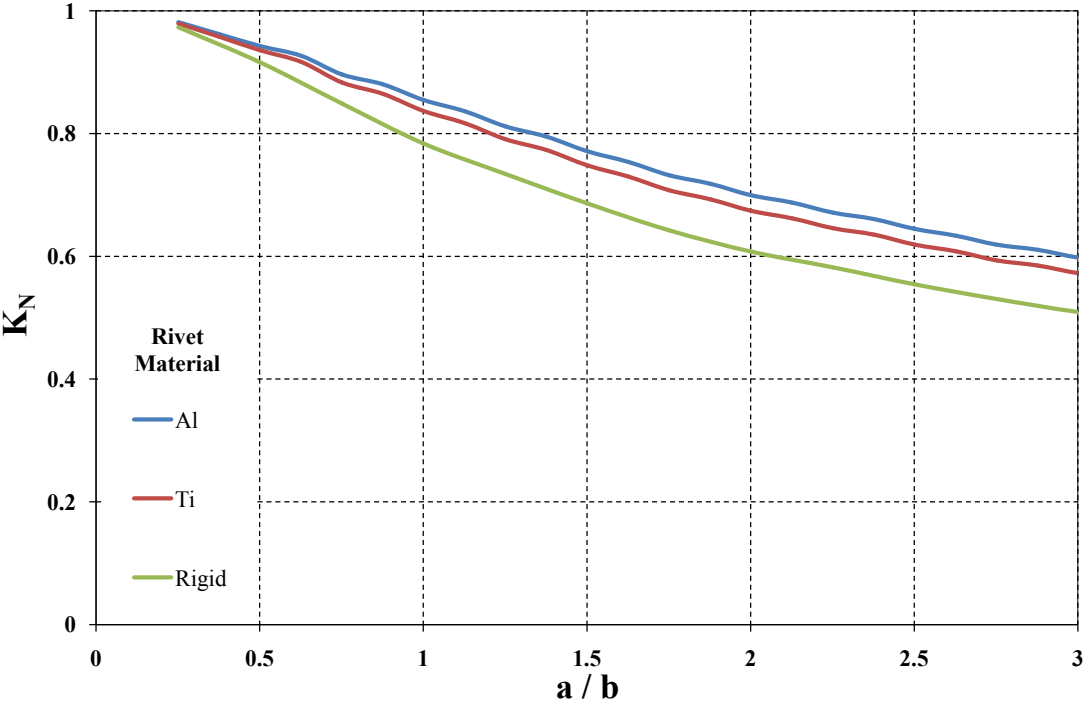


Figure 3.7: Rivet material comparison,  $\mu = 0.5$ ,  $p/b = 1$

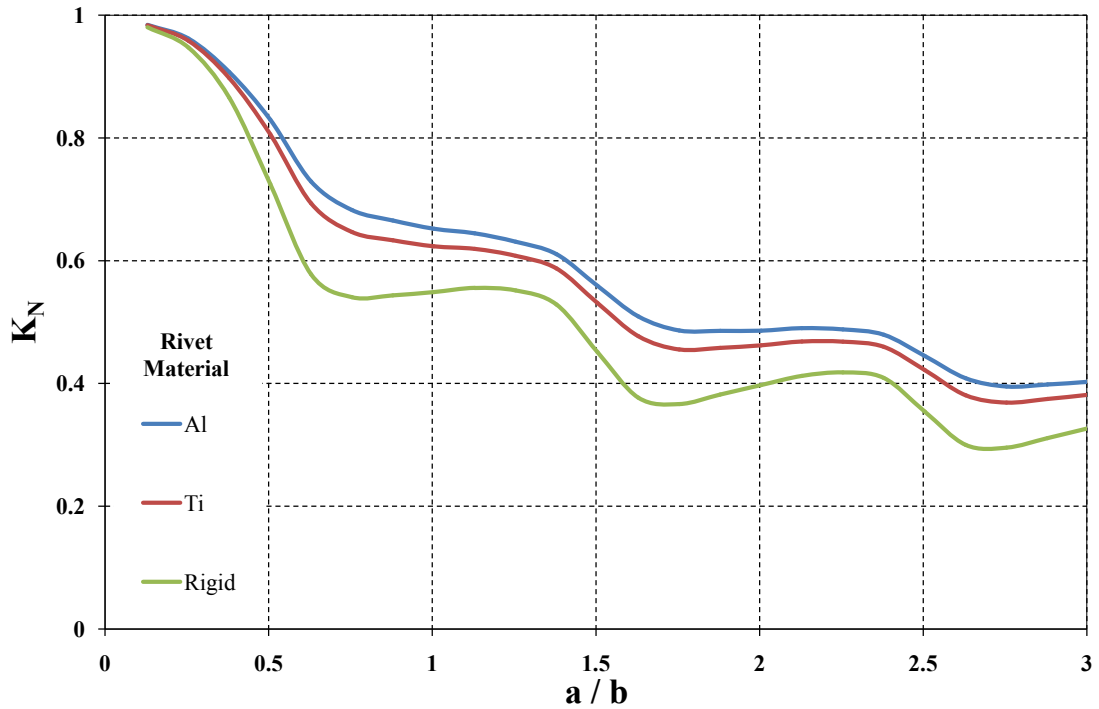
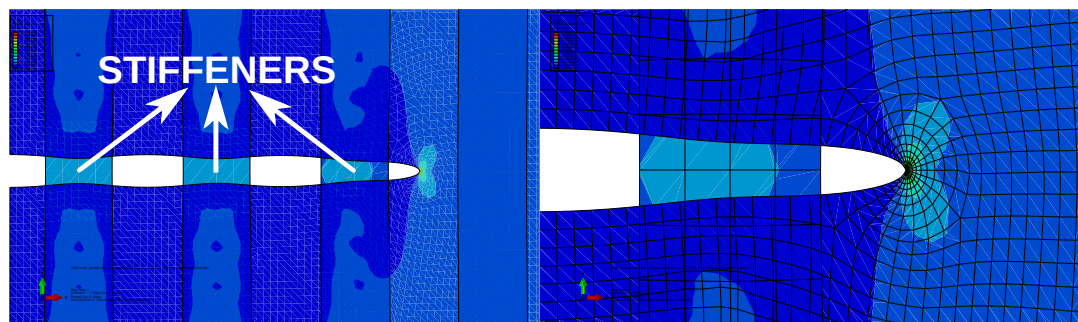


Figure 3.8: Rivet material comparison,  $\mu = 0.5$ ,  $p/b = 1/4$

### 3.2 Determination of Stress Intensity Factors by Abaqus Analysis

The second part of the finite element based SIF calculations of stiffened cracked sheets is performed by Abaqus [23] using the same model that is used in Franc2D/L analysis. Abaqus finite element model of the cracked sheet with riveted stringers is illustrated in Figure 3.9. Figure 3.9a shows the deformed cracked sheet under uniform tension which is applied as shown in Figure 2.1, and Figure 3.9b shows the deformed finite element mesh on the crack tip region.



(a) Deformed stiffened cracked sheet under uniform tension

(b) Focused mesh around the crack tip

Figure 3.9: Abaqus finite element model of the cracked sheet with riveted stringers

Cracked sheet and the stringers are modeled with four node S4R shell elements, and point based mesh independent fasteners are generated by the face to face attachment method. To model the rigid riveted connection, rigid bushing type connector section is used, and for flexible rivet connections, aluminum and titanium bushing connectors are defined and used accordingly. Crack is defined by creating duplicate grids along the crack line, and focused mesh is generated around the crack tip for obtaining better J integral results. Stress intensity factors are calculated by the contour integration, and square root singularity option is selected to perform *LEFM* based SIF calculations, which is explained in detail in [23]. Finite element analysis is performed on the half symmetric model.

### 3.2.1 Analysis results of Abaqus

Figures 3.10 to 3.12 give the comparison of the stress intensity factor versus crack length curves, which are calculated by *Franc2D/L* and Abaqus respectively for the rigid rivet, aluminum rivet and the titanium rivet cases, and no stringer-sheet offset is taken into account. Very good agreement is observed between the results of *Franc2D/L* and Abaqus analysis.

Although the rivets are given the same shear rigidity, SIF's predicted by Abaqus are slightly higher than the *Franc2D/L* for the titanium rivets and slightly lower than the *Franc2D/L* for the aluminum. This may be due to the formulation differences of the Abaqus and *Franc2D* rivet elements. In the Abaqus, the rivets has to have a physical radius, and the flexural rigidity and the shear rigidity should be defined for all three dimensions, but in the *Franc 2D*, simply the nodes of the sheet and the stringer is tied, and this tie has only shear stiffness. It should be noted that when the stringer-sheet offset is not modeled, the nodes on the stringer and the sheet coincide, and rivets essentially behave like shear springs as is the case in *Franc2D/L*.

For the rivet pitch to stringer pitch ratio of 1 and  $\mu = 0.33$ , Figure 3.13 compares the  $K_N$  values, calculated by Abaqus, for the rigid, aluminum and titanium rivets cases. Abaqus results also show the impact of using fasteners with low flexibility in reducing the stress intensity factor. It should be noted that when the stringer-sheet offset is not modeled, the nodes on the stringer and the sheet coincide, and rivets essentially behave like shear springs as is the case in *Franc2D/L*. Therefore, *Franc2D/L* and Abaqus results are very close to each other.

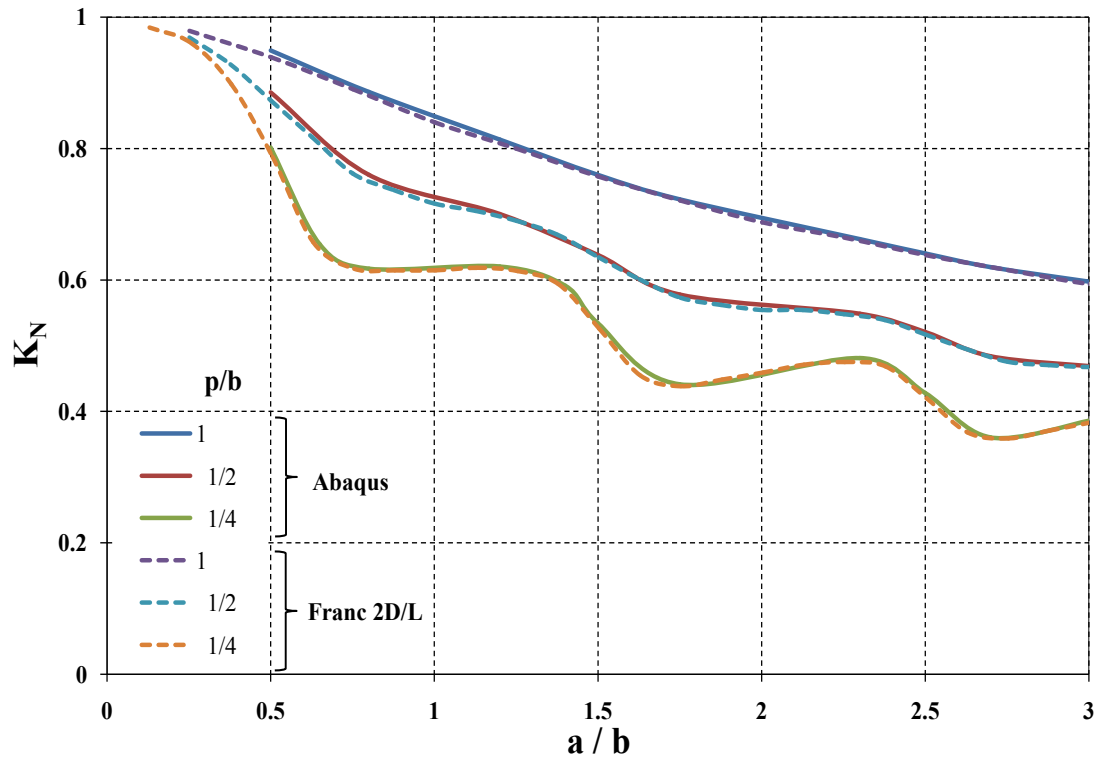


Figure 3.10: Stress intensity factor versus crack length for the rigid rivet case: Abaqus vs Franc2D/L,  $\mu = 0.33$

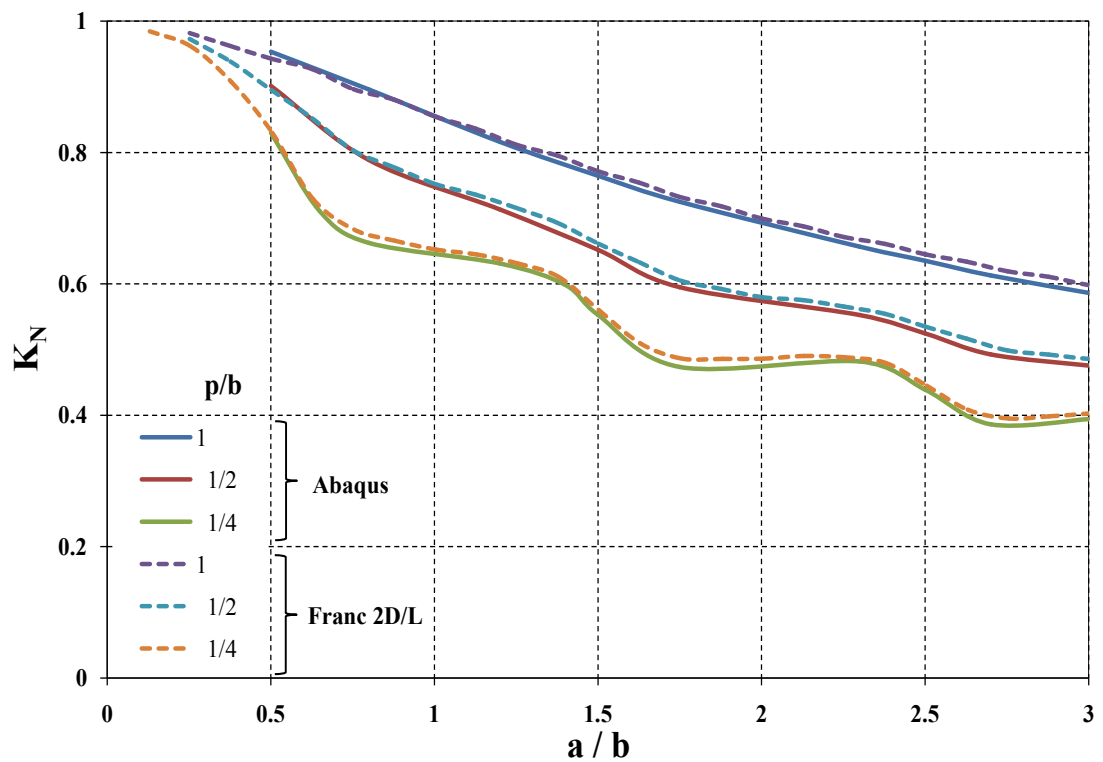


Figure 3.11: Stress intensity factor versus crack length for the aluminum rivet case: Abaqus vs Franc2D/L,  $\mu = 0.5$

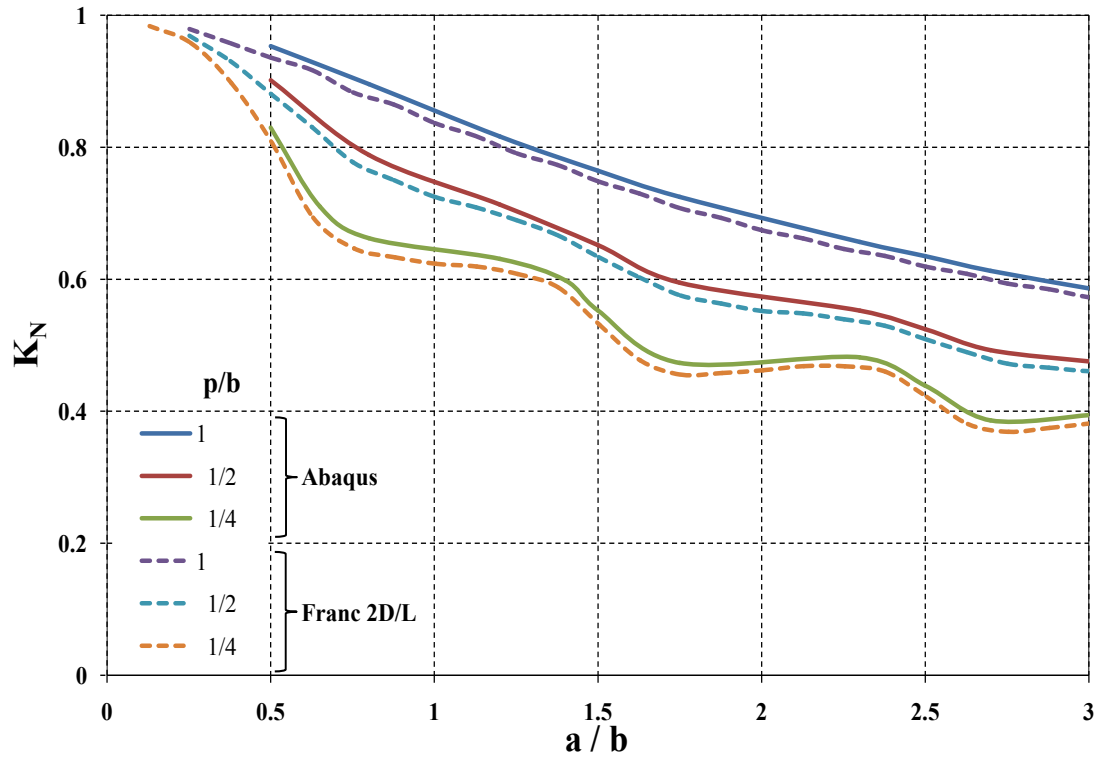


Figure 3.12: Stress intensity factor versus crack length for the titanium rivet case: Abaqus vs Franc2D/L,  $\mu = 0.5$

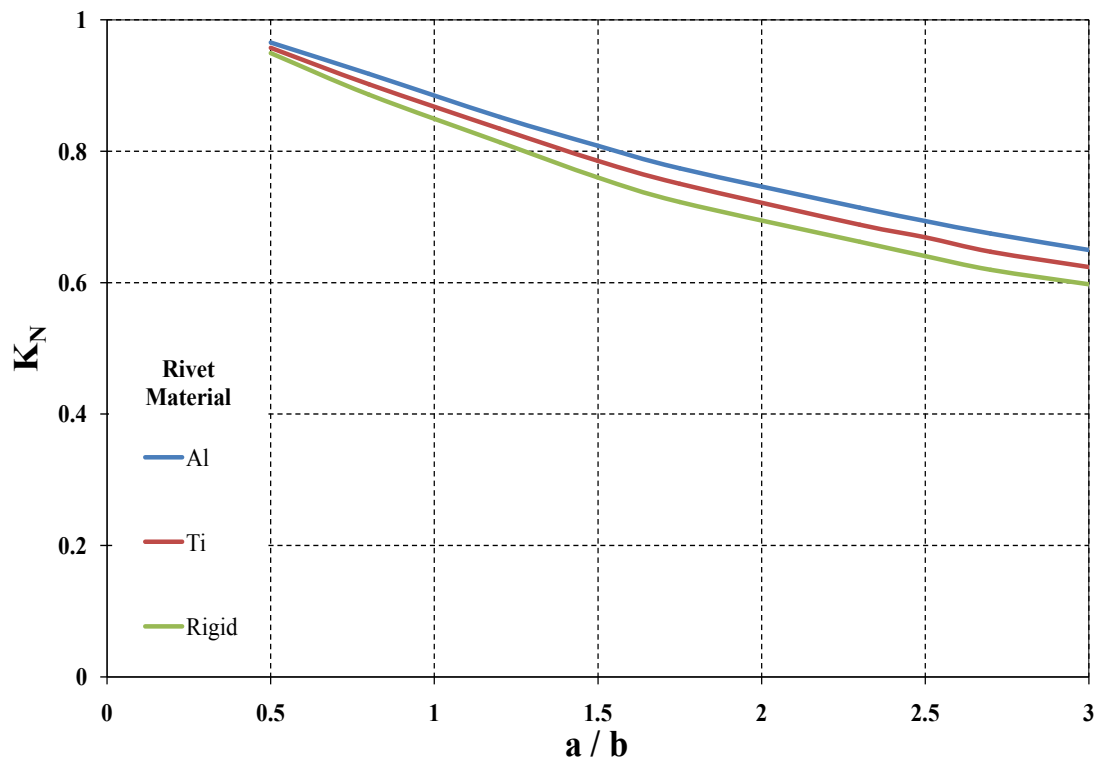


Figure 3.13: Rivet material comparison with Abaqus,  $\mu = 0.33$ ,  $p/b = 1$

### 3.2.1.1 The effect of physical diameter of the rivet on the stress intensity factor

The effect of physical diameter of the rivet on  $K_N$  is given in Figures 3.15 and 3.16, which show respectively the results obtained analytically and by Abaqus for the rigid rivet case with fixed rivet pitch  $p$  and  $p/b = 1$ . In Figures 3.15 and 3.16, both Analytical and Abaqus results show that increase in the physical rivet diameter has a lowering effect on the stress intensity factor. However, in the analytical solution if the rivet diameter is decreased too much, truncation error becomes dominant in the series summation for Equation (2.25). It is observed that Abaqus results are slightly higher than the results of the analytical solution. This could be due to the fact that in the analytical solution, rivet forces are assumed to be uniformly distributed at the  $y = 0$  line along the diameter of the rivet as illustrated in Figure 3.14a, but Abaqus distributes the rivet force to the circular stiffener area  $A_R$  uniformly which can be seen from the Figure 3.14b.

$$Q_{Analytic} = \int_{-d/2}^{d/2} \frac{Q}{d} dx \qquad Q_{Abaqus} = \int_{A_R} \frac{Q}{A_R} dA \qquad (3.1)$$

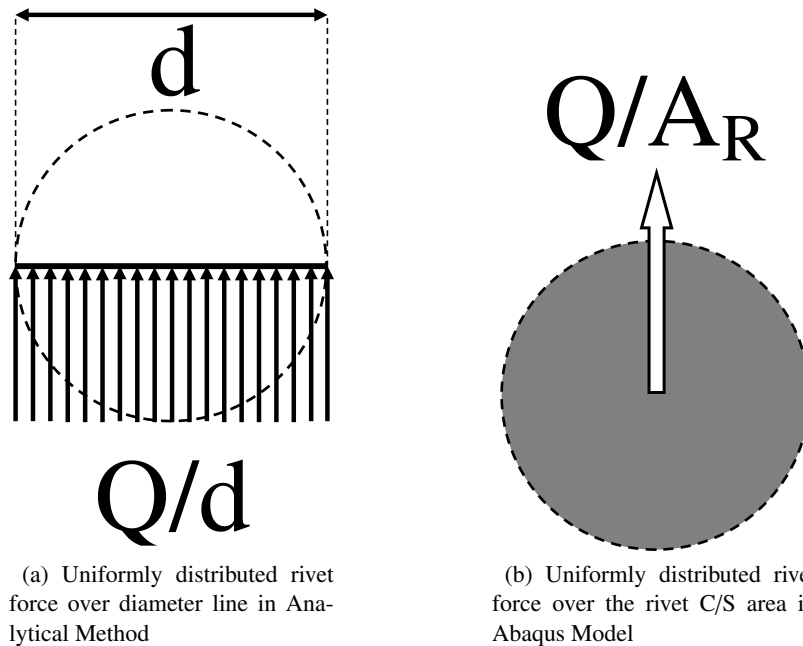


Figure 3.14: The difference between Analytical and Abaqus rivet formulation

It is also noted that the finite sized sheet used in the FEM solution could also be another factor for the slightly higher SIF's calculated by Abaqus compared to the analytical solution.

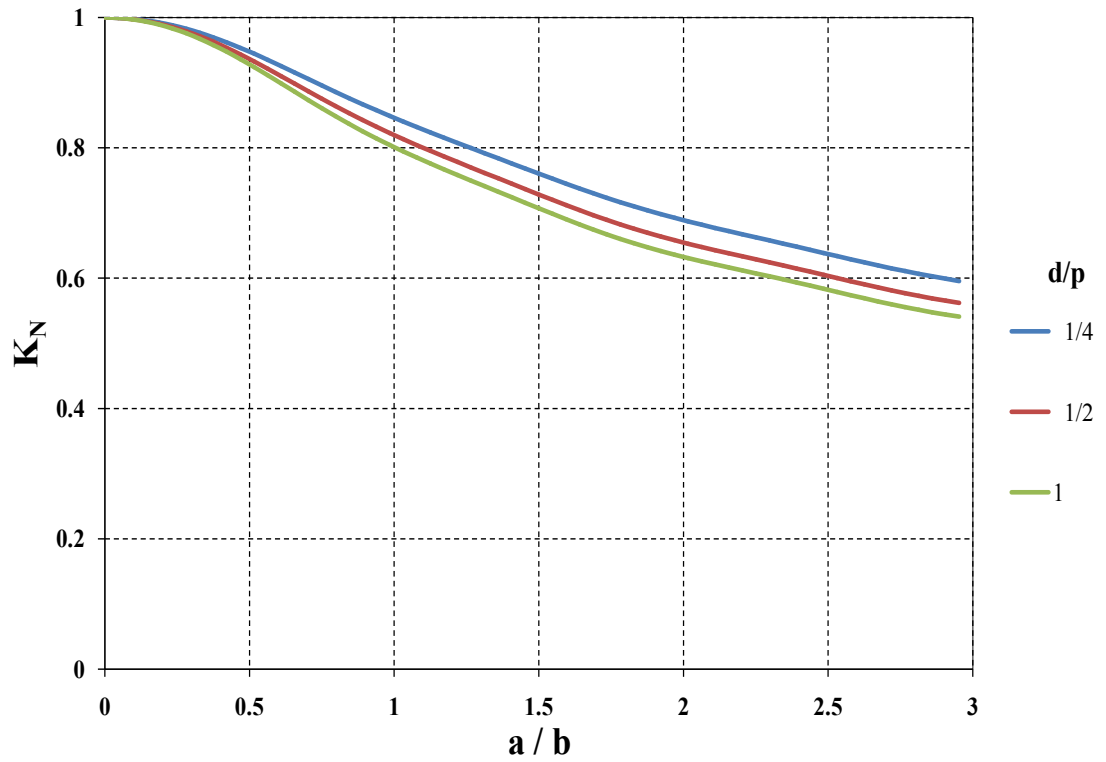


Figure 3.15: Comparison of the  $K_N$  for the effect of rigid rivet diameter on the  $K_N$  with Analytical Method

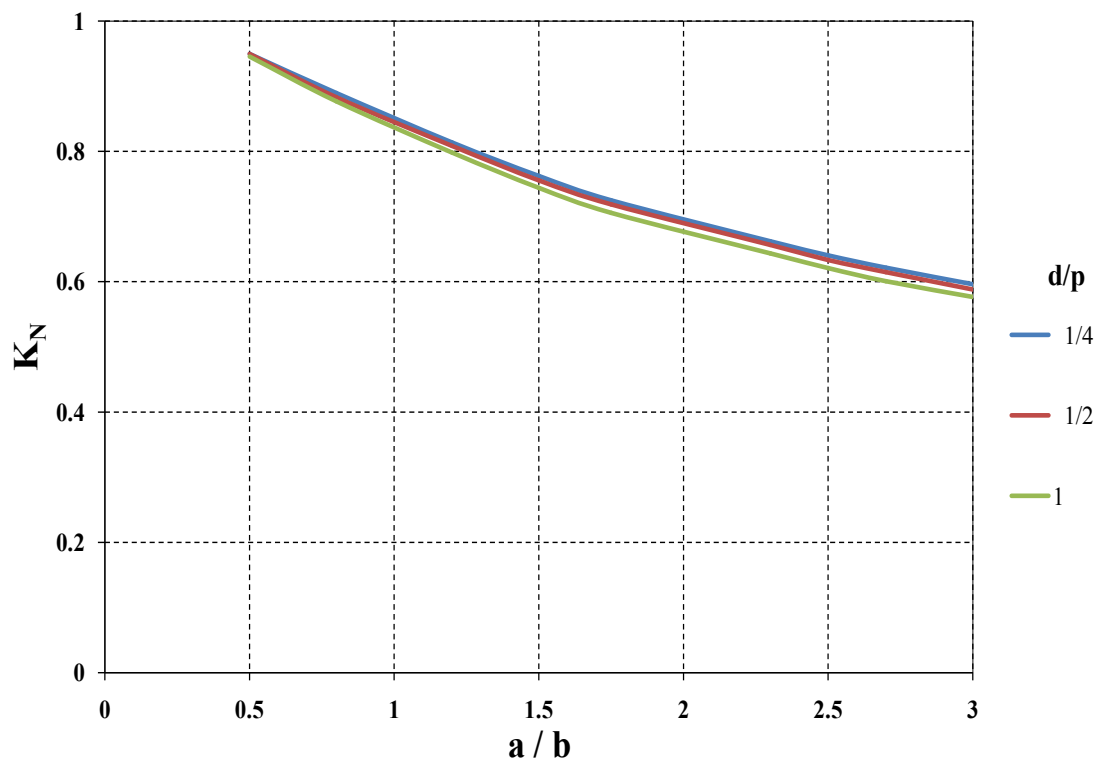


Figure 3.16: Comparison of the  $K_N$  for the effect of rigid rivet diameter on the  $K_N$  with Abaqus

**3.2.1.2 The effect of sheet-stiffener offset on the stress intensity factor**

Figures 3.17, 3.18, 3.21 and 3.22 show the stiffened sheet configurations without and with offset, respectively. The effect of stringer-sheet offset ( $o$ ) on the normalized stress intensity factors is shown in Figures 3.19 and 3.20 for the rigid and aluminum rivet cases, and for a stringer offset ( $o$ ) to stringer pitch ( $b$ ) ratio of 0.25.

From Figure 3.20, it can be seen that stringer-sheet offset has a very significant effect on the stress intensity factors because of the additional moment effect of the stringer loads on the cracked sheet, and stress intensity factor increases significantly when stringer-sheet offset is included.

It is also observed from the Figures 3.21 and 3.22 that when flexible rivets are used, although stress intensity factors increase compared to the rigid rivet case, the effect of stringer offset on the stress intensity factors decreases slightly compared to rigid rivet case.

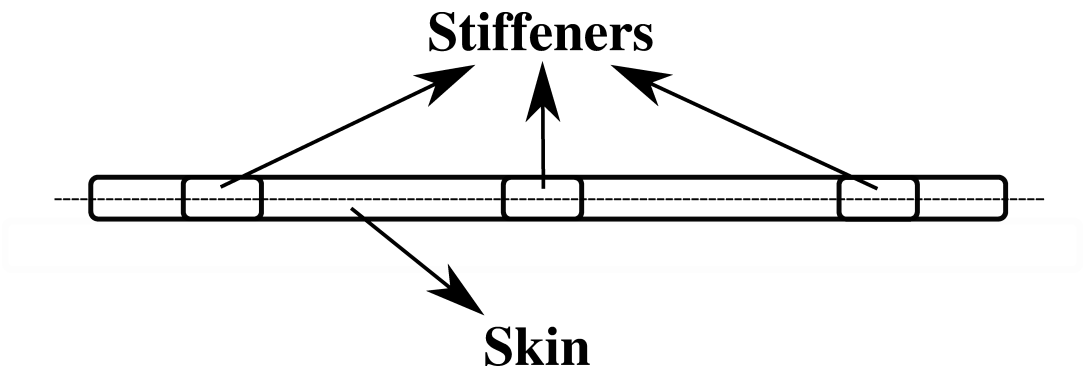


Figure 3.17: The cracked sheet and the stringers are in the same plane

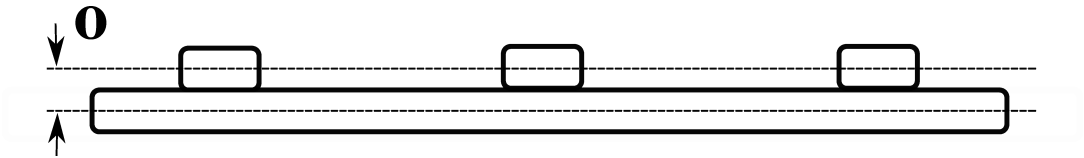


Figure 3.18: The cracked sheet and the stringer has an offset ( $o$ ) due their thicknesses

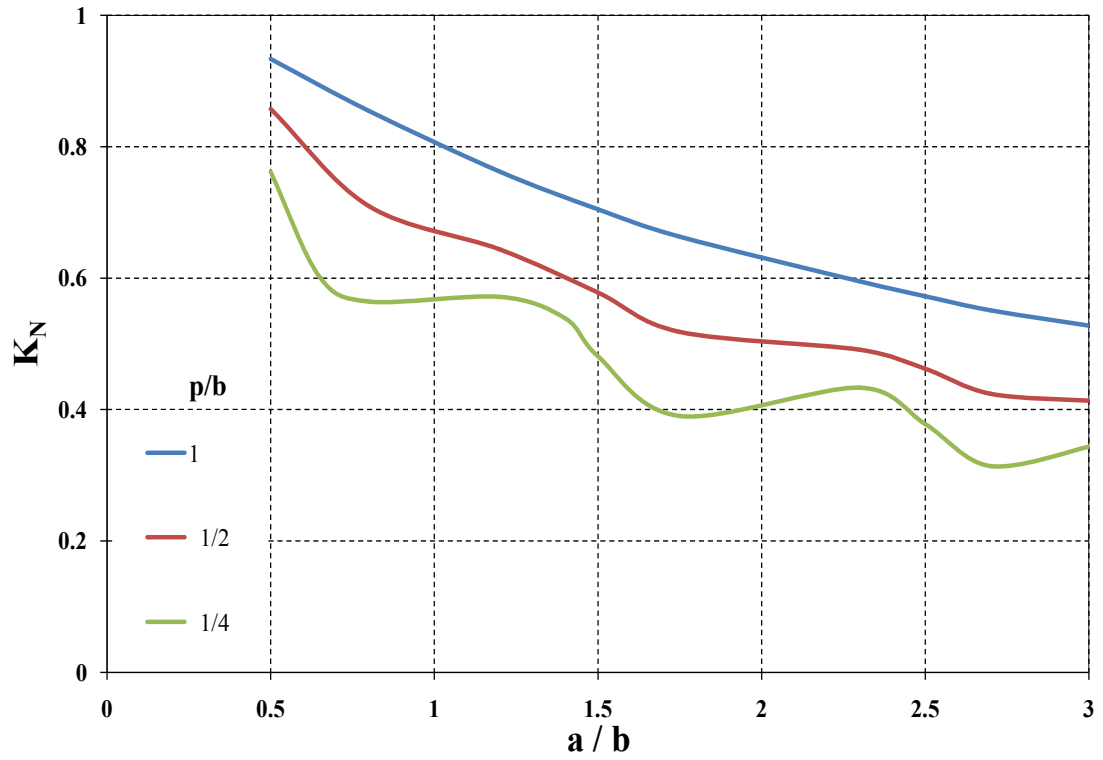


Figure 3.19: Cracked sheet and the stiffener are in the mid-plane

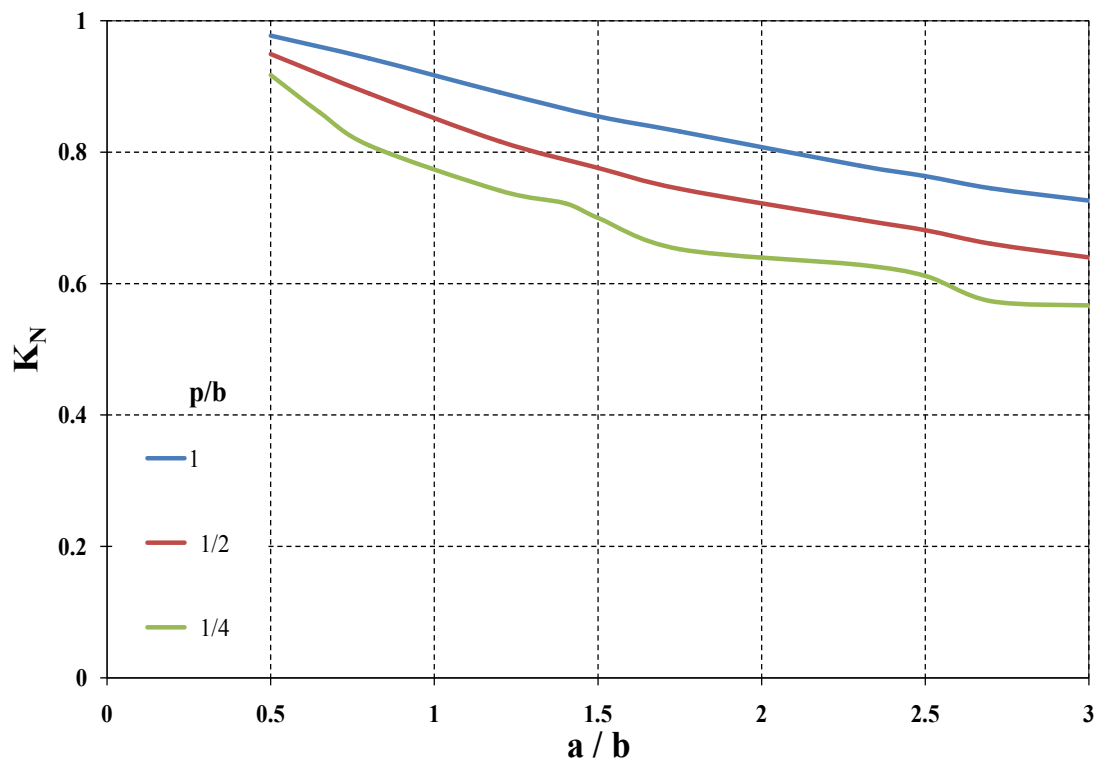


Figure 3.20: Cracked sheet and the stiffener are offsetted

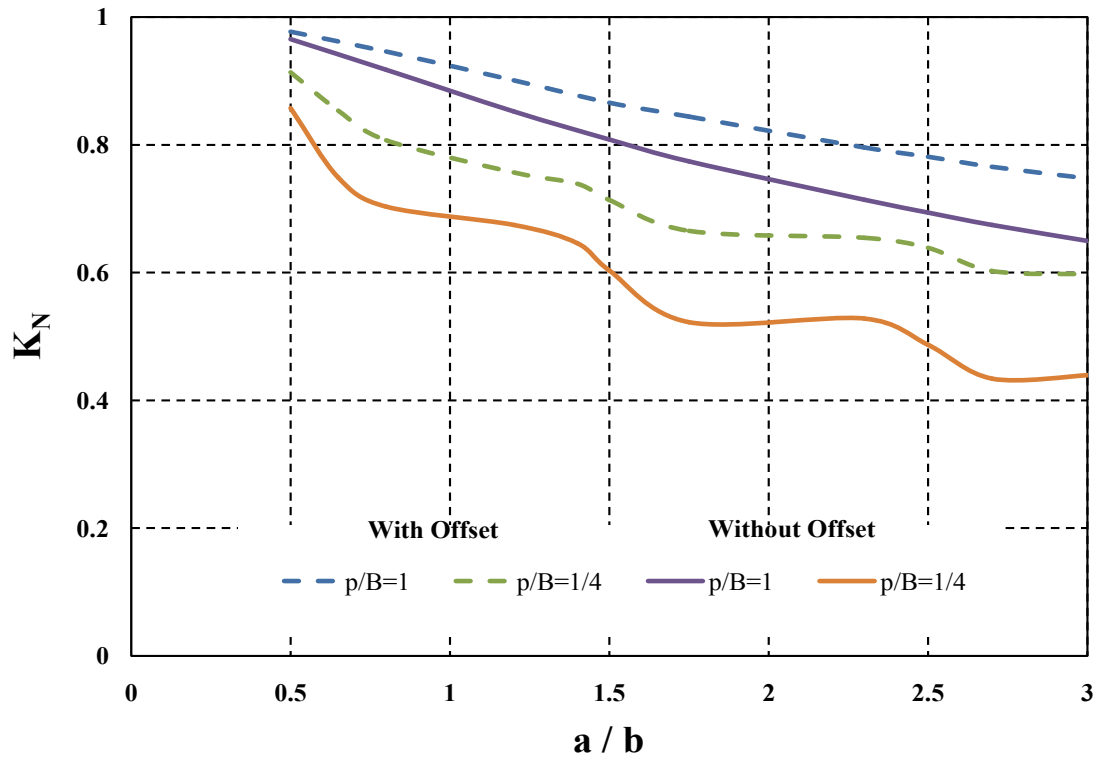


Figure 3.21: Comparison of the SIF's for the offsetted stiffener with rigid rivets,  $\mu = 0.33$ ,  $d/p = 0.25$

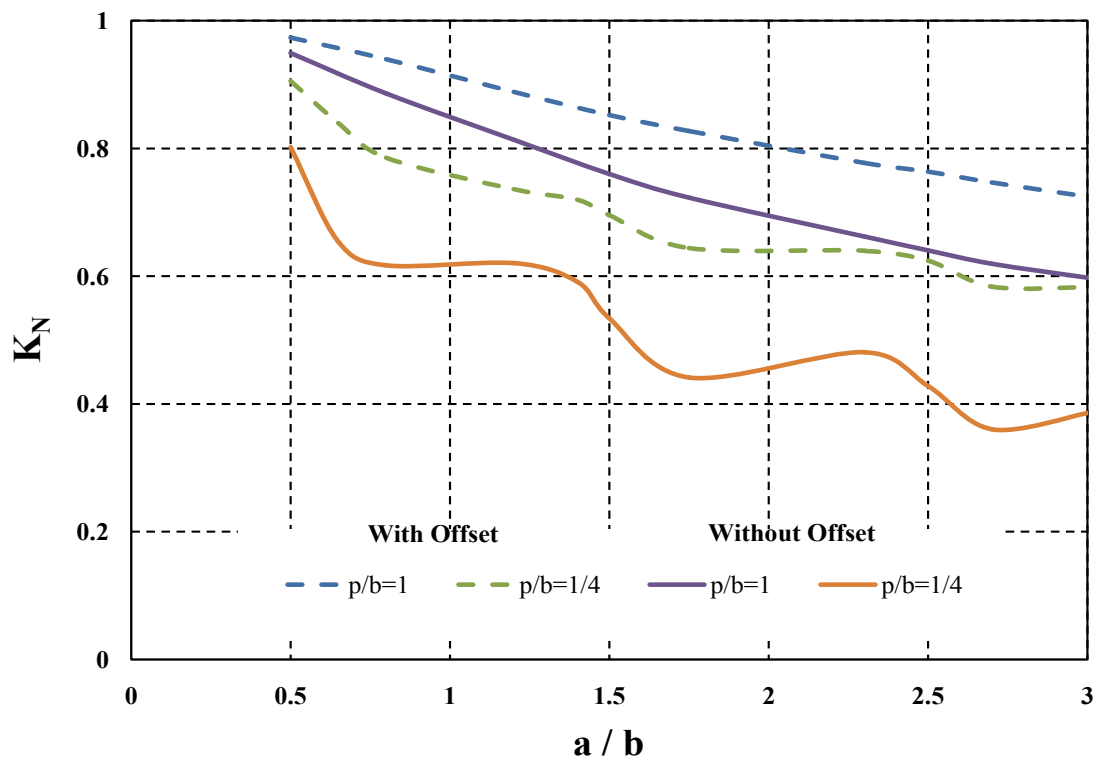


Figure 3.22: Comparison of the SIF's for the offsetted stiffener with Aluminum rivets,  $\mu = 0.33$ ,  $d/p = 0.25$

## **CHAPTER 4**

### **LIFE PREDICTION OF A STIFFENED PANEL**

#### **4.1 Introduction**

In this chapter a sample life calculation of a fuselage panel with a broken stiffener is demonstrated for a cargo airplane. The aim of this study is to emphasize the importance of the determination of the stress intensity factors for obtaining the time history evolution of cracks, and designing the structure accordingly to prevent sudden failure. It should be noted that since it is very difficult to find all of the technical specifications and dimensions of the airplanes, reasonable specifications and dimensions are assigned to get a reasonable life for a generic fuselage panel. As it is explained in Section 1.3, the airplane is exposed to internal pressure loading due to the pressure difference in very high altitudes, therefore the structure of the airplane should be strong enough to withstand that internal pressure loading, in other words the structure should be designed such that there must not be a static failure at a limit loading. Moreover, the airplane should be damage tolerant such that, there must not be a sudden detrimental failure due to the fatigue.

##### **4.1.1 Technical Specifications and Geometry of the Aircraft**

In the life prediction demonstration of the stiffened panel, A-400M military cargo airplane is chosen as the aircraft to be investigated. Available technical specifications and dimensions such as service ceiling and fuselage diameter are taken from Wikipedia and A-400M official website [34, 35], and those properties, which are not available, are only reasonable guesses. Since the main aim of this section is to demonstrate the methodology of life prediction, it is deemed that using the exact geometric properties of the stiffened panel of the aircraft is not

necessary. Table 4.1 summarizes the technical specifications and geometry of the airplane which are made up except the service ceiling for this sample life prediction analysis. Moreover, frame and stringer cross sectional dimensions are not given in any sources, therefore reasonable values are assigned to them as illustrated in Figure 4.1.

Table 4.1: Technical Specifications and Geometry of the Cargo A/C

Service Ceiling	11.300 [m]
Fuselage Diameter	5000 [mm]
Stringer Spacing	131 [mm]
Frame Spacing	500 [mm]
Rivet Diameter	2.5 [mm]
Rivet Spacing	25 [mm]
Skin Thickness	1 [mm]
Stringer C/S Area	110 [mm <sup>2</sup> ]
Frame C/S Area	260 [mm <sup>2</sup> ]
Skin Material	Al 2124 T-851
Frame Material	Al 2124 T-851
Stringer Material	Al 2124 T851

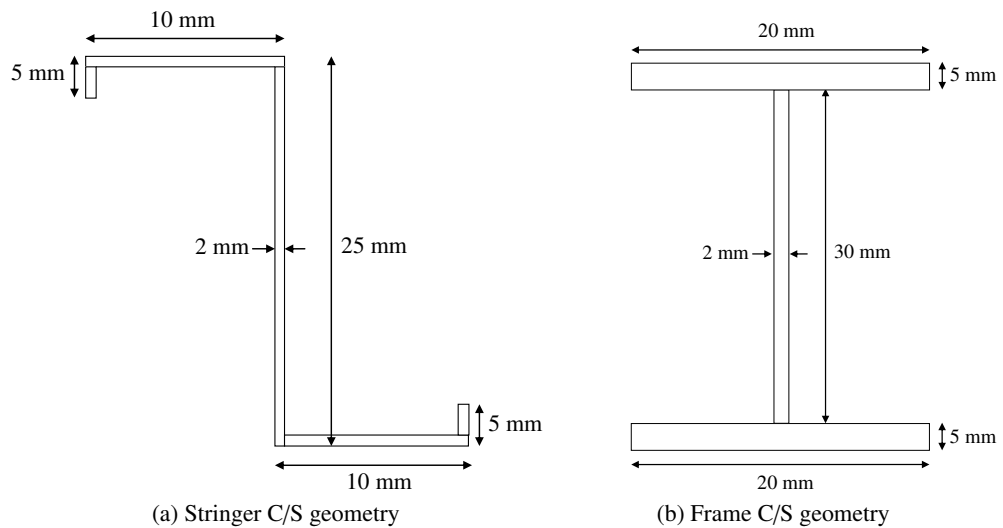


Figure 4.1: Cross sectional geometry of the stringer and frame

## 4.2 Methodology of damage tolerance analysis

The loading and the geometry plays the two main parts of the damage tolerant analysis. In damage tolerant calculations, besides the pressure loading, other loads due to the gusts, turbulence, maneuvers, landing etc., are also taken into consideration. However, in this study to keep the loading simple, only the internal pressure is taken into consideration. In the pressure loading it is assumed that the airplane climbs to the service ceiling in all of the flights. For this loading, pressure difference between the cabin and the atmosphere is maximum, and such a pressure loading is conservative. Therefore, in a one ground-air-ground cycle (GAG), the airplane experiences a pressure difference  $\Delta P$  which is equal to  $P_{sealevel} - P_{11.300m}$ . This is a repeating load that the aircraft experiences in every flight, therefore it may cause fatigue. It should be noted that the stress range of the GAG cycle for the pressure structure of a pressurized fuselage is probably the largest and most frequently applied single load cycle for most transport aircraft.

### 4.2.1 Calculation of Loads

The aircraft chosen for the sample calculation has a service ceiling of 11.300 *m* altitude [34]. Therefore, pressure difference between the sea level and 11.300 *m* can be calculated using the altitude calculator [36].

$$\Delta P = P_{(sealevel)} - P_{(11.300m)} \quad (4.1)$$

where,

$$P_{(sealevel)} = 101[kPa] \quad (4.2)$$

$$P_{(11.300m)} = 24[kPa] \quad (4.3)$$

therefore,  $\Delta P$  becomes,

$$\Delta P = 0.077 [MPa] \quad (4.4)$$

In order to obtain close end condition, axial stress due to the internal pressure applied separately, longitudinal stress for a cylinder can be written as in Equation (4.5),

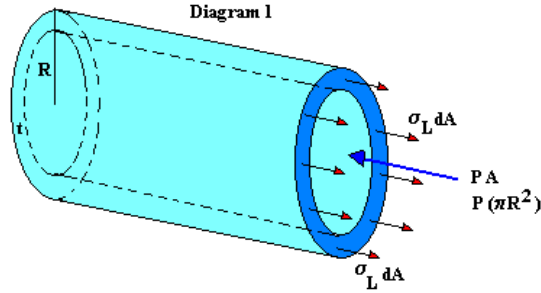


Figure 4.2: Longitudinal stress in an cylindrical pressure vessel [37]

$$\sigma_L = \frac{\Delta P r}{2t} \quad (4.5)$$

where,  $\Delta P$  is the difference between internal pressure, and the outside pressure,  $r$  is the cylinder radius, and  $t$  is the thickness of the cylinder. This case is valid for a cylinder without stiffener. For a stiffened cylinder, assuming that the stiffened cylinder is monolithic, which means that the displacements are equal at the riveting points, the longitudinal stress becomes:

$$\sigma_L = \frac{\pi r^2 \Delta P}{2\pi r t + A_s N_s} \quad (4.6)$$

where,  $A_s$  is the stringer area and  $N_s$  is the number of stringers. Substituting the numerical value of the pressure difference,  $\sigma_L$  becomes:

$$\sigma_L = 68.06 MPa \quad (4.7)$$

## 4.2.2 Determination of the normalized stress intensity factor with FEM

### 4.2.2.1 Model Definition

Figure 4.3 represents the forward fuselage of the aircraft which contains 120 stringers and 6 frames. Because of the limited time and memory, symmetry boundary conditions used on a smaller area which is highlighted red in Figure 4.3.

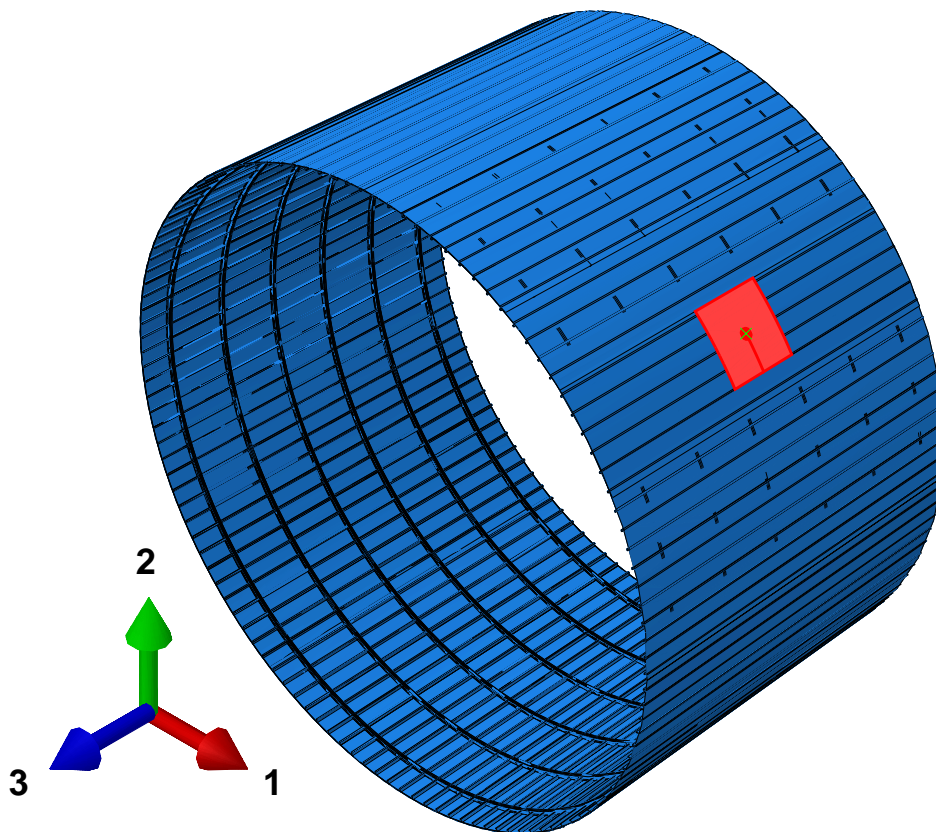


Figure 4.3: Forward center fuselage model

Figure 4.4 represents the local model of the crack area, which is the half of the highlighted red area in the full fuselage model. The center crack is located in the symmetry plane which is the Plane 1-2 in the FEM models. For clarifying the model construction better, details of the local model is illustrated in Figure 4.5 in details.

Figures 4.5a to 4.5d show the position of the broken stringer, local model structure, the center crack with broken stringer and the details of the crack respectively.

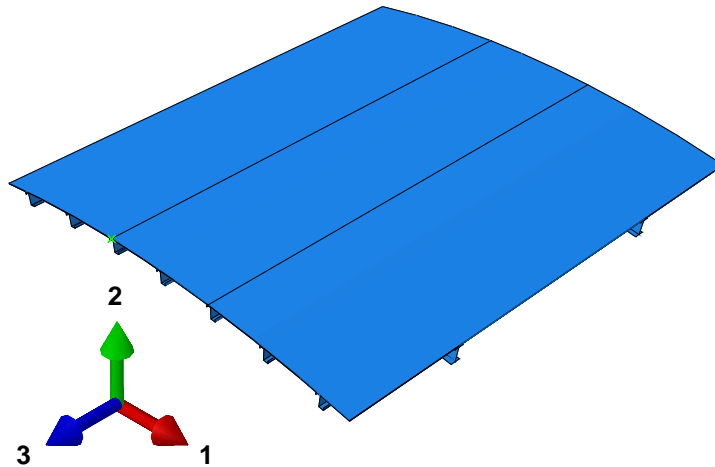


Figure 4.4: Forward center fuselage, cracked stiffened panel local model

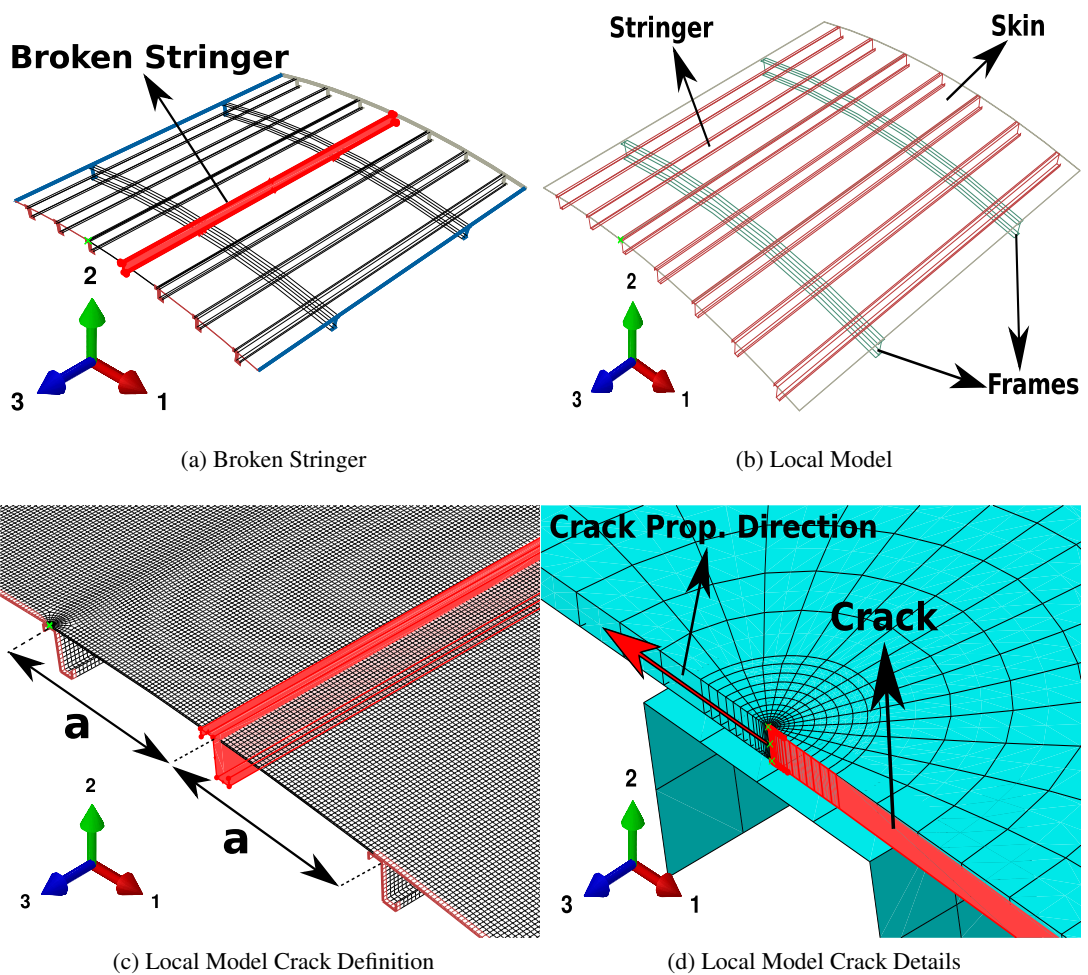


Figure 4.5: Details of the local model

For stress intensity factor evaluations to be accurate, fine mesh is needed around the crack. Focused mesh and the size of the mesh affect the precision of the stress intensity factor significantly. Therefore, fine mesh FEM model is used in the stress intensity factors calculations.

The boundary conditions and forces applied to the local modal in Figure 4.4, which represents the full fuselage modal shown in Figure 4.3, are given in Tables 4.2 and 4.3.

Table 4.2: Boundary conditions on the local model shown in Figure 4.6

BC-Front Face	$U1 = -$	$U2 = -$	$U3 = 0$	$R1 = 0$	$R2 = 0$	$R3 = -$
BC-Back Face	$U1 = -$	$U2 = -$	$U3 = -$	$R1 = 0$	$R2 = 0$	$R3 = -$
BC-Side Faces	$U1 = -$	$U2 = 0$	$U3 = -$	$R1 = 0$	$R2 = -$	$R3 = 0$
BC-Crack Surface	$U1 = -$	$U2 = -$	$U3 = -$	$R1 = -$	$R2 = -$	$R3 = -$
BC-Broken Stringer	$U1 = -$	$U2 = -$	$U3 = -$	$R1 = -$	$R2 = -$	$R3 = -$

In Table 4.2, “-” sign represents that the bounded nodes are free, and “0” sign represents that the nodes are restricted.

The cylindrical reference coordinate system is located at the origin, and  $1$  represents the radial direction,  $2$  represents tangential direction and  $3$  is the  $z$  direction.

Similarly, in Table 4.3 forces and moments in the same mutually perpendicular directions are shown by the same variables  $U1$ ,  $U2$ ,  $U3$  and  $R1$ ,  $R2$ ,  $R3$ .

Table 4.3: Applied forces on the local model shown in Figure 4.7

Axial Skin Stress	$U1 = 0$	$U2 = 0$	$U3 = 68.06MPa$	$R1 = 0$	$R2 = 0$	$R3 = 0$
Axial Stringer Stress	$U1 = 0$	$U2 = 0$	$U3 = 68.06MPa$	$R1 = 0$	$R2 = 0$	$R3 = 0$

Figures 4.6 and 4.7 respectively show the boundary conditions and the forces applied on the local model to simulate the full fuselage model under internal pressure loading condition.

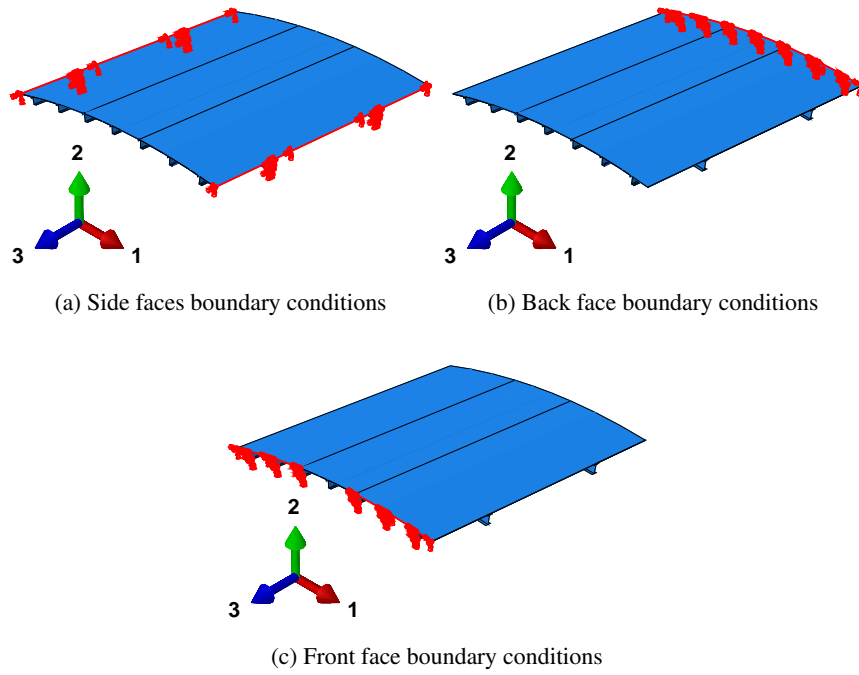


Figure 4.6: Boundary conditions applied on the local model shown in Figure 4.4

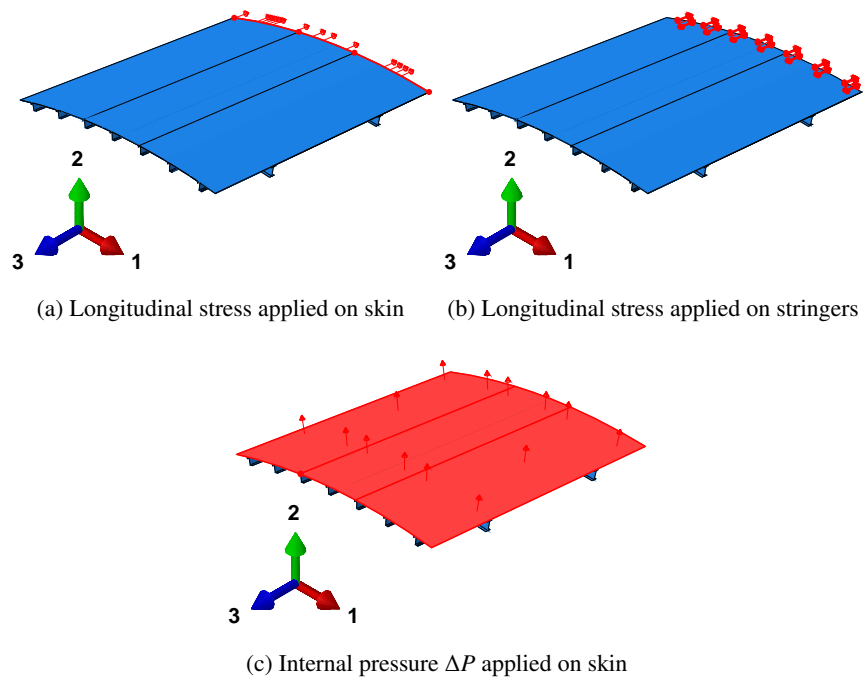


Figure 4.7: Applied forces on the local model shown in Figure 4.4

Figures 4.8 and 4.9 show the half crack model. As shown in Figures 4.8 and 4.9, symmetry boundary conditions are used instead of modeling the full structure because of the the computation time and memory considerations. In Figures 4.8 and 4.9, the edge which is not highlighted in red show the traction free edge which is corresponds to 90 mm long crack. On the other hand, the highlighted edges in red are the restricted regions where the symmetry boundary conditions are applied.

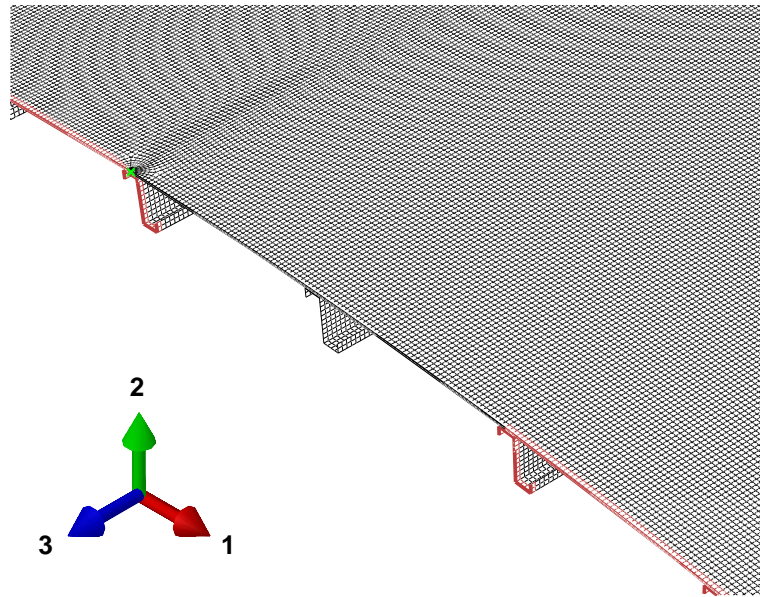


Figure 4.8: Position of the crack in the stiffened panel

Figure 4.9 shows the focused mesh is used for modeling the crack tip region. 3D contour integral crack is defined at the crack tip with mid-side node parameter 0.25 option in order to perform LEFM based SIF calculations.

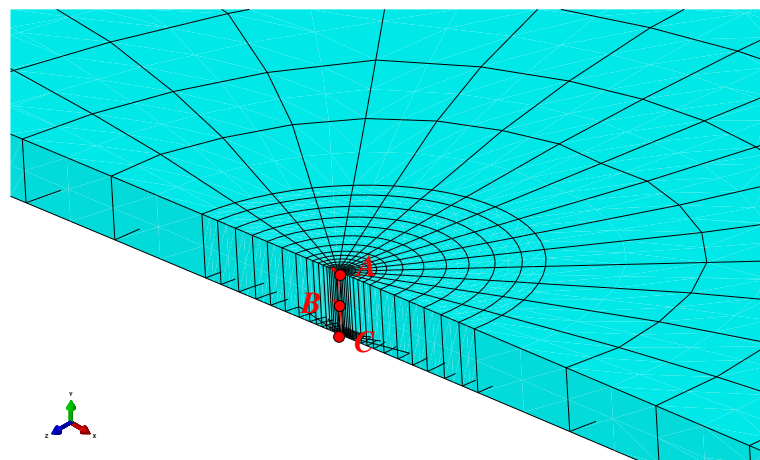


Figure 4.9: Focused mesh around the crack tip; A-B-C nodes are on the crack tip element

In the finite element model of the stiffened panel, stringers and the frames are modeled with S4R linear shell elements and the skin is modeled with C3D20R quadratic brick elements with reduced integration, which has 20 nodes.

In shell element meshes, mechanical loads which act normal to the shell surface and are applied within the contour integral domain are not taken into account in the calculation of the contour integral. For example, pressure loads are not considered because they act normal to the shell surface. Therefore, solid elements has to be used if there is out of plane loading within the contour integral region. In the Abaqus Lecture Notes [38] it is recommended that if the response is membrane dominated, the C3D20R quadratic brick elements should be preferred since these solid elements include out-of-plane loading contributions to contour integrals.

For the stress intensity factor calculation, if only one element is used through the thickness, the stress intensity factors which are calculated at nodes *A*, *B* and *C* are averaged as shown in Equation (4.8). It should be noted that stress intensity factors have to be averaged, otherwise the stress intensity factor calculation may exhibit significant path dependence [38].

$$K_{average} = \frac{K_A + 4K_B + K_C}{6} \quad (4.8)$$

In the finite element model of the stiffened panel, point based mesh independent fasteners are generated by the face to face attachment method, and finite element analysis is performed on the half symmetric model. To model the rigid riveted connection, rigid beam type connector section is defined. Stress intensity factors are calculated by the contour integration, and square root singularity option is selected to perform LEFM based SIF calculations.

#### 4.2.2.2 Analysis results

The deformed local mesh under the internal pressure loading with the closed end condition is seen in Figure 4.10. The deformation behavior is quite different from the other cases where plane sheets with stiffeners exposed to only uni-axial loading. Out of plane loading, which is the pressure in this case, changes the deformation behavior significantly, and bulges form in the skin in the regions between the stringers. In the literature this is called as bulging effect [39].

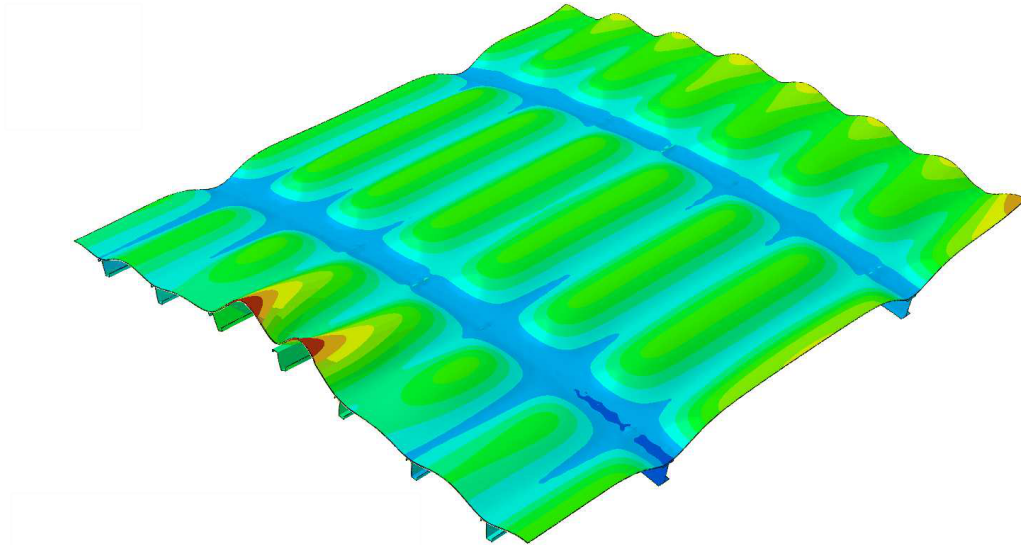


Figure 4.10: Deformed symmetric half crack model containing 90 mm crack over broken stiffener, the deformations are 4X exaggerated

So many assumptions has to be made in analytical modeling, such as calculating the effect of the internal pressure analytically considering the structure is like a pressure vessel with an open ends condition presented in Section 4.2.1. This assumption neglects the bulging of the skin which is very influential on the  $K_N$  factors. However including the internal pressure and the curvature is not done yet in the analytical modeling. Therefore obtaining SIF's with including all these effects in FEM model is more feasible, there is no need for assumptions to simplify, which is a beauty of finite element analysis. The only disadvantage of this approach is; it needs a lot of time for developing the local FEM models, computation time, and memory. Therefore, at first stages of design for parametric studies, using analytical methods for determining the stress intensity factors is more suitable but later FEM analysis should be used for a safe design.

For the stiffened curved fuselage panel under internal pressure with a closed end condition, local finite element analysis results for the variation of the stress intensity factor with the crack length is given on Figure 4.11. Figure 4.11 shows that unlike the analytical model or the finite element model with stiffened plates without curvature, normalized stress intensity factor for curved panels under internal pressure is fluctuating at a value of around 2.5. In addition, while the crack approaches a stiffener, stress intensity factor does not decrease much, as it is in the analysis done with analytical method and FEM method for the stiffened panels without curvature and internal pressure. Therefore, neglecting the bulging effect and the panel curvature, and determining the stress intensity factors only under uni-axial stress assumption in the calculation of stress intensity factors do not give reasonable results.

Results for the local FEM model analysis is included in Figure 4.11 and Table 4.4. The stress intensity factors calculated at the nodes A, B and C shown in Figure 4.9 is averaged using Equation (4.8).

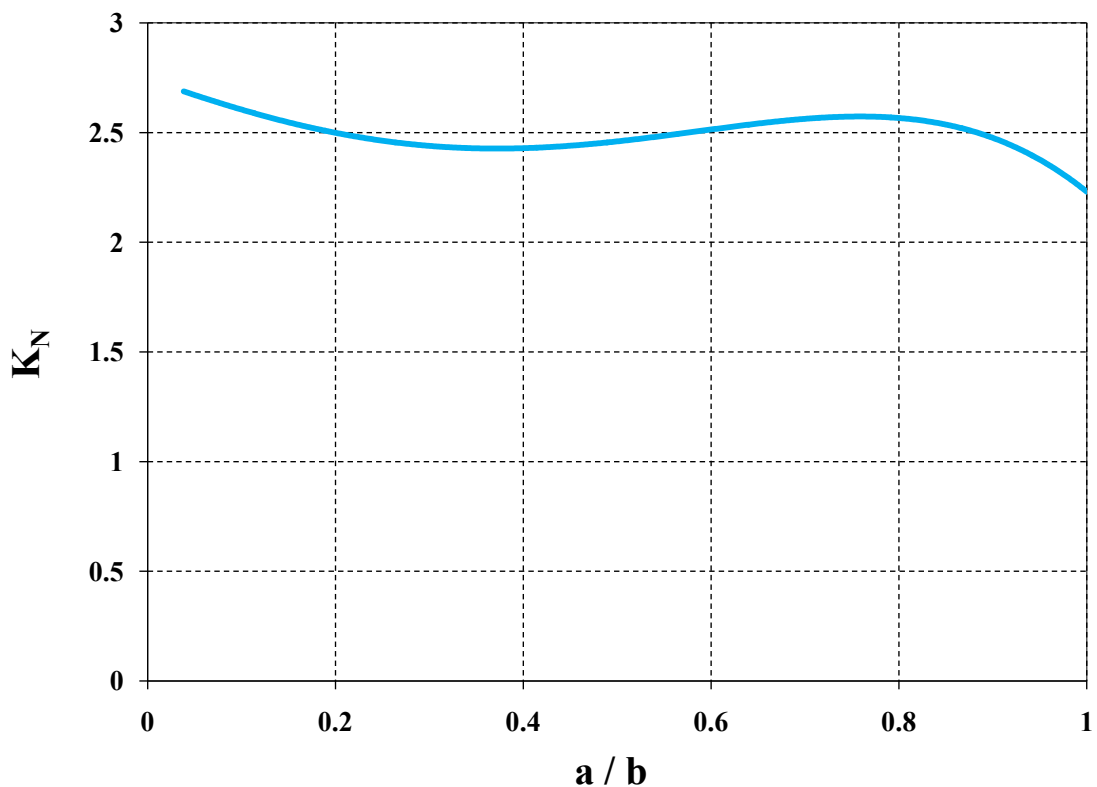


Figure 4.11: Variation of the normalized stress intensity factor with the crack lengths for the stiffened cargo A/C fuselage panels with a broken stiffener

Table 4.4: Stress Intensity Factors [ $MPa\sqrt{m}$ ] for various crack lengths [ $mm$ ] for the curved fuselage panes with a broken stiffener under internal pressure

Crack Length $mm$	a/b	$K_I(A)$	$K_I(B)$	$K_I(C)$	$K_{Average}$	$K_N$
5	0.04	1316	1438	1566	1439	2.67
10	0.08	1869	2007	2274	2029	2.66
20	0.15	2647	2728	3081	2773	2.57
30	0.23	3205	3259	3026	3211	2.43
40	0.31	3849	3727	3595	3725	2.44
50	0.38	4438	4160	3561	4107	2.41
60	0.46	4651	4562	4983	4647	2.49
70	0.54	5506	4958	4820	5026	2.49
80	0.62	5845	5327	5213	5394	2.50
100	0.77	6664	5992	6532	6194	2.57
110	0.85	6837	6228	6638	6398	2.53
120	0.92	6678	6261	7309	6505	2.46
130	1.00	5950	6154	6066	6105	2.22

The yellow line on Figure 4.13 obtained by the FEM analysis denotes the  $K_N$  factors changing with the crack length when the curved fuselage panel treated as a pressure vessel with closed ends and the stress on the skin and the stringers are calculated analytically as it is described in Section 4.2.1. This brings the assumption of neglecting the bulging effect and also only uni-axial stress contributes to  $K_N$  as in the case of analytical solution of flat stiffened panels, the only difference is the panel is curved in this case. The dotted red lines denotes the FEM results of the curved fuselage panel exposed to internal pressure described in details in Section 4.2.2.1. It is clearly seen from the Figure 4.13 that the bulging of the skin increases the  $K_N$  values considerably. Figure 4.14 illustrates the variation of  $K_N$  vs  $a/b$  curve for curved fuselage panel and the flat fuselage panel as shown in Figure 4.12 under only uni-axial loading condition.

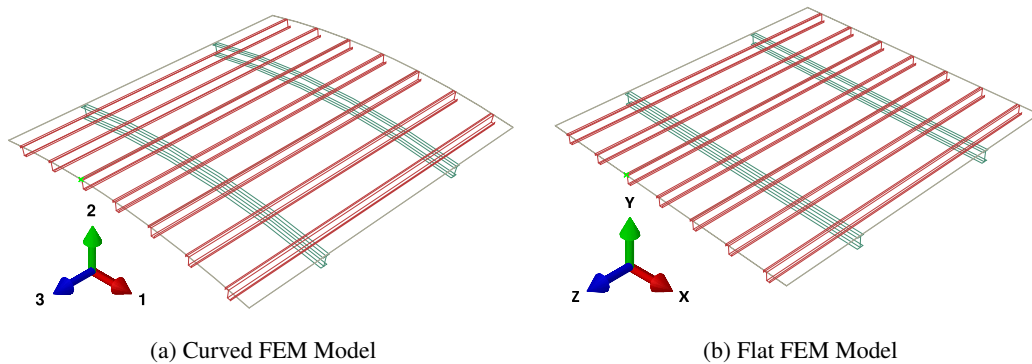


Figure 4.12: Finite element models of curved and flat fuselage panel with a broken stiffener

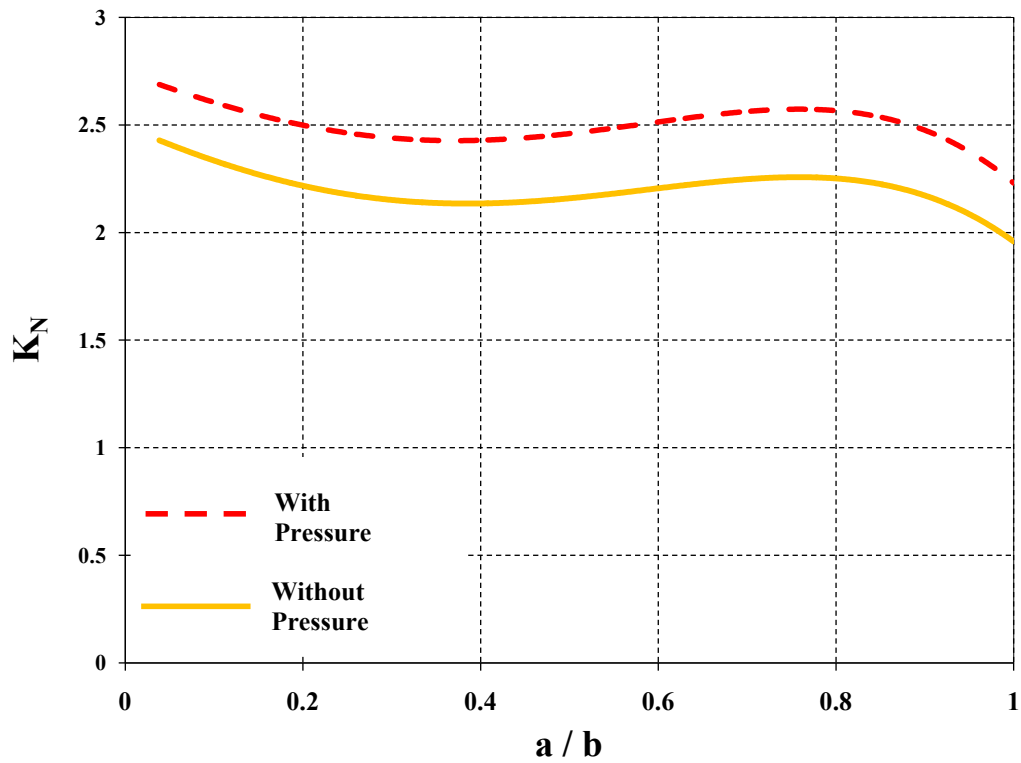


Figure 4.13: Variation of the  $K_N$  with the  $a/b$  for the stiffened fuselage panels with and without internal pressure

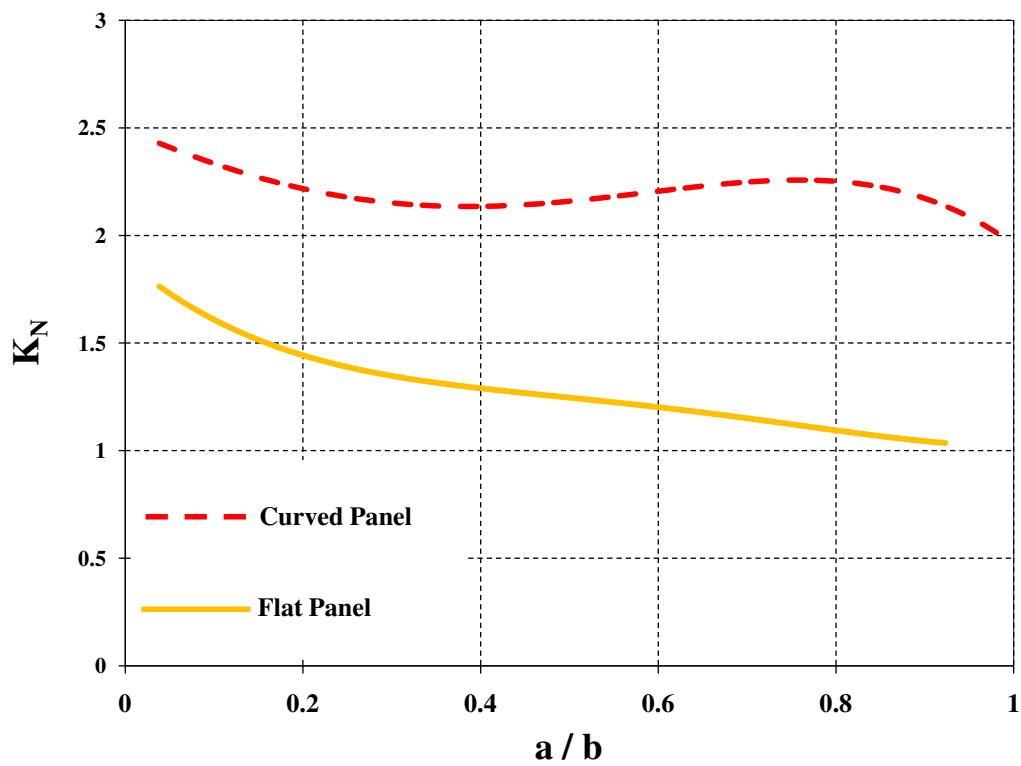


Figure 4.14: Variation of the  $K_N$  with the  $a/b$  for the stiffened fuselage panels with and without curvature under uni-axial stress

### **4.2.3 Experimental Material Characterization**

Although the material properties of the most of the aluminum alloys are available in the Military Handbook [40], most of the aircraft firms such as Airbus, always do material characterization before using the material in building aircraft [1] because, the mechanical properties of the same metal which are bought from different companies may not be the same. Therefore, in this thesis experimental material characterization is done for determining mechanical properties of the aluminum that is used in the design of sample stiffened panel.

For the life estimation of the sample stiffened panel, Al 2124 T-851 is used for both the skin material of the curved fuselage panel, stringers and frames. In this section, material characterization of Al 2124 T-851 is performed. Al-2124 T-851 block, available in the Metallurgy and Materials Engineering Laboratory is used for determining the mechanical properties, such as yield stress, fracture toughness, hardness, crack propagation data.

Al 2124 alloy is an aluminum copper alloy which is mostly produced in the form of plates. The only difference between 2024 and the 2124 is the improved production techniques used for Al 2124, therefore it has higher purity. Moreover, the elongation in short-transverse direction is also higher. As a result, Al 2124 has higher fracture toughness than Al 2024. This alloy is mostly produced in the T-851 temper, which improves the stress corrosion cracking of the material. Al 2124 also has very good mechanical properties at elevated temperatures just like Al 2024. Most of the physical properties of Al 2124 are same as Al 2024, but fracture properties Al 2124 is far better than that of Al 2024 [40].

#### **4.2.3.1 Mechanical Properties**

The mechanical and physical properties of the Al 2124 alloy with T 851 temper is available in military handbook [40]. Although the properties of the material are known, industrial firms always test them before using. Airbus company crack propagation tests showed that although the mechanical properties of the Al-2024 remains the same, the crack propagation properties are now worse than twenty years ago [1]. In this thesis study, some of the mechanical and physical properties are obtained by experiments in order to verify the material data and practice fracture testing. In addition, some of the experimentally determined material properties are also directly used in the life calculations. Room temperature plain strain fracture tough-

ness of aluminum 2124-T851 material is presented in Table 4.5. Stress intensity factors are given in British Unit System which is  $ksi\sqrt{in}$ .

Table 4.5: Room-Temperature Plane-Strain Fracture Toughness of Aluminum 2124-T851 [40]

Product Form	Orientation	Thickness Range	$K_{IC}(max)$	$K_{IC}(avg)$	$K_{IC}(min)$
Plate	L-T	0.5 – 2.5	38	29	18
Plate	T-L	0.5 – 2.0	32	25	19
Plate	S-L	0.3 – 1.5	27	21	16

The mechanical and the physical properties of the Al 2124 T-851 alloy is presented in Figure 4.15. Some of the values are used from this source and some of them will be determined from the experiments. The experiments are presented in detail in Appendix B.

Specification	AMS 4101 and AMS-QQ-A-250/29										
	Plate										
	T851										
Thickness, in.	1.000-1.500	1.501-2.000	2.001-3.000	3.001-4.000	4.001-5.000	5.001-6.000					
Basis	S	A	B	A	B	A	B	A	B	A	B
Mechanical Properties:											
$F_{tu}$ , ksi:											
L	66	66	68	65	68	65	67	64	66	63	65
LT	66	66	68	65	68	65	67	64	66	63	65
ST	64 <sup>a</sup>	64	66	63	64	62	63	61	62	58	59
$F_{ps}$ , ksi:											
L	57	57	61	57	61	56	60	55	58	54	56
LT	57	57	61	57	61	56	60	55	58	54	56
ST	55 <sup>a</sup>	55	59	55	59	54	57	53	55	51	53
$F_{cy}$ , ksi:											
L	57	57	61	56	60	55	59	53	56	52	54
LT	57	57	61	57	61	56	60	55	58	54	56
ST	...	57	61	58	62	57	61	57	60	56	58
$F_{su}$ , ksi:											
L	...	38	39	38	39	38	39	37	38	37	38
LT	...	38	39	38	39	38	39	37	38	37	38
ST	...	36	37	36	37	36	37	35	36	35	36
$F_{brs}^b$ , ksi:											
(e/D = 1.5)	...	97	100	96	100	96	99	94	97	93	96
(e/D = 2.0)	...	126	130	125	130	125	128	123	126	121	125
$F_{brs}^b$ , ksi:											
(e/D = 1.5)	...	79	84	80	85	80	85	79	84	79	82
(e/D = 2.0)	...	91	98	92	99	92	99	92	97	91	95
e, percent (S-basis):											
L	6	6	...	6	...	5	...	5	...	5	...
LT	5	5	...	4	...	4	...	4	...	4	...
ST	1.5 <sup>a</sup>	1.5	...	1.5	...	1.5	...	1.5	...	1.5	...
$E$ , 10 <sup>3</sup> ksi											
10.4											
$E_c$ , 10 <sup>3</sup> ksi											
10.9											
$G$ , 10 <sup>3</sup> ksi											
4.0											
$\mu$											
0.33											
Physical Properties:											
$\omega$ , lb/in. <sup>3</sup>											
0.100											
C, Btu/(lb)(°F)											
0.21 (at 212°F)											
K, Btu/[(hr)(ft <sup>3</sup> )(°F)/ft]											
87 (at 77°F)											
$\alpha$ , 10 <sup>-6</sup> in./in./°F											
12.6 (68°F to 212°F)											

Figure 4.15: Mechanical and Physical Properties of 2124-T851 Aluminum Alloy [40]

#### 4.2.4 Life assessment of the fuselage panel with a broken stiffener

Prediction of the life of a component under cyclic loading has been extensively studied in the literature. Various models are proposed such as Paris [41], Forman [42], Pearson [43], Walker [44], Davies and Federsen [45], Elber [46], Wheeler [47], Willenborg [48, 49, 50], and NASGRO [51, 52, 53, 54] model, for simulating the fatigue crack growth. Until the 1970s the crack growth models only considered the instantaneous events which are the loading during a single cycle, but did not consider the previous crack growth history. Elber, Willenborg and Wheeler considered the previous loading history which is called as crack retardation. Moreover, Elber also considered the crack closure effect. Crack growth retardation models take into account the variable amplitude loading. In this study, retardation models are not used, since it is more conservative to ignore the existence of a reverse cyclic plastic zone in fatigue crack growth calculations for critical aircraft components.

In this section the most commonly used three crack model is described which are the Paris and Erdođan model, Forman Model, and NASGRO Model. Neglecting the effect of retardation, the life of the stiffened panel will be calculated utilizing the Forman Model due to the convenience of determining the constants with the experiments and the success in modeling the secondary and tertiary region.

##### 4.2.4.1 Paris and Erdođan Model

Paris and Erdođan introduced a power law relationship between the crack growth rate during the experiment and the range of the stress intensity factor [41] as it is given in the Equation (4.9). This is the first, and the simplest model that can be used for crack growth calculations. The only disadvantage of using Paris and Erdođan model is that it considers only the linear region, namely the secondary region on the  $da/dN$  vs  $\Delta K$  curve, but not the primary and the tertiary region.

$$\frac{da}{dN} = C (\Delta K)^m \quad (4.9)$$

where,

$$\begin{aligned}\Delta K &= K_{max} - K_{min} \\ K &= \beta\sigma\sqrt{\pi a}\end{aligned}\tag{4.10}$$

and,  $a$  is the crack length,  $\beta$  is the geometry factor, in this thesis denoted as  $K_N$ ,  $\sigma$  is the remote stress,  $C$  and  $m$  are the material constants for Paris Erdoğan Equation. The material constants  $C$  and  $m$  can be determined following the methodology described for determining the Paris and Erdoğan Model Constants described in Section 4.2.5.

#### 4.2.4.2 Forman Model

Forman model is another power law relationship between the crack growth rate and the range of stress intensity factors but in the Forman Model the effect of the stress ratio  $R$ , and the critical fracture toughness of the material is taken into account. Determination of the Forman Constants are described in Section 4.2.5. Forman Model is used in this study for the life calculations due to the success at modeling the secondary and the tertiary region. It is also convenient to obtain the Forman Constants from the crack growth rate experiments described in Appendix B.4.

$$\frac{da}{dN} = \frac{C (\Delta K)^m}{(1 - R) K_{CR} - \Delta K}\tag{4.11}$$

where,

$$R = \frac{S_{min}}{S_{max}}$$

$K_{CR}$  is the critical fracture toughness of the material,  $S_{max}$  and  $S_{min}$  are the maximum and the minimum remote stress in one cycle respectively,  $C$  and  $m$  are the Forman constants.

#### 4.2.4.3 Nasgro Model

The equation for crack growth used in NASGRO (Version 3.0) is developed by Forman and Newman at NASA, De Koning at NLR, and Henriksen at ESA [53, 54, 55].

$$\frac{da}{dN} = C \left[ \left( \frac{1-f}{1-R} \right) \Delta K \right]^n \left( \frac{1 - \frac{\Delta K_{th}}{\Delta K}}{1 - \frac{K_{max}}{K_{cr}}} \right)^p \quad (4.12)$$

C, n, p, and q are empirically derived, and  $f$  is:

$$f = \frac{K_{op}}{K_{max}} = \begin{cases} \max(R, A_0 + A_1R + A_2R^2 + A_3R^3) & R \geq 0 \\ A_0 + A_1R & -2 \leq R < 0 \\ A_0 - 2A_1 & R \leq -2 \end{cases}$$

where,  $A_i$  coefficients are:

$$\begin{aligned} A_0 &= \left( 0.825 - 0.34\eta + 0.05\eta^2 \right) \left[ \cos \left( \frac{\pi}{2} S_{max}/\sigma_0 \right) \right]^{\frac{1}{\eta}} \\ A_1 &= (0.415 - 0.071\eta) S_{max}/\sigma_0 \\ A_2 &= 1 - A_0 - A_1 - A_3 \\ A_3 &= 2A_0 + A_1 - 1 \end{aligned}$$

where,

$\eta$  : Plane stress/plane strain constraint factor

$S_{max}/\sigma_0$  : The ratio of the maximum applied stress divided by the flow stress

$K_{op}$  : Opening stress intensity factor, above which the crack is open

$K_{max}, K_{min}$  : Maximum and minimum stress intensity factors in a cycle

$K_{CR}$  : Critical stress intensity for fracture

$K_C$  : Fracture toughness at plane stress condition

These values are provided by the NASGRO material database. Crack growth rate tests, which are presented in Appendix B.4 showed that, the  $da/dN$  vs  $\Delta K$  curve AFGROW proposing is very close to the test results. Therefore there is no need to re-calculate the coefficients for the NASGRO equation but they will be used as it is in this study.

$$\Delta K_{th} = \Delta K_0 \left( \frac{a}{a + a_0} \right)^{\frac{1}{2}} / \left( \frac{1 - f}{(1 - A_0)(1 - R)} \right)^{1 + C_{th}R} \quad (4.13)$$

where,

- $\Delta K_{th}$  : threshold stress intensity factor range
- $\Delta K_0$  : threshold stress intensity factor range at  $R = 0$
- $a$  : crack length
- $a_0$  : intrinsic crack length ( 0.0015 in or 0.0000381 m)
- $C_{th}$  : threshold coefficient

$\Delta K_0$  and  $C_{th}$  are also provided by the NASGRO material database.

NASGRO takes into account the thickness by Equation (4.14).

$$\frac{K_{cr}}{K_{Ic}} = 1 + B_k e^{-\left(A_k \frac{t}{t_0}\right)^2} \quad (4.14)$$

- $K_{Ic}$  : Plain strain fracture toughness
- $A_k$  : Fit parameter
- $B_k$  : Fit parameter
- $t$  : Thickness
- $t_0$  : Reference thickness (Plain strain condition)

#### 4.2.5 Determination of Critical Fracture Toughness and Crack Constants

Using the crack growth rate data obtained from the experiment which is presented in Appendix B.4 in details,  $da/dN$  vs  $\Delta K$  graph is prepared. It should be noted that  $da/dN$  vs  $\Delta K$  curve is drawn in logarithmic scale. As it can be seen from the Figure 4.16, crack propagation may be divided into three phases, which are primary region, secondary region and tertiary region. Paris and Erdoğan observed that the secondary region is almost linear [41]. Crack spends most of the time in the secondary region, therefore many crack propagation models uses the linearity of the secondary region such as the Paris and Erdoğan and Forman model given by Equations (4.9) and (4.19).

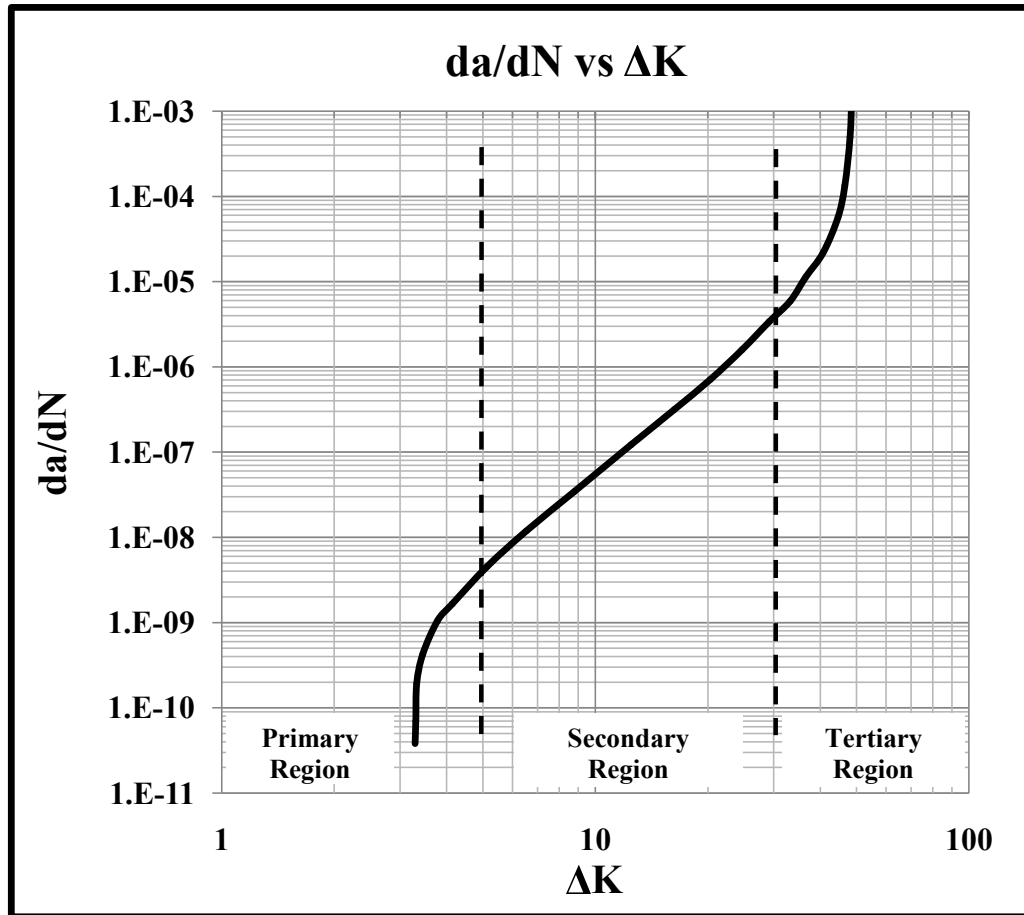


Figure 4.16:  $da/dN$  vs  $\Delta K$  curve for Al 2124-T851

#### 4.2.5.1 Determination of Critical Fracture Toughness

Determination of the plain strain fracture toughness of the Aluminum 2124-T851 for  $T$ - $L$  direction which is  $24.3 \text{ MPa} \sqrt{\text{m}}$ , is explained in detail in the experimental study in Appendix B.3.

It is known that the critical fracture toughness is a function of the plain strain fracture toughness and the thickness, therefore for 1 mm sheet, which is the thickness of the curved fuselage panel, critical fracture toughness should be calculated. The formulation presented in NASGRO 4 [54] is utilized for determining the critical fracture toughness of the 1 mm sheet  $K_{CR}$ .

$$K_{CR}/K_{IC} = 1 + B_k e^{-(A_k t/t_0)^2} \quad (4.15)$$

$$t_0 = 2.5 (K_{IC}/\sigma_{ys})^2 \quad (4.16)$$

$A_k, B_k$  : Fit parameters  
 $\sigma_{ys}$  : Yield stress

$A_k$  and  $B_k$  parameters are recommended to be 1 in the NASGRO and AFGROW database, therefore they are assumed to be 1. Using the Equation (4.15), and substituting the numerical values, for 1 mm thickness, fracture toughness  $K_{CR}$  comes out to be  $48.1 \text{ Mpa} \sqrt{\text{m}}$ .

#### 4.2.5.2 Determination of the Paris and Erdoğın Constants

As it is described in section 4.2.4.1, the crack growth rate is related to the  $\Delta K$  linearly proportional in secondary region. The Paris and Erdoğın Constants which are C and m are the two unknowns in the Equation (4.17). Picking two points from the  $da/dN$  vs  $\Delta K$  graph which is obtained from the experiment explained in detail in Appendix B.4, and solving the equations simultaneously C and m can be obtained.

$$\frac{da}{dN} = C (\Delta K)^m \quad (4.17)$$

Natural logarithm of the both side in Equation (4.17) is taken to get a linear equation which is given in Equation (4.18).

$$\ln\left(\frac{da}{dN}\right) = \ln(C) + m \ln(\Delta K) \quad (4.18)$$

Substituting numerical values and solving the equations simultaneously, Paris and Erdoğın Constants are obtained, and given in Table 4.6.

Table 4.6: Paris and Erdoğın Constants for Al 2124 T-851

$C$	$1.31911 * 10^{-11}$
$m$	3.61911

#### 4.2.5.3 Determination of the Forman Constants

The Forman Equation is already presented in Section 4.2.4.2. Similar like the Paris and Erdoğın Constants; Forman Constants, C and m will be obtained by picking up two points

from the linear region on the  $da/dN$  vs  $\Delta K$  graph obtained from the experiment which is presented in Appendix B.4, and solving the Equation (4.19) simultaneously for these points.

Note that Equation (4.19) includes  $K_{CR}$  and the  $R$  terms apart from the Paris and Erdoğan Equation. Knowing that the crack growth rate tests discussed in Appendix B.4 are done with  $R = 0$ , the only term to be calculated before obtaining the Forman Constants is  $K_{CR}$ . Determination of the  $K_{CR}$  from the  $K_{IC}$  is described in Section 4.2.5.1. Therefore, obtaining the fracture toughness  $K_{IC}$  and  $\sigma_{ys}$  from the experiments which are respectively included in Appendix B.2 and Appendix B.3, and utilizing the methodology described in Section 4.2.5.1, the critical fracture toughness  $K_{CR}$  can be obtained. The crack growth rate tests are done with 12.7 mm specimens, therefore  $K_{CR}$  is calculated for  $t = 0.0127m$ , which is  $24.6 MPa \sqrt{m}$ .

$$\frac{da}{dN} = \frac{C (\Delta K)^m}{(1 - R) K_{CR} - \Delta K} \quad \text{where,} \quad R = \frac{S_{min}}{S_{max}} \quad (4.19)$$

$t$  : Thickness.

$K_{CR}$  : Critical fracture toughness of the material at thickness  $t$ .

$K_{IC}$  : Plain strain fracture toughness.

$S_{max}, S_{min}$  : The maximum and the minimum remote stress in one cycle respectively.

$C, m$  : Material parameters known as Forman constants .

Natural logarithm of the both side in Equation (4.19) is taken to get a linear equation which is given in Equation (4.20).

$$\ln\left(\frac{da}{dN}\right) = \ln C + m \ln \Delta K - \ln(K_{CR} - \Delta K) \quad (4.20)$$

Performing the necessary manipulations, substituting numerical values and solving the equations simultaneously, Forman constants are obtained, and given in Table 4.7.

Table 4.7: Forman Constants for Al 2124 T-851

$C$	$8.09735 * 10^{-10}$
$m$	3.36876

#### 4.2.6 Life Calculation with AFGROW

Details of the crack growth calculations, and the results of the analysis are presented in this section. Although it is almost impossible that the skin and the stringer contains a  $1.27\text{ mm}$  crack at the same time, in order to be on the conservative side, it is assumed that both sheet and the stringer have an initial crack of  $1.27\text{ mm}$  in length. The reason why the crack starts with a  $1.27\text{ mm}$  length is that, it is the smallest crack length that the NDT inspection can detect during the maintenance periods.

The uni-axial loading of the fuselage panels, is caused by the  $\Delta P$  loading with a closed end condition, as it is mentioned in Section 4.2.1 results in  $68\text{ MPa}$  constant cyclic loading with the stress ratio  $R = 0$  on the skin and the stringers, therefore knowing the stress spectrum and the stress intensity factors for the specified geometry, fatigue life can be calculated.

The crack growth calculations are performed by the crack propagation program AFGROW (Air Force Growth) which is a crack propagation prediction software enables to analyze fatigue life of the metallic structures [56]. AFGROW is mostly used in Aerospace applications for predicting the fatigue life of a component. The stress intensity factor library contains over 30 different simple but useful crack geometries. There are a lot of critical scenarios, which may occur during the service life of the aircraft, and engineers have to predict the possible critical scenario to prove that the A/C is still safe even if that critical scenario becomes reality. In this sample calculation, the critical scenario chosen for the life calculation consists of two stages.

The life prediction results presented in this section are obtained utilizing the Forman and NASGRO Model as explained respectively in Sections 4.2.4.2 and 4.2.4.3, but the life prediction methodology is described with presenting the detailed results of AFGROW utilizing the Forman Equation. The results of the NASGRO Equation is also presented in this section.

*Stage 1(a)* : Two double cracks start from the skin and the stringer at the same time. Stage 1(a) is illustrated in Figure 4.17. For the AFGROW life calculations for this stage, for both skin and stringer, an application defined double through crack at a hole model, which is illustrated in Figure 4.20a, is used. The crack propagation is done under  $68\text{ MPa}$  uni-axial constant cyclic loading, with Forman and NASGRO crack growth model with plain stress option.

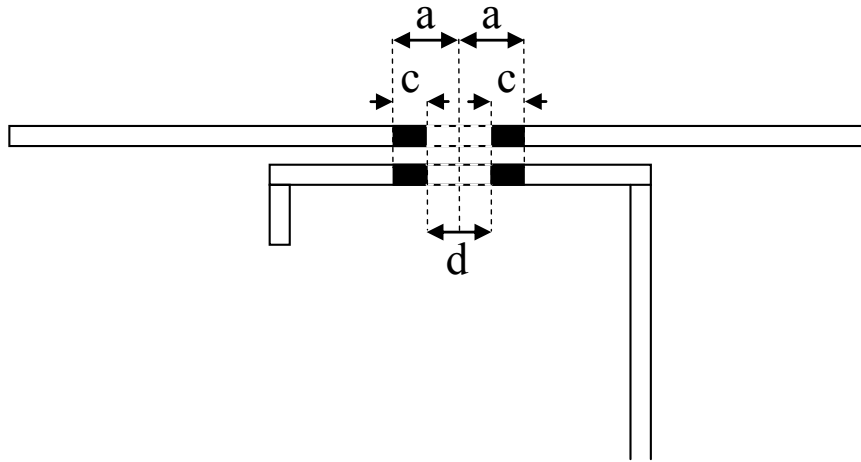


Figure 4.17: Stage 1(a): Double crack starts from a hole on the skin and the stringer at the same time

*Stage 1(b)* : After the propagation of the cracks, one of the crack on the stringer, which is close to the free end, completely breaks one side of the stringer with a brittle fracture as the SIF reaches  $K_C$ . From there on, crack on the stringer can be treated as an edge crack which is shown on Figure 4.18. The new crack on the stringer is modeled with a application defined edge through crack as shown in Figure 4.20b. It should be noted that at this stage, the skin is still modeled with application defined double through crack at a hole.

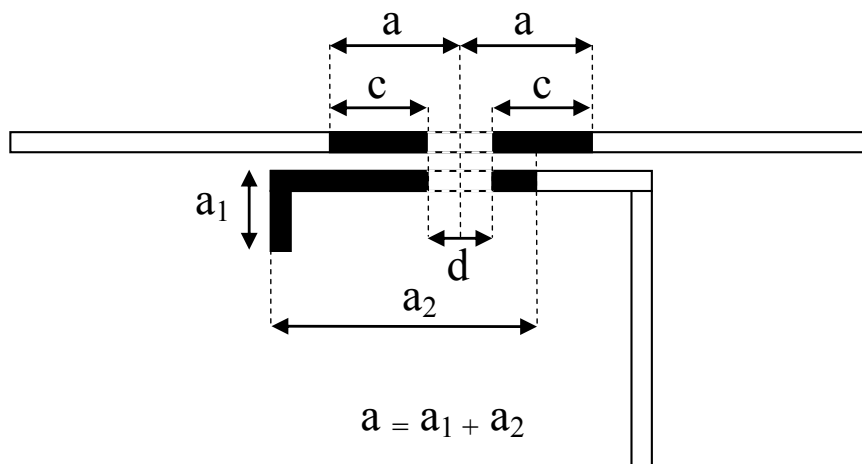


Figure 4.18: Stage 1(b): Center crack on the stringer breaks through to the edge; crack on the stringer becomes an edge crack

*Stage 2* : This stage starts when the edge through crack at Stage 1(b) reaches its final length and the stringer is completely broken. Up to Stage 2 application defined models of AFGROW are used with an assumption of constant cyclic stress on both skin and stringer. For these cases, AFGROW has its own stress intensity history. However, after the stiffener failure, the whole picture changes, and since the stiffener carries no more load, this situation affects the the stress intensity factors tremendously. For this stage, using the application defined models of the AFGROW just like Stage 1 is not suitable. Therefore, finite element model is developed and the stress intensity factors are obtained for this geometry as explained in Section 4.2.2. As illustrated on Figure 4.19 the center through crack model is used with SIF correction for this stage.

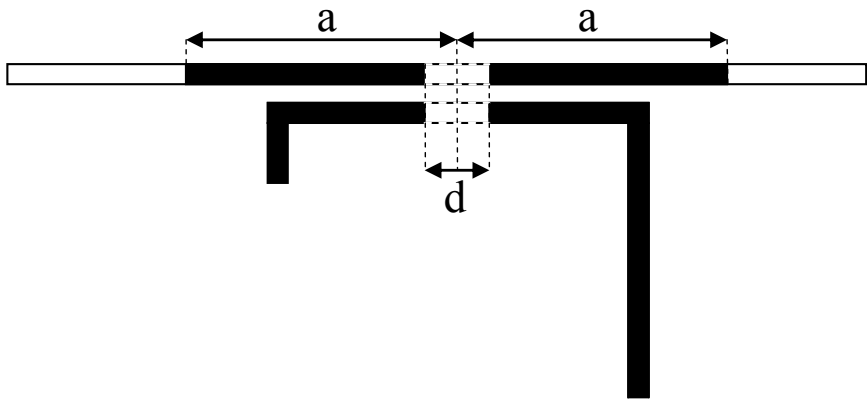


Figure 4.19: Stage 2: Stringer is completely broken, and the crack propagates on the skin

Figures 4.20a to 4.20c shows the built in AFGROW models which are used in crack growth calculations.

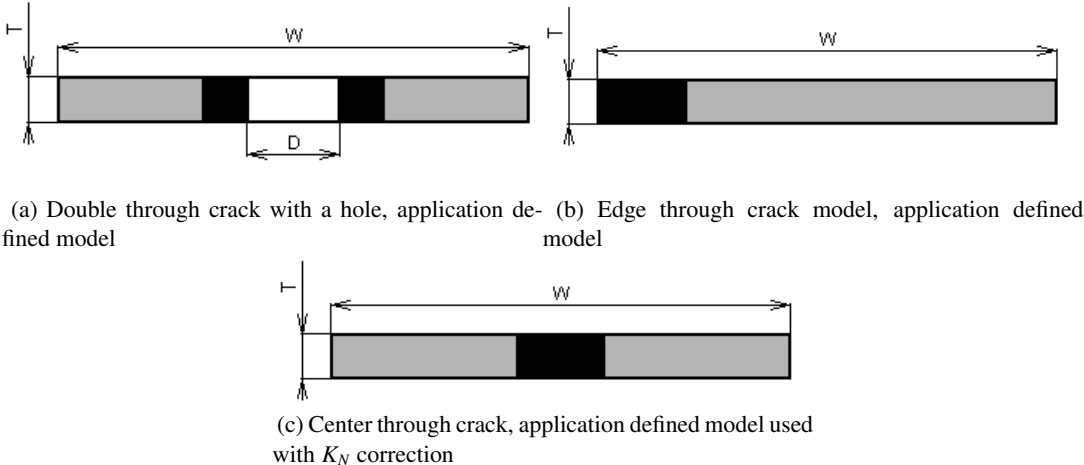


Figure 4.20: Applied forces on the local model shown in Figure 4.4

### 4.3 Analysis Results of AFGROW

#### 4.3.1 Stage 1

*Stage 1* starts with an initial through crack, of length  $1.27\text{ mm}$ , on both sides of skin and stringer rivet hole at the same time. As it is noted before, crack length of  $1.27\text{ mm}$  which is the smallest crack length which can be detected with NDT.

*Stage 1(a)* is the stage that the symmetric double crack starts and propagates from the stringer rivet hole as it is illustrated on Figure 4.17 until the crack reaches the closer end of the stringer. In this stage when the crack length reaches a value of  $c_f = 6.9\text{ mm}$  Net Section Yielding failure occurs therefore it is assumed that the crack reaches to the closer end. The results of the AFGROW analysis are presented for Stage 1(a) in Table 4.8.

Table 4.8: Stage 1(a): Double through crack propagating on the stringer, Forman Eq.

$w_{eff}$	$20\text{ mm}$
$d$	$2.5\text{ mm}$
$t$	$2\text{ mm}$
$c_i$	$1.27\text{ mm}$
$c_f$	$6.9\text{ mm}$
$a_i$	$2.52\text{ mm}$
$a_f$	$8.15\text{ mm}$
N	$174800\text{ Cycles}$

where,

$w_{eff}$  : Twice the distance from the rivet center line to the closer end of the stringer including the stringer vertical flange length for Stage 1(a)

$d$  : Rivet hole diameter

$t$  : Thickness defined in Figures 4.20a to 4.20c

$c_i$  : Initial crack length at the beginning of the stage measured from the edge of the rivet hole as shown in Figure 4.20a

$c_f$  : Final crack length at the end of the stage measured from the edge of the rivet hole

$a_i$  : Initial crack length at the beginning of the stage, measured from the center of the rivet hole

- $a_f$  : Final crack length at the end of the stage, measured from the center of the rivet hole
- N : Number of cycles

As explained before, Stage 1(a) starts with two double crack at the edge of the rivet diameter on both skin and stringer. After the crack propagates, crack on the stringer, which is closer to the free end of the stringer, reaches to the free end with a brittle fatigue fracture which is the end of the Stage 1(a). Crack propagation results for the stringer for Stage 1(a) are presented in Table 4.8.

Stage 1(b) starts after the one of the crack which is closer to the free end of the stringer reaches to the free end. Therefore, in Stage 1(b), crack on the stringer can be treated as an edge through crack. After a while of propagation of the crack, the stringer is completely broken with a brittle fracture again with a brittle fracture due to the SIF reaching the  $K_{CR}$ , which is the end of the Stage 1(b). In AFGROW life calculations, application defined edge through crack model is used, as illustrated in Figure 4.20b. Stage 1(a) ends with a final crack length of  $a_f = 8.15 \text{ mm}$  and one side of the stringer including the vertical length is completely broken which is  $10 \text{ mm}$ . Therefore, the initial edge crack length for the Stage 1(b) for the stringer is  $a_i = 18.15 \text{ m}$ .

Table 4.9: Stage 1(b): Edge through crack propagating on the stringer, Forman Eq.

$w_{eff}$	55 mm
d	2.50 mm
t	2 mm
$c_i$	6.9 mm
$c_f$	-
$a_i$	18.15 mm
$a_f$	26.24 mm
N	1246 Cycles

Note that the effective width  $w_{eff}$  defined here is the total length of the stringer including all horizontal and vertical members. Because the double through crack turns to be a edge through crack at the end of this stage  $c_f$  is not applicable, and  $a_f$  here is the length which is described as  $a = a_1 + a_2$  in Figure 4.18.

The AFGROW crack propagation analysis results of the Stage 1(a), and Stage 1(b) are presented respectively in Tables 4.8 and 4.9. It should be noted that at the same time, skin crack

also propagates during Stages 1(a) and 1(b). Summing up the number of cycles for Stage 1(a) and Stage 1(b), total number cycles for Stage 1 can be obtained.

$$N_{Stage1} = N_{Stage1(a)} + N_{Stage1(b)} \tag{4.21}$$

$$N_{Stage1} = 176046 \text{ Cycles} \tag{4.22}$$

After obtaining the total number of cycles at Stage 1, and utilizing the application defined AFGROW double through crack at a hole model, as illustrated in Figure 4.20a, the final crack length on the skin at the end of Stage 1 is calculated propagating the initial crack of 1.27 mm cracks for 176046 cycles. Crack growth analysis results for the skin during Stage 1 is presented in Table 4.10. It is seen that during Stage 1, the crack reaches to a length of 4.62 mm ( $a_f = 4.62 \text{ mm}$ ) in 176046 cycles on the skin.

Table 4.10: Stage 1: Double through crack at the rivet hole propagating on the skin, Forman Eq.

$w_{eff}$	262 mm
d	2.50 mm
t	1 mm
$c_i$	1.27 mm
$c_f$	3.37 mm
$a_i$	2.52 mm
$a_f$	4.62 mm
N	176046 Cycles

**4.3.2 Stage 2**

Stage 2 starts right after the stiffener failure. In Stage 2, crack propagates very fast, because the broken stiffener is no more carrying the load, moreover it causes a tremendous increase in stress intensity factors.

In AFGROW model database, there is no built in model for simulating such a complicated geometry. Therefore, stress intensity factors are obtained using finite element method, as explained in Section 4.2.2, and they are used in the AFGROW center through crack model shown in Figure 4.20c as a  $\beta$  correction factor, in this thesis defined as  $K_N$ . Now the AFGROW

is not calculating the stress intensity factors but directly uses the values obtained from the finite element analysis.

AFGROW crack propagation results for Stage 2 are presented in Table 4.11. The crack propagates from 4.62 mm to 25.8 mm in  $N = 4360$  Cycles until the brittle fracture occurs due to the stress intensity factor reaching to the critical value  $K_{CR}$ . Analysis showed that in Stage 2, crack propagates very fast comparing with the Stage 1.

Table 4.11: Stage 2: Center through crack propagates on the skin, Forman Eq.

$w_{eff}$	262 mm
d	2.5 mm
t	1 mm
$c_i$	-
$c_f$	-
$a_i$	4.62 mm
$a_f$	25.75 mm
N	4360 Cycles

Summing up the number of cycles at Stage 1 and Stage 2, the fatigue life of the stiffened panel is calculated as  $N = 180406$  flight cycles. The crack propagation vs flight cycles graph is given in Figure 4.21 which clearly shows that crack propagates very fast in Stage 2. The life prediction result using the NASGRO equation with the constants available in database is also presented in Figure 4.22.

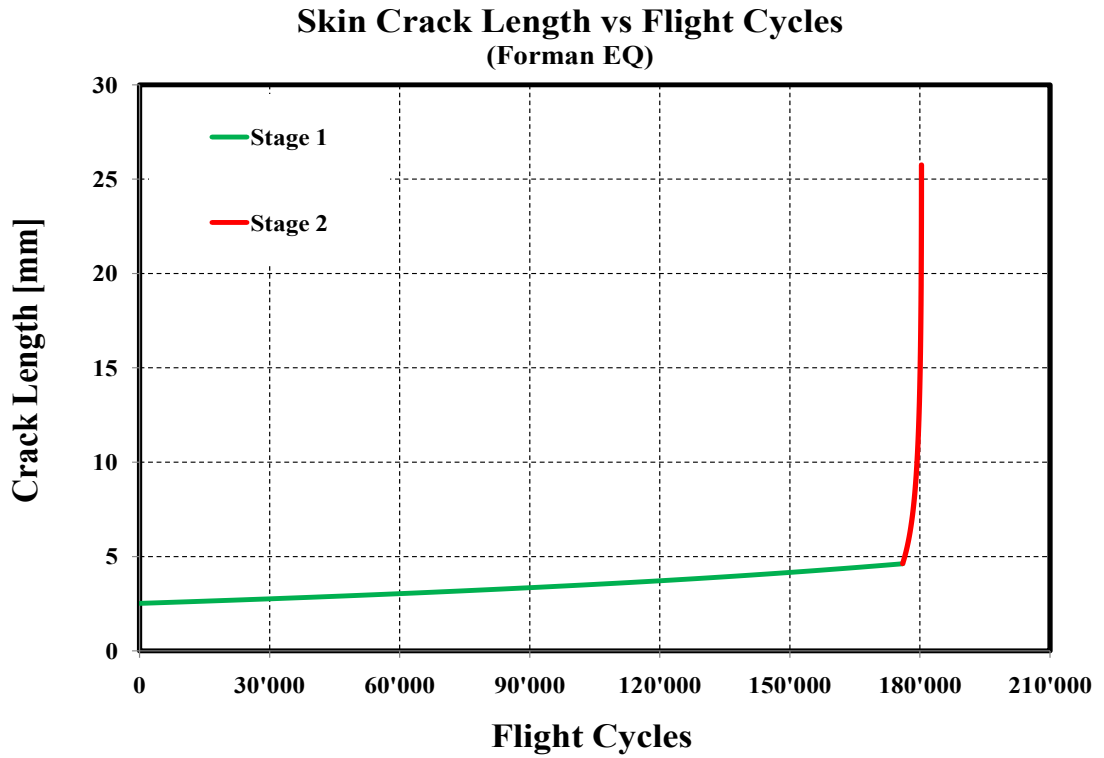


Figure 4.21: Crack growth time history for the skin, utilizing Forman Equation with experimentally determined constants

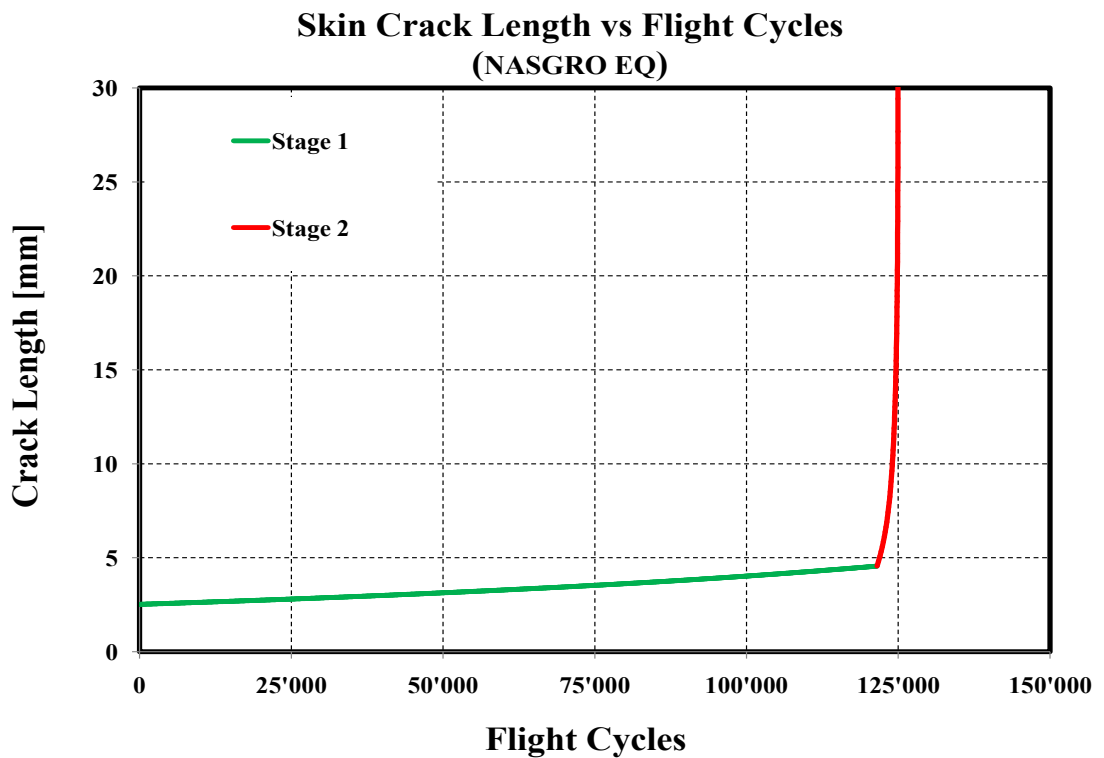


Figure 4.22: Crack growth time history for the skin, utilizing NASGRO Equation with using the constants available in database

### 4.3.3 Conclusion

The method of inspection, and the interval between inspections depends on damage tolerance capability of the design. The best damage tolerant designs always provides long fatigue life and slow crack growth. Slow crack growth enables the manufacturer to set longer inspection intervals, because although there may be a crack propagating, it is known that the crack will not get to the critical length rapidly. The method and the intervals of inspection has significant effect on maintenance cost of the aircraft, such as the maintenance using visual inspection is far cheaper than maintenance with NDT. Although NDT is more precise than the visual inspection, it needs more money and time.

It is noted that since the crack propagates very fast in Stage 2, detecting the crack before it gets critical needs considerable effort and money. Therefore, the design should be changed. Because the crack rapidly speeds up in Stage 2, to catch the crack before it gets critical, the inspection intervals should be close which will increase the maintenance cost.

Decreasing the stiffener thickness may be a solution to this problem, because as the stiffness ratio increases, the portion of the load that the stiffener carries increases, and as discussed in Section 2.3.5 stress intensity factor increases until  $a/b \approx 1$  for broken stiffener configuration. Note that remote stress on skin will increase, if the stiffness ratio is to be decreased.

Thicker skin and stringer may be used to reduce the remote stress. It should be noted that, the normalized stress intensity factor for the 3D model of the fuselage structure is different from the analytical solution and the Franc 2D/L solution. The bulging effect and the curvature effect are the responsible for the crack to move very fast in Stage 2.

## CHAPTER 5

### CONCLUSION

Comparative study of stress intensity factor calculations in cracked sheets with riveted stringers, by the analytical and finite element method, is presented. Three main crack configurations are studied. In the first two configurations, stiffeners are intact and crack in the sheet exists in between two intact stiffeners and underneath the intact stiffener. The third configuration studied involves the crack in the sheet just under the broken stiffener. In the first part, details of the analytical solution is given, and all the equations of the analytical study of Poe [6] are re-derived. In the first part of the thesis, the sources of the typographical errors in the original study of Poe [6] for the intact stiffener configurations, are shown and corrections are made.

In the second part of the thesis, a finite element modeling methodology is developed for the infinite width stiffened panels, which can be easily adapted for the finite width stiffened panels. Finite element based stress intensity factor calculations are performed by *Franc2D/L* and *Abaqus*, and in general, very good agreement is observed between the analytical, *Franc2D/L* and *Abaqus* results for the various case studies pertaining to the intact stiffener configurations. For the broken stiffener case, analytical solution of stress intensity factors by Poe [7] is checked against *Franc2D/L* only. Very good agreement is found between the analytical solution of stress intensity factors for the broken stiffener case by Poe [7], and *Franc2D/L* results. Some main conclusions drawn from the analytical and finite element study of stiffened cracked plates with intact and broken stiffeners are highlighted below.

- Increasing rivet flexibility increases the stress intensity factor. Therefore, assuming rigid connector elements is not a conservative approach in fracture mechanics analysis of riveted structures.

- It is found that by increasing the rivet diameter, stress intensity factors decrease slightly. This conclusion is verified by both analytical and finite element analysis.
- For large values of rivet pitch, rivet forces cause a steady decrease in the stress intensity factor because crack tip is farther away from the closest rivet. On the other hand, for small values of rivet pitch when the crack moves away from a stringer, stress intensity factor increases. Similarly when the crack approaches to the stringer the stress intensity factor decreases. This is because, since rivets are closer to the crack tip, rivet forces are more influential on the crack tip stresses. Therefore, when the crack moves away from a stringer, stress intensity factor increases because of increase of stress in the vicinity of the crack and for a crack approaching the stiffener, the stress intensity factor decreases due to the decreasing stress on the crack tip vicinity.
- The most significant effect on the stress intensity factor is seen when stringer-cracked sheet offset is included in the analysis model. This is due to the additional moment effect of the stringer loads on the cracked sheet, and stress intensity factors increase significantly when stringer-sheet offset is included in the analysis.
- As the stiffener gets stiffer and when the crack tip is close to the broken stiffener, the stress intensity factor becomes very high. Very much increase of the stress intensity factors near the stiffer broken stiffener is considered to be mainly due to the fact that the stiffer stringers carry more load, and the broken stiffener tends to open up the crack.
- When the crack moves away from the broken stiffener and approaches to the neighboring intact stiffeners, the rivet forces at the intact stiffeners act on the sheet such that they tend to close the crack. Since the stiffer stringer is loaded more compared to the less stiff stringer, away from the broken stiffener stress intensity factor becomes less for the sheet reinforced with stiffener stringers, compared to the stress intensity factor for the sheet reinforced with less stiff stringers.

In the last part of the thesis, a sample life calculation of the fuselage panels with a broken stiffener is performed for a cargo airplane. The aim of the study was to highlight the importance of determination of the stress intensity factors for complex geometries for which stress intensity factors are not available. For this purpose, a curved fuselage panel with frames and stringers is analyzed by Abaqus. Stress intensity factor versus crack length data is obtained

by the finite element analysis of the pressurized fuselage panel with a broken stiffener under the cracked fuselage panel. It is seen that unlike the flat panels under uni-axial load, in the pressurized fuselage panel, stress intensity factors along the crack length remains almost constant and does not decrease as the crack approaches to an intact stringer. Bulging effect and the curvature effect are considered to be the main reasons for this behavior. However, as the crack approaches the broken stiffener, increase in the stress intensity factor is observed as it is in the flat plate case under uni-axial loading. Life assessment of the fuselage panel with a broken stiffener is performed in two stages. In Stage 1 the crack on the stringer is let to grow until the stiffener is completely broken. Application defined crack models of AFGROW are used to estimate the life until the stiffener is completely broken up. After the stiffener is broken, stress intensity factor versus crack length data obtained by the finite element analysis is employed in the NASGRO crack growth model to estimate the remaining life of the panel. Based on the sample case study, it is seen that after the stiffener is broken, because of the increase of the stress intensity factors for the cracked panel, crack propagates very fast in the panel.

For the sample fuselage panel studied, it is concluded that if the stiffness of the broken stiffener is decreased, stress intensity factors of the cracked panel decreases for the  $a/w$  is in between nearly 0 and 1. This conclusion was verified both by the analytical study of Poe [7] and finite element analysis by Franc2D/L. However, in real life applications it may not be always possible to predict the location of the broken stiffener. Therefore, decreasing the remote stress by increased skin and stringer thickness may also be a remedy to prevent the fast growth of the crack in Stage 2.

As a final conclusion, the main contributions of the thesis are listed below.

- An analytical tool is developed for determining stress intensity factors of stiffened infinite size plates for any rivet pitch, stringer pitch, rivet diameter and total stringer stiffness to total plate stiffness ratio. Therefore, for the intermediate geometrical values of the stiffened plate, there is no need for interpolation to determine the stress intensity factors from the charts presented in Poe's reports [6], [7].
- Sources of the typographical errors in the original study of Poe [6] are shown and corrections are made.

- Finite element model is developed to simulate infinite size cracked stiffened sheets, and stress intensity factor versus crack size data are obtained for different crack and geometrical configurations. Finite element modeling technique can be easily implemented to complex geometries, and the variation of the stress intensity factor with the crack length can be determined for complex real life geometries.
- A sample fatigue life estimation example is demonstrated for a stiffened fuselage panel with a broken stiffener. It is shown that for complex geometries, determination of stress intensity factor can not be possible using tools as such as AFGROW. Therefore, determining the stress intensity factor data by the finite element analysis is very crucial in assessing the structural integrity and also in calculating the fatigue life of critical structural components. The example on the fatigue life estimation of the fuselage panel is a practical example, and all aircraft companies perform such calculations to estimate the fatigue life of critical components. Thus, with this example the significance of finite element analysis based stress intensity factor determination is emphasized and a life estimation approach is demonstrated.

The following items are also listed as recommendations for future works:

- For the future work, the effect of different modeling alternatives of connector elements and mesh independent fasteners on the stress intensity factors of stiffened cracked sheets can be studied thoroughly. Finite element codes have many modeling alternatives for the connector elements and the effect of using different modeling approaches of the connector elements on the stress intensity factors is a worthwhile study to perform.
- In the present study, analytical and finite element based determination of stress intensity factors for the broken stiffener case is performed for single broken stiffener case. As a future work, the study can be expanded to multiple broken stiffener case.
- The curvature and the bulging effects on the stress intensity factors for the stiffened fuselage panels may be investigated thoroughly.
- Franc 3D model can be developed for validating the 3D Abaqus model results, presented in the sample case, for determining the stress intensity factor for pressurized fuselage panel.

- In the present study, the effect of fastener pre-load is not included in the analysis. Incorporating fastener pre-load on the stress intensity factor determination of stiffened panels is considered to be an important future study to conduct. Studies can be conducted to include the effect of fastener pre-load on the stress intensity factor analytically and numerically through appropriate finite element modeling approaches, the effect of fastener pre-load on the stress intensity factor will also be investigated.
- The effect of the stiffener geometry may be investigated thoroughly, and these effects may be included in the analytical tool.

## REFERENCES

- [1] Scmidth, H. J. and Scmidth, B., “Damage Tolerant Design Seminar Notes,” *Damage Tolerant Design Seminar*, TÜBİTAK, 2008.
- [2] *Aircraft Accident Report Aloha Airlines, Flight 243 BOEING 737-200, N73711, MAUI, HAWAII*, 1988.
- [3] “Federal Aviation Regulations, Airworthiness Standards: Transport Category Airplanes,” Sec 25.571, FAA.
- [4] Swift, T., “Development of the Fail-Safe Design Features of DC-10,” Astm stp 486, American Society of Testing Materials, 1971.
- [5] Bloom, J. M. and J. L. Sanders, J., “The Effect of a Riveted Stringer on the Stress in a Cracked Sheet,” *Journal of Applied Mechanics*, Vol. 33, No. 3, 1966, pp. 561–570.
- [6] Poe, C. C., “Stress intensity factor for a cracked sheet with riveted and uniformly spaced stringer,” Nasa technical report r-358, NASA, 1971.
- [7] Poe, C. C., “The effect of broken stringers on the stress intensity factor for a uniformly stiffened sheet containing a crack,” Nasa technical memorandum x-72947, NASA, 1973.
- [8] Poe Jr, C., “Fatigue crack propagation in stiffened panels,” *Damage tolerance in aircraft structures: a symposium presented at the seventy-third annual meeting American Society for Testing and Materials, Toronto, Ontario, Canada, 21-26 June 1970*, ASTM International, 1971, p. 79.
- [9] Newman, J., *Stress analysis of simply and multiply connected regions containing cracks by the method of boundary collocation*, Ph.D. thesis, Virginia Polytechnic Institute, 1969.
- [10] Rooke, D. and Cartwright, D., “The compendium of stress intensity factors,” *International Journal of Fracture*, 1978, pp. R143–R143.
- [11] “The compounding method of estimating stress intensity factors for cracks in complex configurations using solutions from simple configurations,” Esdu 78036, ESDU, 1978.
- [12] Swift, T., “The effects of fastener flexibility and stiffener geometry on the stress intensity in stiffened cracked sheets,” *Proceedings of the Conference on Prospects of Fracture*, Noordhoff International, Leyden, Netherlands, 1974, pp. 419–457.
- [13] Tada, H., Paris, P. C., and Irwin, G. R., “The Stress Analysis of Cracks Handbook,” *Del. Research Corporation*, 1973.
- [14] Westergaard, H. M., “Bearing Pressures and Cracks,” *Journal of Applied Mechanics*, 1939.

- [15] Seshadri BR, Newman JC, D. D. and RD, Y., “Fracture analysis of the FAA/NASA wide stiffened panels,” Nasa tm-1998-208976, Langley Research Center, Hampton, VI,USA, 1998.
- [16] Widagdo, D. and Aliabadi, M. H., “Boundary element analysis of cracked panels repaired by mechanically fastened composite patches,” *Engineering Analysis with Boundary Elements*, Vol. 25, No. 4-5, 2001, pp. 339 – 345.
- [17] Mabson, G., Deobald, L., Dopker, B., Hoyt, D., Baylor, J., and Graesser, D., “Fracture Interface Elements for Static and Fatigue Analysis,” 16<sup>th</sup> *International Conference on Composite Materials*, Kyoto, JAPAN, 2007.
- [18] Tanzer, G., *Life Assessment of a Stationary Jet Engine Component With a Three-Dimensional Structural Model*, Master’s thesis, Department of Aerospace Engineering, Middle East Technical University, 2004.
- [19] Parekh C.J., Arnold R.R., W. P., “A Modern Family of Crack Tip Elements for MSC/NASTRAN,” *MSC/NASTRAN User’s Conference*, Universal City, California, USA, 1986.
- [20] Swenson, D. and James, M., *FRANC2D/L: A Crack Propagation Simulator for Plane Layered Structures*, 1997.
- [21] *Franc 2D/L and Casca: A Crack Propagation Simulator and Pre-processor program, Cornell Version*, from <http://www.cfg.cornell.edu/index.htm>.
- [22] Swenson, D. and James, M., *FRANC3D: Fracture Analysis Code for Simulating Arbitrary Non-planar 3D Crack Growth*, 1987.
- [23] *Abaqus Analysis User’s Manual*, Providence, RI,USA, 2009.
- [24] Moes, N., Dolbow, J., and Belytschko, T., “A finite element method for crack growth without re-meshing,” *International Journal for Numerical Methods in Engineering*, Vol. 46, No. 1, 1999, pp. 131–150.
- [25] Hansbo, A. and Hansbo, P., “A finite element method for the simulation of strong and weak discontinuities in solid mechanics,” *Computer methods in applied mechanics and engineering*, Vol. 193, No. 33-35, 2004, pp. 3523–3540.
- [26] Song, J., Areias, P., and Belytschko, T., “A method for dynamic crack and shear band propagation with phantom nodes,” *International Journal for Numerical Methods in Engineering*, Vol. 67, No. 6, 2006, pp. 868–893.
- [27] Giner, E., Sukumar, N., Tarancon, J., and Fuenmayor, F., “An Abaqus implementation of the extended finite element method,” *Engineering Fracture Mechanics*, Vol. 76, No. 3, 2009, pp. 347–368.
- [28] Sukumar, N., Moës, N., Moran, B., and Belytschko, T., “Extended finite element method for three-dimensional crack modelling,” *International Journal for Numerical Methods in Engineering*, Vol. 48, No. 11, 2000, pp. 1549–1570.
- [29] Pais, M., *2D Static Edge Crack Modelling with ABAQUS X-Fem Tutorial*, <http://www.matthewpais.com/2DEdgeCrack>, 21/02/2012.

- [30] Nurse, A., Güng, S., and Patterson, E., “Experimental stress intensity factors for cracks in a thin plate with stiffeners,” *The Journal of Strain Analysis for Engineering Design*, Vol. 30, No. 3, 1995, pp. 235.
- [31] Paris, P. C., “Application of Muskhelishvili’s Methods to the Analysis of Crack Tip Stress Intensity Factors for Plane Problems,” Tech. rep., Langley Research Center, 1960.
- [32] Love, A. E. H., *A Treatise on the Mathematical Theory of Elasticity*, Dover Publications, 4th ed., 1944.
- [33] DAĞ, S., “ME 583 Fracture Mechanics Notes,” lecture notes, Middle East Technical University, 2010.
- [34] *Airbus A400M Military Cargo Airplane Technical Specifications*, <http://en.wikipedia.org/>, 21/02/2012.
- [35] *Airbus A400M Military Cargo Airplane Official Website*, from <http://www.a400m.com/Specifications.aspx>, 21/02/2012.
- [36] *Altitude Air Pressure Calculator*, from <http://www.altitude.org>, 21/02/2012.
- [37] *Thin walled pressure vessel*, from <http://physicsarchives.com/index.php/courses/900>, 21/02/2012.
- [38] “Modeling Fracture and Failure with Abaqus,” Lecture notes, Dassault Systems Simulia Corporation, Providence, RI, USA, 2010.
- [39] Rahman, A., NAVAIR, N., and Branch, T., “Bulging effects on longitudinal cracks in lap joints of pressurized aircraft fuselage,” *Aging Aircraft Conference*, 2002, pp. 16–19.
- [40] *Military Standardization Handbook: Metallic Materials and Elements for Aerospace Vehicle Structures*, U.S Department of Defense, 1987.
- [41] Paris, P. and Erdoğan, F., “A critical analysis of crack propagation laws,” *Journal of Basic Engineering*, Vol. 85, No. 4, 1963, pp. 528–534.
- [42] Forman, R., Kearney, V., and Engle, R., “Numerical Analysis of Crack Propagation in Cyclic - Loaded Structures,” *Journal of Basic Engineering*, Vol. 89, No. 3, 1967, pp. 459–464.
- [43] Pearson, S., “The effect of mean stress on fatigue crack propagation in half-inch (12.7 mm) thick specimens of aluminium alloys of high and low fracture toughness,” *Engineering Fracture Mechanics*, Vol. 4, No. 1, 1972, pp. 9–24.
- [44] Walker, K., “The effect of stress ratio during crack propagation and fatigue for 2024-T3 and 7075-T6 aluminum,” *Effects of environment and complex load history on fatigue life*, *ASTM STP*, Vol. 462, 1970, pp. 1–14.
- [45] Davies, K. and Feddersen, C., “Inverse hyperbolic tangent model of fatigue crack growth,” *Journal of Aircraft*, Vol. 12, 1975, pp. 943–947.
- [46] Elber, W., “The significance of fatigue crack closure,” *ASTM STP*, Vol. 486, 1971, pp. 230–242.
- [47] Wheeler, O., “Spectrum loading and crack growth,” 1997.

- [48] Jefferson, A., "Linear elastic fracture mechanics," *Noise and vibration*, 1982, pp. 463.
- [49] Broek, D., *Elementary engineering fracture mechanics*, Kluwer Academic Pub, 1986.
- [50] Stephens, R. and Fuchs, H., *Metal fatigue in engineering*, Wiley-Interscience, 2001.
- [51] De Koning, A., "A simple crack closure model for prediction of fatigue crack growth rates under variable-amplitude loading," *ASTM STP*, Vol. 743, 1981, pp. 63–85.
- [52] Newman, J., "A crack opening stress equation for fatigue crack growth," *International Journal of Fracture*, Vol. 24, No. 4, 1984, pp. 131–135.
- [53] Forman, R., Shivakumar, V., and Newman Jr, J., "Development of the NASA/FLAGRO computer program for analysis of airframe structures," *Advanced Structural Integrity Methods for Airframe Durability and Damage Tolerance, Part 2*, Vol. 1, 1994, pp. 277–288.
- [54] Mettu, S., Shivakumar, V., Beck, J., Yeh, F., Williams, L., Forman, R., McMahon, J., and Newman, J., "NASGRO 3.0-A software for analyzing aging aircraft," *NASA CONFERENCE PUBLICATION*, NASA, 1999, pp. 792–801.
- [55] Harter, J., "AFGROW users guide and technical manual," 2008.
- [56] AFGROW, *Air Force Growth*, <http://en.wikipedia.org/wiki/AFGROW>, 21/02/2012.
- [57] *Crack plane orientation of the materials*, from <http://www.ndt-ed.org/EducationResources/CommunityCollege/Materials/Mechanical/FractureToughness.htm>, 21/02/2012.
- [58] Leng, Y., *Materials characterization: introduction to microscopic and spectroscopic methods*, Wiley, 2008.
- [59] ASTM, E., "399-90. Annual book of ASTM standards," *American Society of Testing and Materials*, 2001.
- [60] Standard, A., "E8/E8M, 2009. Standard test methods for tension testing of metallic materials. ASTM international, West Conshohocken PA; 2009. doi: 10.1520," Tech. rep., E0008-E0008M-09. [www.astm.org](http://www.astm.org).
- [61] ASTM, E., "647-08 Standard test method for measurement of fatigue crack growth rates," *Annual Book of ASTM Standards*.
- [62] *ZunZun.com Online Curve Fitting and Surface Fitting Web Site*, <http://zunzun.com/>, 21/02/2012.

## APPENDIX A

### DERIVATION OF INFLUENCE COEFFICIENTS

#### A.1 Derivation of $B_i$ Coefficient

Derivation of the influence coefficient  $B_i$ , which is the displacement at the  $i$ 'th rivet location in the cracked sheet due to the uniform loading of the infinite sheet perpendicular to the crack direction is given in this section. Figure A.1 shows the infinite size sheet under bi-axial loading.

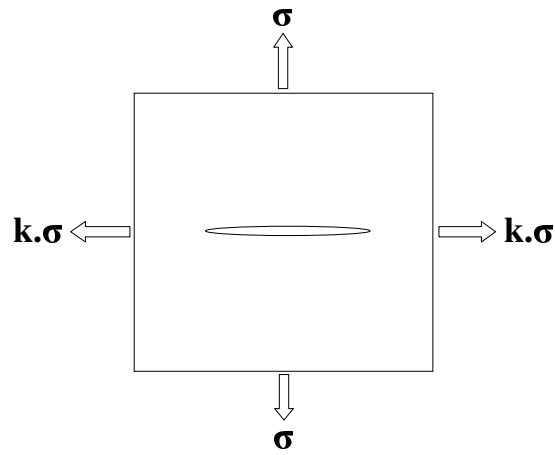


Figure A.1: Infinite size cracked sheet under bi-axial loading

According to Stanford [33], the Airy stress function for the bi-axial loading condition shown in Figure A.1 is given by Equation (A.1).

$$\Phi = \Re \bar{\bar{Z}} + y(\Im \bar{Z} + \Im \bar{Y}) \quad (\text{A.1})$$

$Z$  and  $Y$  are the Westergaard functions given by Equations (A.2a) and (A.2b), which is proposed by Stanford for bi-axial loading case [33].

$$Z = \frac{\sigma z}{\sqrt{z^2 - a^2}} \quad (\text{A.2a})$$

$$Y = -\frac{1-k}{2}\sigma \quad (\text{A.2b})$$

For uni-axial load case studied in the thesis  $k = 0$ , and  $\bar{Z}$ ,  $Z$ ,  $Z'$  and  $Z''$  are defined as Equations (A.3) to (A.6).

$$\bar{Z} = \frac{\partial \bar{Z}}{\partial z} \quad (\text{A.3})$$

$$Z = \frac{\partial \bar{Z}}{\partial z} \quad (\text{A.4})$$

$$Z' = \frac{\partial Z}{\partial z} \quad (\text{A.5})$$

$$Z'' = \frac{\partial Z'}{\partial z} \quad (\text{A.6})$$

Similar derivative expressions are valid for the  $Y$  function, with  $Z$  being substituted by  $Y$  in the above relations namely Equations (A.3) to (A.6).

In-plane stresses are defined in terms of the Airy stress function as given in Equation (A.7c).

$$\sigma_{xx} = \frac{\partial^2 \Phi}{\partial y^2} \quad (\text{A.7a})$$

$$\sigma_{yy} = \frac{\partial^2 \Phi}{\partial x^2} \quad (\text{A.7b})$$

$$\sigma_{xy} = -\frac{\partial^2 \Phi}{\partial x \partial y} \quad (\text{A.7c})$$

Now, the in-plane stresses are expressed in terms of Westergaard functions.

$$\frac{\partial\Phi}{\partial y} = \Im\bar{Y} + y(\Re Z + \Re Y) \quad (\text{A.8a})$$

$$\sigma_{xx} = \frac{\partial^2\Phi}{\partial y^2} = 2\Re Y + \Re Z - y(\Im Z' + \Im Y') \quad (\text{A.8b})$$

$$\frac{\partial\Phi}{\partial x} = \Re Z + y(\Im Z + \Im Y) \quad (\text{A.9a})$$

$$\sigma_{yy} = \frac{\partial^2\Phi}{\partial x^2} = \Re Z + y(\Im Z' + \Im Y') \quad (\text{A.9b})$$

$$\sigma_{xy} = -y(\Re Z' + \Re Y') - \Im Y \quad (\text{A.10})$$

Displacements are then determined by making use of the constitutive equations, given as Equation (A.11).

$$\varepsilon_{xx} = \frac{\partial u}{\partial x} = \frac{1}{8\mu} \{(\kappa + 1)\sigma_{xx} - (3 - \kappa)\sigma_{yy}\} \quad (\text{A.11a})$$

$$\varepsilon_{yy} = \frac{\partial v}{\partial y} = \frac{1}{8\mu} \{(\kappa + 1)\sigma_{yy} - (3 - \kappa)\sigma_{xx}\} \quad (\text{A.11b})$$

$$\varepsilon_{xy} = \frac{1}{2\mu}\sigma_{xy} \quad (\text{A.11c})$$

Since the influence coefficients are defined for the  $y$  direction displacement, which is denoted by  $v$ , Equation (A.11b) must be integrated with respect to  $y$ . To integrate Equation (A.11b), normal stresses in the  $x$  and  $y$  direction must be integrated with respect to  $y$ . The integral of the normal stresses in the  $x$  and  $y$  direction is given by Equation (A.12).

$$\int \sigma_{yy} \cdot dy = 2\Im\bar{Z} + \Im\bar{Y} - y(\Re Z + \Re Y) \quad (\text{A.12a})$$

$$\int \sigma_{xx} \cdot dy = \Im\bar{Y} + y(\Re Z + \Re Y) \quad (\text{A.12b})$$

Inserting Equation (A.12) into Equation (A.11b), Equation (A.13) is obtained.

$$\nu = \frac{1}{8\mu} \left\{ (\kappa + 1) [2\Im\bar{Z} + \Im\bar{Y} - y(\Re Z + \Re Y)] - (3 - \kappa) [\Im\bar{Y} + y(\Re Z + \Re Y)] \right\} \quad (\text{A.13})$$

where,

$$\mu = \frac{E}{2(1 + \nu)} \quad \text{and} \quad \kappa = \frac{3 - \nu}{1 + \nu} \quad (\text{A.14})$$

$$Z = \frac{\sigma z}{\sqrt{z^2 - a^2}} \quad (\text{A.15a})$$

$$\bar{Z} = \sigma \sqrt{z^2 - a^2} \quad (\text{A.15b})$$

$$Y = -\frac{1 - k}{2} \sigma \quad (\text{A.15c})$$

$$\bar{Y} = -\frac{z}{2} \sigma \quad \text{for} \quad k = 0 \quad (\text{A.15d})$$

It should be noted that the coordinates of a point  $z$  in the cracked zone, as shown in Figure A.2, can be written in polar coordinates as in Equation (A.16).

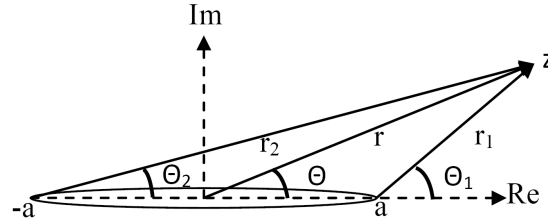


Figure A.2: Crack tip zone

$$z = a + r_1 e^{j\theta_1} \quad \text{or} \quad z - a = r_1 e^{j\theta_1} \quad (\text{A.16a})$$

$$z = -a + r_2 e^{j\theta_2} \quad \text{or} \quad z + a = r_2 e^{j\theta_2} \quad (\text{A.16b})$$

$$z = r e^{j\theta} \quad (\text{A.16c})$$

Substituting Equation (A.15) in Equation (A.13) and using Equation (A.16) in Equation (A.15), displacement  $v$  given by Equation (A.17) is derived.

$$v = \frac{\sigma}{E} \left\{ 2\sqrt{r_1 r_2} \sin \frac{\theta_1 + \theta_2}{2} - y - \frac{y(1 + \nu)}{\sqrt{r_1 r_2}} \left[ x \cos \frac{\theta_1 + \theta_2}{2} + y \sin \frac{\theta_1 + \theta_2}{2} - \sqrt{r_1 r_2} \right] \right\} \quad (\text{A.17})$$

Influence coefficient  $B_i$  is determined from Equation (A.17) by substituting  $\sigma = 1$ .

## A.2 Derivation of $A_{ij}^s$ Coefficient

Using the equations of the configuration for four point forces as shown in Figure A.3, as mentioned in Page 19, and manipulating it for the finite width single stiffener, one can get the influence coefficient  $A_{ij}^s$ , which gives the displacement at the  $i$ 'th rivet location due to a unit force at the  $j$ 'th rivet location. Figure A.4 shows the approximation of a finite width riveted stiffener by the infinite size riveted sheet. It should be noted that in this approximation, the only boundary condition for the finite width stiffener that is not satisfied is  $\sigma_{xx} = 0$  at  $x = \mp w/2$ . In order to carry out the calculation, the effect of the rivet forces, shown in Figure A.3, must be superimposed. However, in this case the contribution of the rivet forces in the central stiffener must also be added to get the displacement equation for the single stiffener.

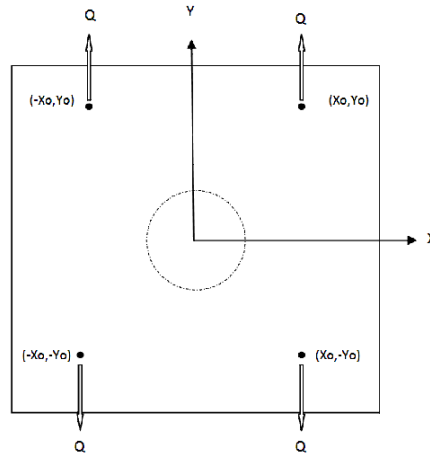


Figure A.3: Symmetrical four point forces acting on four quadrant

The  $y$  displacement due to four rivet forces in an infinite size sheet, shown in Figure A.3 and given by Equation (A.18), was derived in Chapter 2 as (Equation (2.14)).

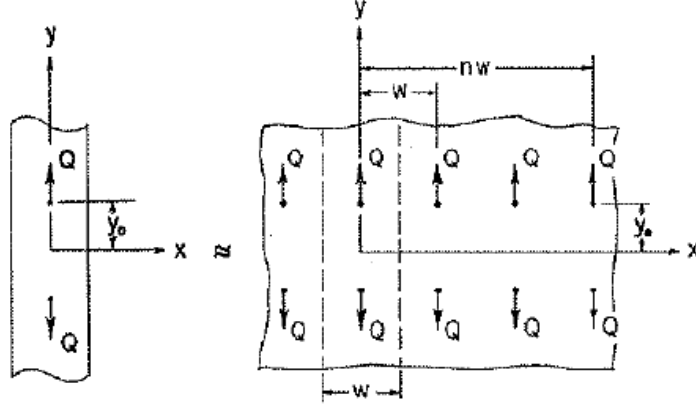


Figure A.4: Approximation of the finite width riveted stiffener by the infinite size riveted sheet [6]

$$v_a = \frac{(1 + \nu)(3 - \nu)Q}{16\pi tE} \Omega \quad (\text{A.18})$$

where  $\Omega$  is given by

$$\begin{aligned} \Omega = & (\alpha_1 + 1) \ln \left[ \frac{(\alpha_1 + 1)^2 + \alpha_4^2}{(\alpha_1 + 1)^2 + \alpha_3^2} \right] - (\alpha_1 - 1) \ln \left[ \frac{(\alpha_1 - 1)^2 + \alpha_4^2}{(\alpha_1 - 1)^2 + \alpha_3^2} \right] \\ & + (\alpha_2 + 1) \ln \left[ \frac{(\alpha_2 + 1)^2 + \alpha_4^2}{(\alpha_2 + 1)^2 + \alpha_3^2} \right] - (\alpha_2 - 1) \ln \left[ \frac{(\alpha_2 - 1)^2 + \alpha_4^2}{(\alpha_2 - 1)^2 + \alpha_3^2} \right] \\ & + 4 \left( \frac{1 - \nu}{3 - \nu} \right) \left\{ \alpha_4 \left[ \arctan \left( \frac{2\alpha_4}{\alpha_1^2 + \alpha_4^2 - 1} \right) + \arctan \left( \frac{2\alpha_4}{\alpha_2^2 + \alpha_4^2 - 1} \right) \right] \right. \\ & \left. - \alpha_3 \left[ \arctan \left( \frac{2\alpha_3}{\alpha_1^2 + \alpha_3^2 - 1} \right) + \arctan \left( \frac{2\alpha_3}{\alpha_2^2 + \alpha_3^2 - 1} \right) \right] \right\} \quad (\text{A.19}) \end{aligned}$$

### A.2.1 Derivation of $\Psi_0$

To derive the displacement at the  $i$ th rivet location in a riveted stiffener, shown in Figure A.4, because we are interested in the displacement of the stiffener which is at the origin of the coordinate system,  $x$  values should be set to zero while superimposing the effects of the rivet forces of the infinite size sheet shown in Figure A.3. Thus, in the series summation given by

Equation (2.28)  $n = 0$ ,  $x = 0$ ,  $x_0 = 0$  and  $y$  and  $y_0$  are distinct  $y$  coordinates indicating the locations where displacement is desired and where rivet force is applied, respectively.

Therefore  $\alpha$  coefficients, defined in Chapter 2, become

$$\begin{aligned}\alpha_1 &= \frac{2(x - x_0)}{d} & \alpha_1 &= 0 \\ \alpha_2 &= \frac{2(x + x_0)}{d} & \alpha_2 &= 0 \\ \alpha_3 &= \frac{2(y - y_0)}{d} & \alpha_3 &= \alpha_3 \\ \alpha_4 &= \frac{2(y + y_0)}{d} & \alpha_4 &= \alpha_4\end{aligned}$$

Substituting the expression for  $\alpha_i$  to Equation (A.19), for  $n = 0$ ,  $\Omega_0$  becomes,

$$\Omega_0 = 4 \ln \left( \frac{1 + \alpha_4^2}{1 + \alpha_3^2} \right) + 8 \left( \frac{1 - \nu}{3 - \nu} \right) \left[ \alpha_4 \arctan \left( \frac{2\alpha_4}{\alpha_4^2 - 1} \right) - \alpha_3 \arctan \left( \frac{2\alpha_3}{\alpha_3^2 - 1} \right) \right] \quad (\text{A.20})$$

Note that  $\Psi_0 = \Omega_0/4$ , therefore;

$$\Psi_0 = \ln \left( \frac{1 + \alpha_4^2}{1 + \alpha_3^2} \right) + 2 \left( \frac{1 - \nu}{3 - \nu} \right) \left[ \alpha_4 \arctan \left( \frac{2\alpha_4}{\alpha_4^2 - 1} \right) - \alpha_3 \arctan \left( \frac{2\alpha_3}{\alpha_3^2 - 1} \right) \right] \quad (\text{A.21})$$

### A.2.2 Derivation of $\Psi_n$

For  $\Omega_n$ ,  $x_0 = nw$  and  $x = 0$  therefore the  $\alpha$  coefficients become;

$$\begin{aligned}\alpha_1 &= -\frac{2nw}{d} \\ \alpha_2 &= \frac{2nw}{d} \\ \alpha_3 &= \alpha_3 \\ \alpha_4 &= \alpha_4\end{aligned}$$

Substituting  $\alpha_1$  to  $\alpha_4$  into Equation (A.18), and after manipulating the resulting expressions one gets,

$$\begin{aligned} \Psi_n = & \left(1 - \frac{2nw}{d}\right) \ln \left[ \frac{\left(1 - \frac{2nw}{d}\right)^2 + \alpha_4^2}{\left(1 - \frac{2nw}{d}\right)^2 + \alpha_3^2} \right] + \left(1 + \frac{2nw}{d}\right) \ln \left[ \frac{\left(1 + \frac{2nw}{d}\right)^2 + \alpha_4^2}{\left(1 + \frac{2nw}{d}\right)^2 + \alpha_3^2} \right] \\ & + 4 \left( \frac{1-\nu}{3-\nu} \right) \left\{ \alpha_4 \arctan \frac{2\alpha_4}{\left(\frac{2nw}{d}\right)^2 + \alpha_4^2 - 1} - \alpha_3 \arctan \frac{2\alpha_3}{\left(\frac{2nw}{d}\right)^2 + \alpha_3^2 - 1} \right\} \end{aligned} \quad (\text{A.22})$$

It should be noted that  $\Psi_n = \Omega_n/2$ .

### A.3 Derivation of $A_{ij}$ Coefficient

#### A.3.1 Derivation of Equation (2.9)

Derivation of Equation (2.9) starts from Equation (A.23) which is taken from [32]. Equation (A.23) gives the displacement of an infinite size sheet which is subjected to a concentrated force at the origin. Equation (A.23) is the displacement due to the concentrated force of magnitude  $2\pi At$  applied in the -x direction.

$$u = \frac{\lambda' + 3\mu}{2\mu(\lambda' + 2\mu)} A \frac{\ln(x^2 + y^2)}{2} + \frac{\lambda' + \mu}{2\mu(\lambda' + 2\mu)} A \frac{y^2}{x^2 + y^2} \quad (\text{A.23})$$

For plane stress,  $\lambda'$ ,  $\mu$  and  $\lambda$  are given by

$$\lambda' = \frac{2\lambda\mu}{\lambda + 2\mu} \quad \mu = \frac{E}{2(1+\nu)} \quad \lambda = \frac{E\nu}{(1+\nu)(1-2\nu)} \quad (\text{A.24})$$

Substituting Equation (A.24) to the Equation (A.23), Equation (A.25) can be obtained.

$$u = \frac{A(1+\nu)}{2E} \left\{ \frac{3-\nu}{2} \ln(x^2 + y^2) + (\nu+1) \frac{y^2}{x^2 + y^2} \right\} \quad (\text{A.25})$$

where for a plate of unit thickness, the concentrated force applied is given by  $Q = -2A\pi$ . Therefore, in Equation (A.25)  $A$  can be taken as  $\frac{Q}{-2\pi}$ .

After performing the necessary simplifications, and substituting  $A$  into Equation (A.25), Equation (A.26) is derived.

$$v = -\frac{(1+\nu)Q}{4\pi t E} \left[ \frac{1}{2}(3-\nu) \ln(x^2 + y^2) + (1+\nu) \left( \frac{x^2}{x^2 + y^2} \right) \right] \quad (\text{A.26})$$

It should be noted that the derivation of the  $v$  displacement is done by using the formula for the  $u$  displacement. This is because, in the work of Love [32], concentrated force is applied in  $x$  direction. In the present study, the point load is applied in  $y$  direction, therefore variables are changed accordingly.

### A.3.2 Derivation of Equation (2.10)

Derivation of Equation (2.10) starts from Equation (A.27) which is taken from Love [32]. Equation (A.27) gives the  $x$  direction stress in an infinite size sheet which is subjected to a concentrated force at the origin. Equation (A.27) is the stress due to the concentrated force of magnitude  $2\pi At$  applied in the  $-x$  direction.

$$\sigma_x = A \frac{x}{x^2 + y^2} \left\{ \frac{2\lambda' + 3\mu}{\lambda' + 2\mu} - \frac{2(\lambda' + \mu)}{\lambda' + 2\mu} \frac{y^2}{x^2 + y^2} \right\} \quad (\text{A.27})$$

Substituting Equation (A.24) into Equation (A.27), Equation (A.28) is obtained. Equation (A.28) gives the stress in the  $x$  direction due to a concentrated force acting at the origin in the  $-x$  direction in an infinite size plate. However, in the present study, the concentrated force acts in the  $+y$  direction. Therefore, variables must be changed to obtain the expression for the  $y$  direction stress  $\sigma_{yy}$ .

$$\sigma_x = A \frac{x}{x^2 + y^2} \frac{\nu + 1}{2} \left[ \frac{\nu + 3}{\nu + 1} - \frac{2y^2}{x^2 + y^2} \right] \quad (\text{A.28})$$

After replacing  $x$  with  $y$ , and substituting  $A = -\frac{Q}{2\pi}$  in Equation (A.28), Equation (A.29), which gives the  $y$  direction stress  $\sigma_{yy}$  is derived.

$$\sigma_{yy} = -\frac{(1+\nu)Q}{4\pi t} \left( \frac{y}{x^2 + y^2} \right) \left( \frac{3+\nu}{1+\nu} - \frac{2x^2}{x^2 + y^2} \right) \quad (\text{A.29})$$

### A.3.3 Derivation of Equation (2.14)

Equation (2.14) gives the displacement in part a of Figure 2.4. In the derivation process of Equation (2.14), in order to get rid of the singularity at the origin,  $x$  should be replaced by  $x - \bar{x}$  as shown in Figure A.5, and Equation (A.26) should be integrated from  $-\frac{1}{2}d$  to  $\frac{1}{2}d$ .

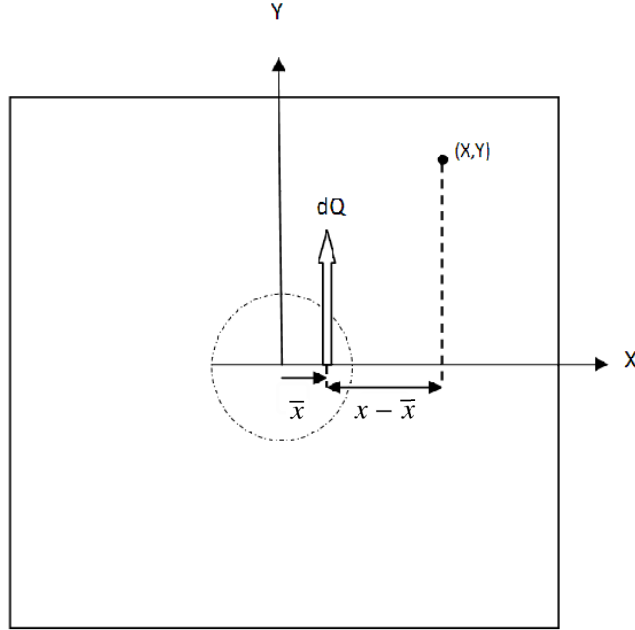


Figure A.5: Distributing the point force to the diameter

Changing the variables as shown in Equation (A.30), the  $y$  direction displacement  $v$  for part a of Figure 2.4 is obtained. Equation (A.31) gives the integral expression, when evaluated, gives the displacement  $v$  for part a of Creff:aijcoefficient.

$$z = x - \bar{x} \qquad dz = -d\bar{x} \qquad (A.30)$$

$$v = -\frac{(1 + \nu)Q}{4\pi t E d} \int_{z=x+d/2}^{z=x-d/2} \left[ \frac{1}{2}(3 - \nu) \ln(z^2 + y^2) + (1 + \nu) \left( \frac{z^2}{z^2 + y^2} \right) \right] dz \qquad (A.31)$$

Integrating Equation (A.31), and doing the necessary simplifications Equation (A.33) is obtained.

$$v = \frac{(1+\nu)Q}{4\pi t E d} \left[ \left( -2z + 2y \arctan \frac{z}{y} + z \ln(z^2 + y^2) \right) \frac{3-\nu}{2} + (1+\nu) \left( z - y \arctan \frac{z}{y} \right) \right]_{x+d/2}^{x-d/2} \quad (\text{A.32})$$

$$v = -\frac{(1+\nu)(3-\nu)Q}{16\pi t E} \left\{ \left( \frac{2x}{d} + 1 \right) \ln \left[ \left( \frac{2x}{d} + 1 \right)^2 + \frac{4y^2}{d^2} \right] - \left( \frac{2x}{d} - 1 \right) \ln \left[ \left( \frac{2x}{d} - 1 \right)^2 + \frac{4y^2}{d^2} \right] + \frac{8(1-\nu)y}{d(3-\nu)} \arctan \left[ \frac{\frac{y}{d}}{\frac{x^2}{d^2} + \frac{y^2}{d^2} - \frac{1}{4}} \right] \right\} + \underbrace{\frac{(1+\nu)(3-\nu)Q}{16\pi t E} \left[ \frac{8(1-\nu)}{d(3-\nu)} + \frac{8 \ln^2(2/d)}{d(3-\nu)} \right]}_{\text{Constant}} \quad (\text{A.33})$$

It should be noted that in the article of Poe [6], the constant term in Equation (A.33) is not shown. For the single concentrated load, the constant term has to exist in Equation (A.33). However, in the derivation of the influence coefficient  $A_{ij}$ , the  $y$  direction displacement is obtained for four concentrated forces which act on four quadrants, shown in part a of Figure 2.4, and in symmetric locations with respect to the  $x$  and  $y$  axes. To calculate influence coefficient  $A_{ij}$ , displacements due to four concentrated forces acting on four quadrants are superimposed. During the summation of the displacements due to forces acting in four quadrants, the constant terms cancel out each other. Therefore, the constant term in Equation (A.33) is not shown by Poe [6].

#### A.3.4 Derivation of Equation (2.17)

Equation (A.29) gives the  $y$  direction stress for the configuration of a concentrated force acting at the origin. In order to derive Equation (2.17), which gives the  $y$  direction stress for part B of Figure 2.4, firstly the point forces should be translated to the  $(\mp x_0, \mp y_0)$  and stresses should be added up. By re-arranging Equation (A.29), Equation (A.34) is obtained.

$$\sigma_{yy} = -\frac{(1+\nu)Q}{2\pi t d} \left\{ \frac{3+\nu}{1+\nu} \frac{\frac{2y}{d}}{\left(\frac{2x}{d}\right)^2 + \left(\frac{2y}{d}\right)^2} - 2 \left( \frac{2y}{d} \right) \left( \frac{\left(\frac{2x}{d}\right)^2}{\left(\frac{2x}{d}\right)^2 + \left(\frac{2y}{d}\right)^2} \right) \right\} \quad (\text{A.34})$$

For translating the point forces to get the four point force configuration of part a of Figure 2.4  $x$  and  $y$  should be replaced by  $x - x_0$  and  $y - y_0$ ,  $x + x_0$  and  $y - y_0$ ,  $x - x_0$  and  $y + y_0$ ,  $x + x_0$  and

$y + y_0$  in sequence, and the resulting stress expressions must be added up. Superimposing the stress expressions due to four concentrated forces acting at four quadrants and re-arranging the terms, Equation (A.35) is obtained.

$$\sigma_{yy} = \frac{(1+\nu)Q}{2\pi t d} \left\{ \frac{3+\nu}{1+\nu} \left( \frac{\alpha_4}{(\alpha_1)^2 + (\alpha_4)^2} + \frac{\alpha_4}{(\alpha_2)^2 + (\alpha_4)^2} - \frac{\alpha_3}{(\alpha_1)^2 + (\alpha_3)^2} - \frac{\alpha_3}{(\alpha_2)^2 + (\alpha_3)^2} \right) + 2\alpha_3 \left[ \left( \frac{\alpha_1}{(\alpha_1)^2 + (\alpha_3)^2} \right)^2 + \left( \frac{\alpha_2}{(\alpha_2)^2 + (\alpha_3)^2} \right)^2 \right] - 2\alpha_4 \left[ \left( \frac{\alpha_2}{(\alpha_2)^2 + (\alpha_4)^2} \right)^2 + \left( \frac{\alpha_1}{(\alpha_1)^2 + (\alpha_4)^2} \right)^2 \right] \right\} \quad (\text{A.35})$$

Equation (A.35) is the full-field equation for the  $y$  direction stress which applies for part A of Figure 2.4 To determine the  $y$  direction stress corresponding to part B of Figure 2.4, stress  $\sigma_{yy}$  acting at  $y = 0$  along the crack line must be determined. Therefore, by setting  $y = 0$  and  $x = \xi$  in Equation (A.35), Equation (A.36) is derived.

$$\sigma_{yy}(\xi, 0) = \frac{(1+\nu)Q}{2\pi t} \left\{ \left( \frac{1-\nu}{1+\nu} + 2 \right) \left[ \frac{y_0}{(\xi - x_0)^2 + y_0^2} + \frac{y_0}{(\xi + x_0)^2 + y_0^2} \right] - 2y_0 \left[ \frac{(\xi - x_0)^2}{((\xi - x_0)^2 + y_0^2)^2} + \frac{(\xi + x_0)^2}{((\xi + x_0)^2 + y_0^2)^2} \right] \right\} \quad (\text{A.36})$$

Finally, re-arranging Equation (A.36), Equation (A.37) is obtained. In Equation (A.37), the corrected exponent 2 is also shown here. This is one of the typographical errors in the report of Poe [6]. With such an error, it is impossible to replicate the stress intensity graphs presented in the technical report of Poe, and it is also impossible to obtain the correct stress intensity values, for any combination of geometrical and material properties of stiffened cracked sheets, which are not available in report by Poe [6].

$$\sigma_{yy}(\xi, 0) = \frac{(1+\nu)Qy_0}{2\pi t} \left\{ \frac{1-\nu}{1+\nu} \left( \frac{1}{(\xi - x_0)^2 + y_0^2} + \frac{1}{(\xi + x_0)^2 + y_0^2} \right) + \underbrace{2y_0^2}_{\text{Corrected Exp.}} \left[ \left( \frac{1}{(\xi - x_0)^2 + y_0^2} \right)^2 + \left( \frac{1}{(\xi + x_0)^2 + y_0^2} \right)^2 \right] \right\} \quad (\text{A.37})$$

## APPENDIX B

### TESTING OF MATERIAL PROPERTIES

#### B.1 Micro-structure Analysis

Micro-structure analysis should be done to determine the orientation of the grains before preparing the specimens which are used to determine the yield stress, fracture toughness and  $da/dN$  vs  $\Delta K$  curve. The mechanical properties of the aluminum sheet changes with the direction, because during the production process the raw aluminum blocks are deformed to form the sheets, therefore the shape of the grains and their orientations are changing according to this deformation process. The crack moves in different directions with a different speed and the fracture toughness also changes with the crack direction. Therefore, there is a need to specify the grain directions, or the rolling direction before the preparation of the specimens.

In the literature, the rolling direction is denoted by  $L$  in which the grains lie longitudinally,  $S$  is the short transverse in the thickness direction of the plate, and  $T$  is the long transverse which is the third direction which is perpendicular to  $L$  and  $T$  directions, as illustrated in Figure B.1. Figure B.2 shows the convention of the directions of the crack planes. The first letter designates the normal of the fracture plane, and the second letter designates the growing direction of the crack. Therefore, six principal fracture plane directions exist which are  $L-T$ ,  $L-S$ ,  $T-L$ ,  $T-S$ ,  $S-L$ , and  $S-T$  [57].

During the preparation of the fracture specimens, small cuts are taken from the Al-2124-T851 block. After sealing the small specimens which improves the ability to grab the specimen, grinding operation is done to obtain a shiny surface. In order to see the grain boundaries, the specimens are etched with Keller's reagent which is a special solution for etching aluminum and aluminum alloys [58].

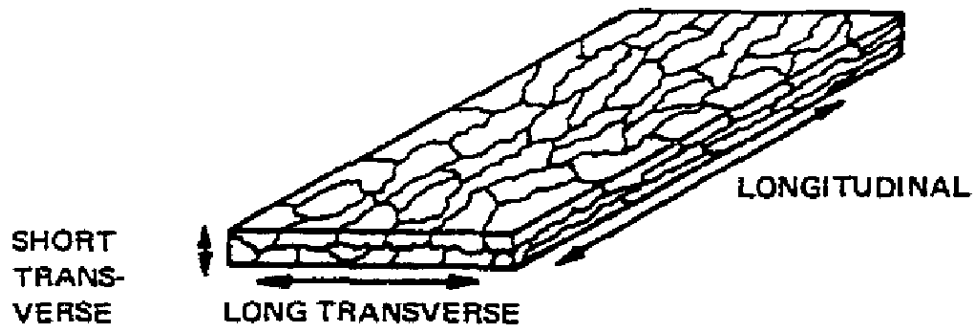


Figure B.1: Rolling direction and the grain directions

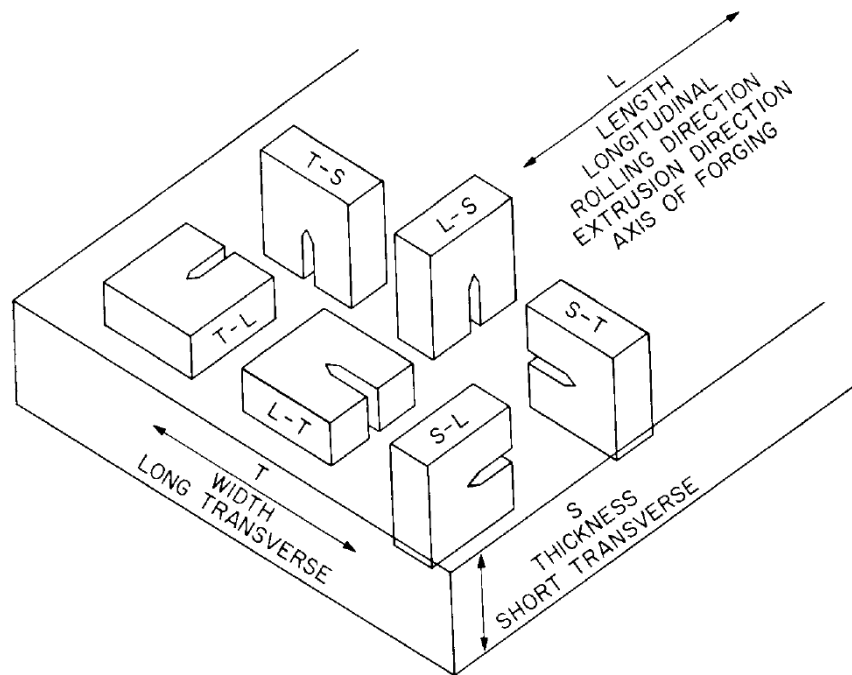


Figure B.2: Conventions for the crack planes for plates [59]

Figure B.3 shows the grain boundaries and the rolling direction of the fracture specimens. Because the specimens are taken from a thick block, the grain boundaries are not very thin, but still they are elongated and oriented in the L direction. In order to be in the conservative side, the test specimens are prepared in T-L direction, because it is the weakest crack propagation direction of the aluminum sheet. Hence, the worst data is collected for the crack propagation analysis of Al-2124-T851.

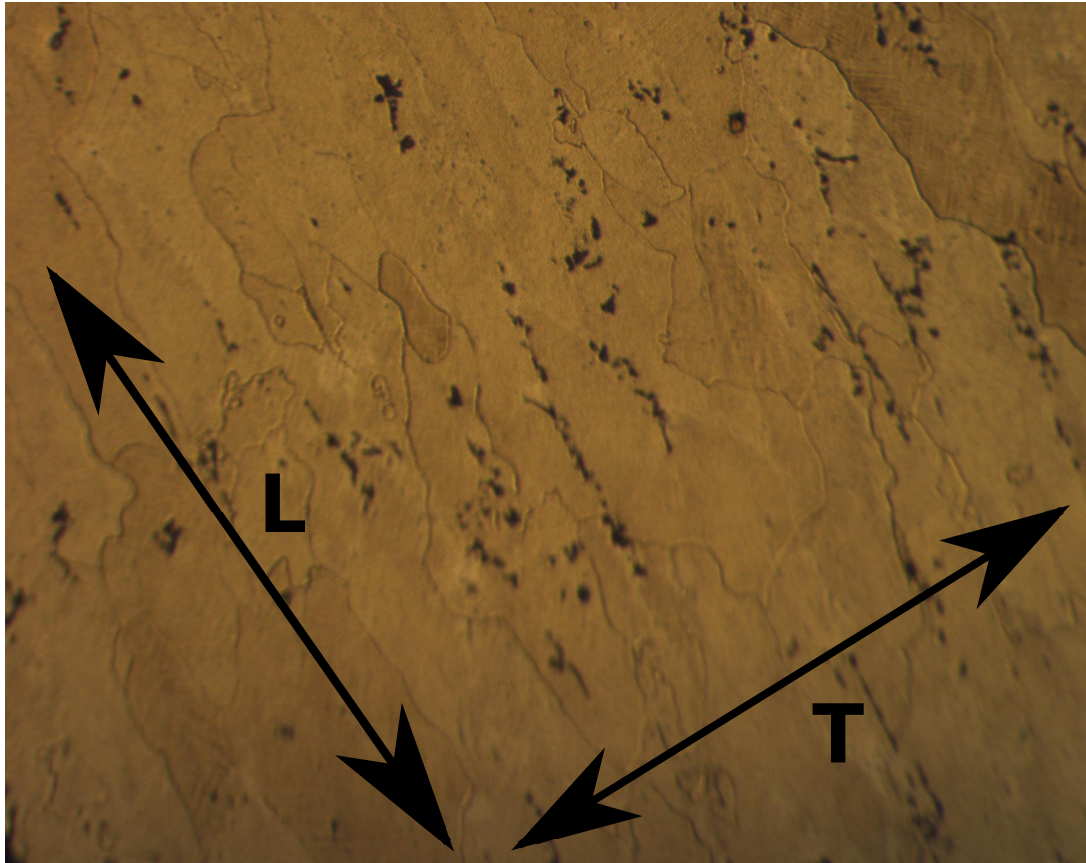


Figure B.3: Specimen inspection under the light microscope for the determination of the rolling direction

## B.2 TENSION TEST

The tension test is done for obtaining the Elastic Modulus  $E$ , and the 0.2 % Offset yield stress  $\sigma_{ys}$  which are needed in life calculations and the validation calculations of the fracture toughness test and the crack growth rate test respectively included in Appendices B.3 and B.4. Instron Tensile Test Equipment which has built-in optical extensometer, available in the Metallurgical and Materials Engineering is utilized for the tension test. Figure B.4 shows the stress strain data obtained from the tension test which is conducted according to the ASTM E8/E8M-09 [60].

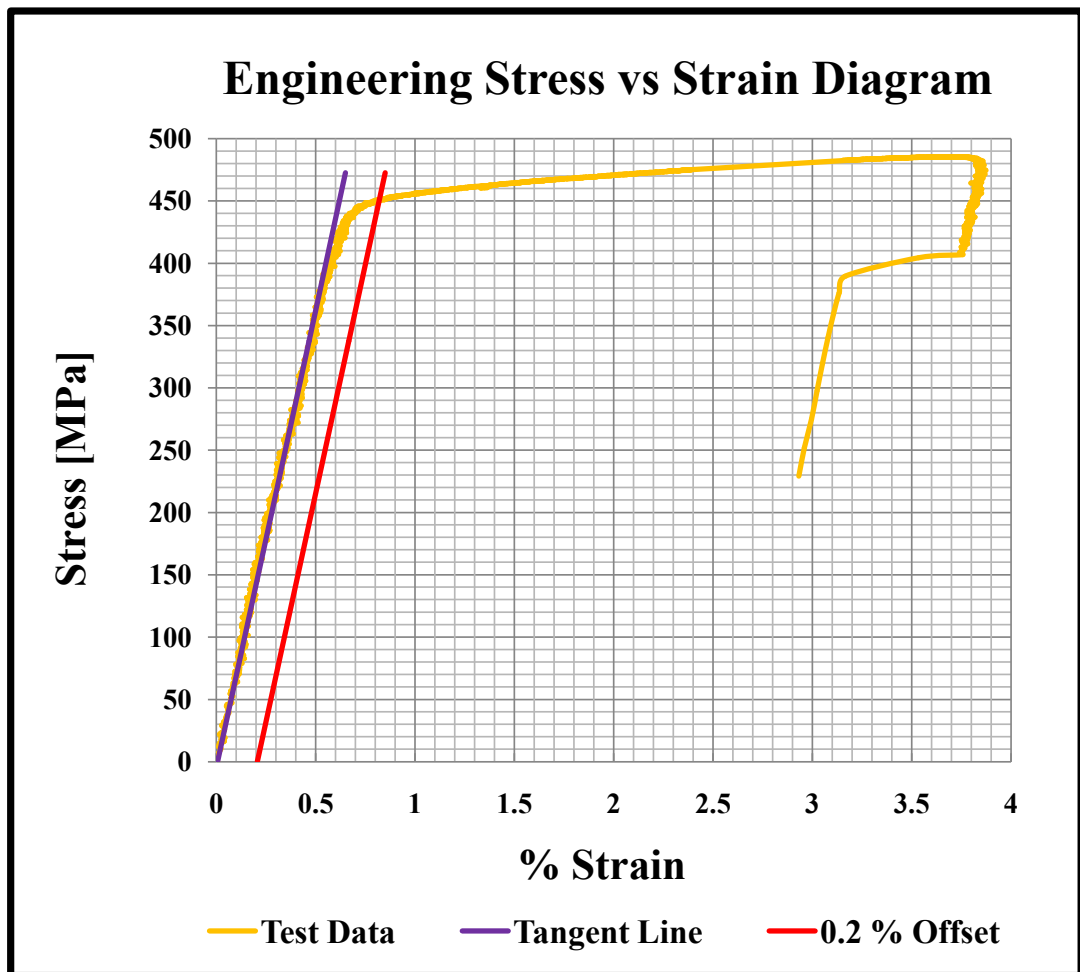


Figure B.4: Stress vs Strain data for Aluminum 2124 T-851

The purple line in the Figure B.4 represents the tangent line to the linear region of the test data, and the orange line is the 0.2 % Offset given to the purple line. The intersection of the test data and the 0.2 % Offset line gives the 0.2 % yield stress of the Aluminum 2124-

T851. Elastic Modulus is simply the slope of the tangent line to the stress strain curve given in Figure B.4. The material properties obtained from the tension test is included in Table B.1. The results are quite reasonable.

Table B.1: Tension Test Results

Tensile extension at Break [ <i>mm</i> ]	0.98155
Tensile strain at Break [ <i>mm/mm</i> ]	0.03534
Young's Modulus [ <i>MPa</i> ]	68259.86328
Tensile stress at Tensile Strength [ <i>MPa</i> ]	485.55713
Tensile strain at Tensile Strength	3.67012
Tensile extension at Tensile Strength [ <i>mm</i> ]	1.01922
Tensile stress at Yield (Offset 0.2 %) [ <i>MPa</i> ]	450.96612

### B.3 FRACTURE TOUGHNESS TEST

Figure B.5 shows the experimental set-up which is used in both fracture toughness and crack propagation testing. MTS Universal Testing Machine available in the Metallurgical and Materials Engineering Mechanical Testing Laboratory, METU is utilized for the experiments. During the experiment the crack lengths are measured visually by means of the traveler microscope, as shown in Figure B.5b. A light bulb is used for illumination of the specimen.

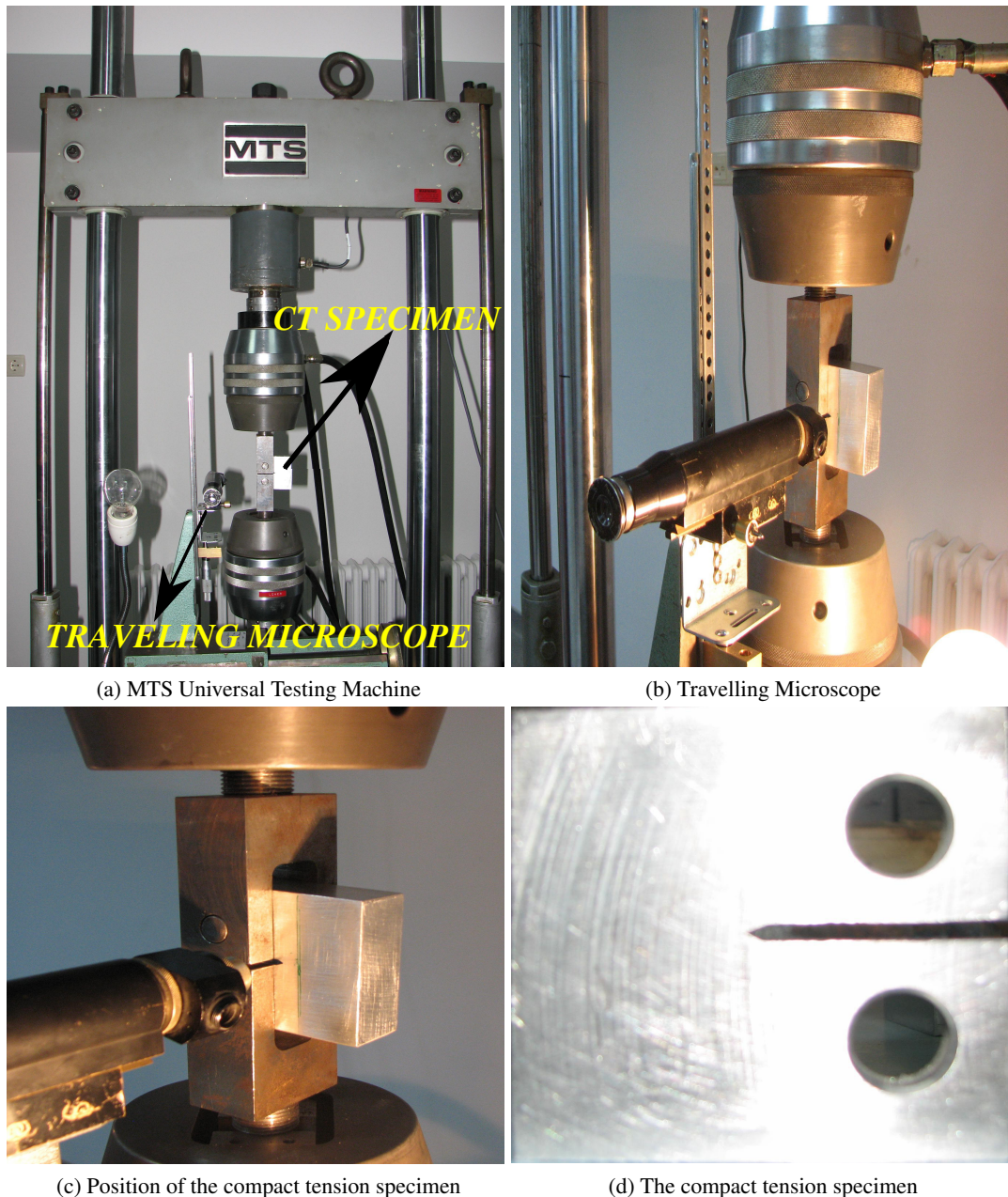


Figure B.5: Experiment Equipment

Compact tension(CT) specimen is preferred for both fracture toughness and crack propagation tests, due to the available fixtures in the mechanical test laboratory. Moreover, the Compact tension(CT) type specimens provides a longer distance which the crack can propagate. Dimensions of the CT specimen, which is used in the experiments for determination of fracture toughness is given in Figure B.6. The fracture toughness and crack propagation specimens are the same in all dimensions except for the thicknesses. The thicknesses of crack propagation specimens are chosen to be the half of the fracture toughness specimens, therefore for the fracture toughness testing 25.4mm thickness is used but for the crack propagation tests 12.7mm thickness is chosen.

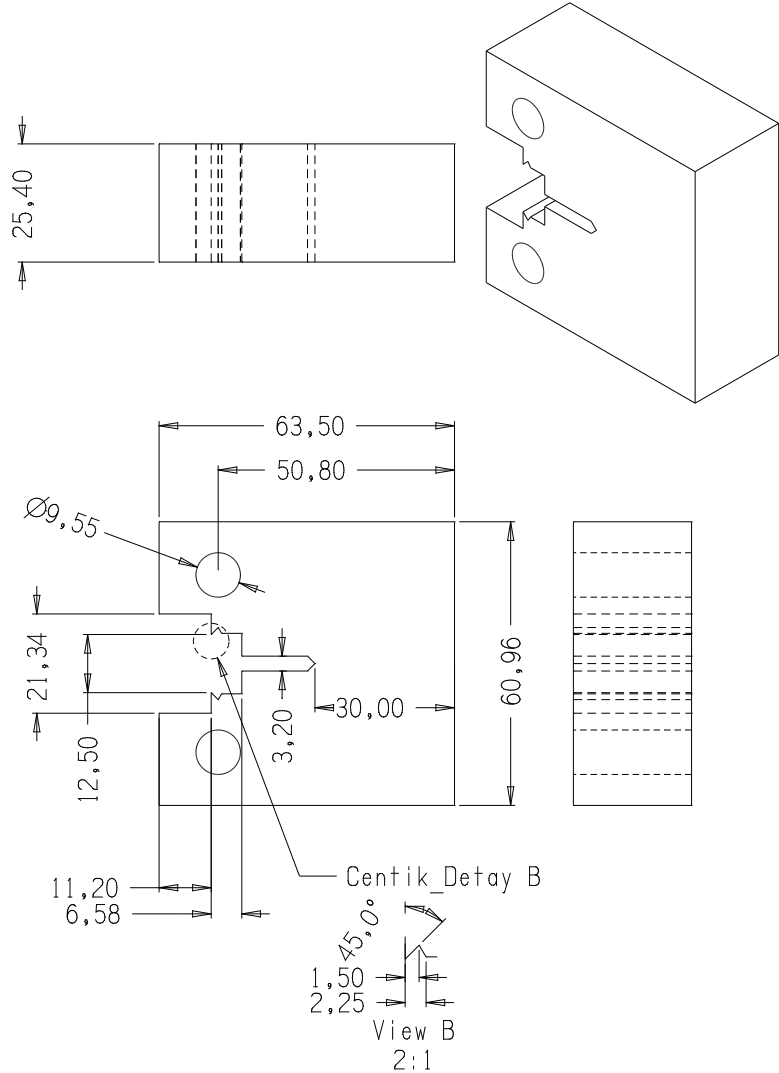


Figure B.6: CT test specimen geometry used in the experiment for crack propagation

The technical drawings of the specimens as presented in Figure B.6 is prepared in accordance with the ASTM-E399 [59] standard, and the specimens are produced in the Metallurgy and

Materials Engineering workshop. The geometry given in the standard is parametric as shown on Figure B.7 which gives the chance to adjust the dimensions compatible with the fixtures. The positions and the diameters of the holes on the specimens are critical, therefore the specimens are drilled in the Mechanical Engineering Workshop with CNC machine with very close tolerances. The fixtures on the MTS testing machine are tried to be aligned perfectly in line, because any misalignment can cause the fatigue crack to propagate faster in one face that ruins the symmetry. Instead of installing the displacement gauge the displacement are measured by the MTS system, therefore there is no need of producing *Centik Delay* part shown on Figure B.7. As recommended in the standard, a saw-cut notch is preferred [59].

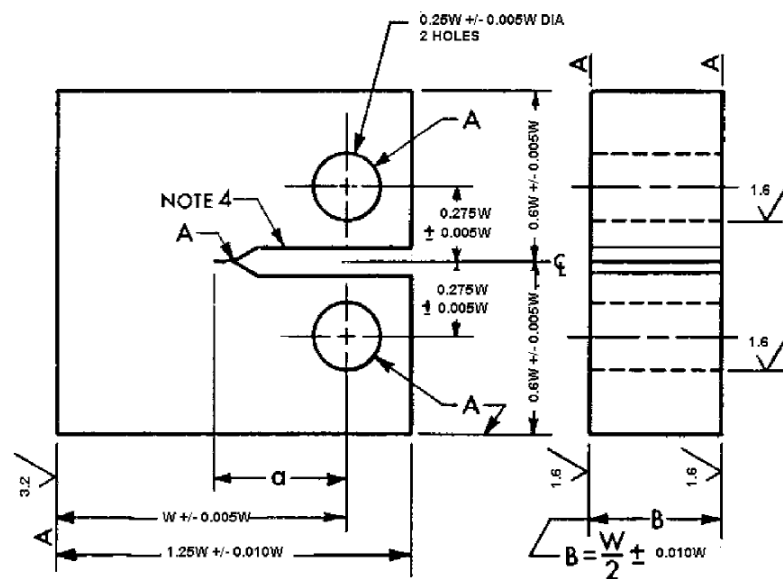


Figure B.7: CT test specimen geometry for crack propagation given in ASTM-E399 [59].

Details of the crack tips are presented in Figure B.8. The Chevron type notch is preferred due to the easiness of pre-cracking and the convenience of the production in a way that the staff in workshop is familiar with the Chevron.

According to the ASTM-E399 standard[59], the initial crack including the pre-crack has to be formed with a length in a range of  $0.45W < a_{notch} + a_{pre-crack} < 0.55W$ . Therefore, given a sinusoidal cyclic loading, fatigue crack is initiated on the notch, and the crack is propagated up to reaching the terminal value of the pre-crack recommended as the  $0.0125W$  in the ASTM-E399 standard [59]. At the end of the pre-cracking the specimen was loaded up to the fracture with a constant load rate of respectively  $1KN/sec$  and  $0.5KN/sec$  which are in the range that standard [59] is proposing.

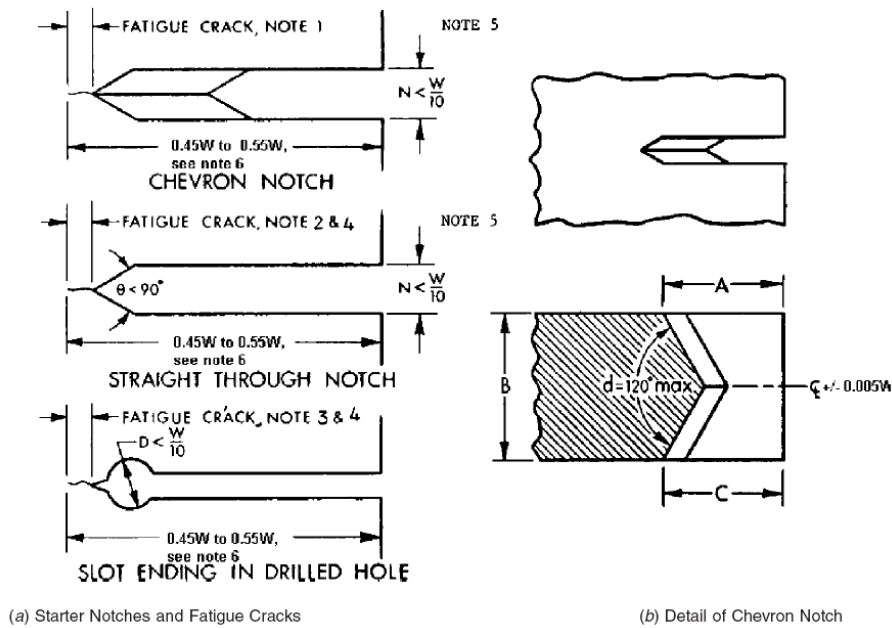


Figure B.8: Crack tip details

During the experiment, care should be taken on the issues that:

- Maximum stress intensity factor should not exceed 80 % of the  $K_q$  value that is guessed or obtained from previous experiment [59].
- For terminal stage of pre-cracking, maximum stress intensity factor should not exceed 60 % of the  $K_q$  obtained in previous experiment[59].

$K_q$  is the prospective fracture toughness value of the material. After the testing, if the validity criteria proposed in the standard are achieved, then the  $K_q$  value is named as the fracture toughness of the material. The calculation of  $K_q$  and the validity requirements will be discussed in Appendix B.3.0.3. Successive three experiments were done to obtain fracture toughness. At the first experiment the prospective value of fracture toughness ( $K_q$ ) is guessed around 25MPa which is higher than the fracture toughness of the real specimen. Therefore, the 60 % of the load is exceeded automatically and the validity requirements are not satisfied, in the preceding experiment the  $K_q$  is guessed as 15 MPa and during the whole pre-cracking stage the load is kept such that the maximum stress intensity factor is around the 40 % of the  $K_q$  value. The last two successive experiments are presented as the first and the second fracture toughness experiment in the Appendices B.3.0.1 and B.3.0.2.

### B.3.0.1 First fracture toughness experiment

Before starting the experiment, the dimensions of the specimens are measured again. The dimensions of the first specimen is presented in Table B.2.

Table B.2: Compact tension specimen test data

W	B	h	$a_i$	$a_f$
50.35 mm	23.50 mm	60.93 mm	20.24 mm	26.24 mm

where,

W : Specimen width, measured from the load line

B : Specimen thickness

h : The thickness of the saw cut described in Figure B.8

$a_i$  : The length of the initial notch measured from the load line

$a_f$  : The average length of the final length measured after the experiment

Before starting the experiment terminal length of the pre-crack should be determined which is the 0.0125W. Giving the cyclic loading calculated utilizing the Equation (B.1) which is the 40 % of the maximum load that the specimen will be broken with a fast fracture.

$$K_q = \frac{P_q}{B \sqrt{W}} \frac{(2 + \alpha)}{(1 - \alpha)^{\frac{3}{2}}} (0.886 + 4.64\alpha - 13.32\alpha^2 + 14.73\alpha^3 - 5.6\alpha^4) \quad (\text{B.1})$$

where,  $a$  is the crack length measured from the load line, and  $\alpha = a/W$ .  $K_q$  and  $P_q$  are respectively the prospective maximum stress intensity factor and the load that the fracture occurs at that crack length [59].

At first stages of pre-cracking sinusoidal cyclic loading with  $R = 0$  is applied with 60 % of the  $P_q$  that is calculated for the initial starter crack. As the terminal crack length is reached the load decreased to the 40 % of the  $P_q$  which is calculated for the terminal crack length. In other words, the maximum load is decreased from 13836.6N to the 8160.0 and the minimum load is kept as close as zero during the pre-cracking stage.

After the crack reaches the terminal value, the specimen is loaded with a load rate of 1KN/s which is in the range that the standard proposed for this geometry [59], and the Load vs Displacement data is recorded during the experiment.

Figure B.9 shows the load, and displacement data that is obtained during the test. The purple line in the graph denotes the tangent line to the linear region on the test data, and the red line denotes 95 % slope of the tangent line which crosses the test data. The intersection of the test data and the 95 % slope tangent line is called as  $K_q$  which is a candidate of  $K_{IC}$  if the validity requirements are achieved. The valid requirements will be explained in Appendix B.3.0.3.

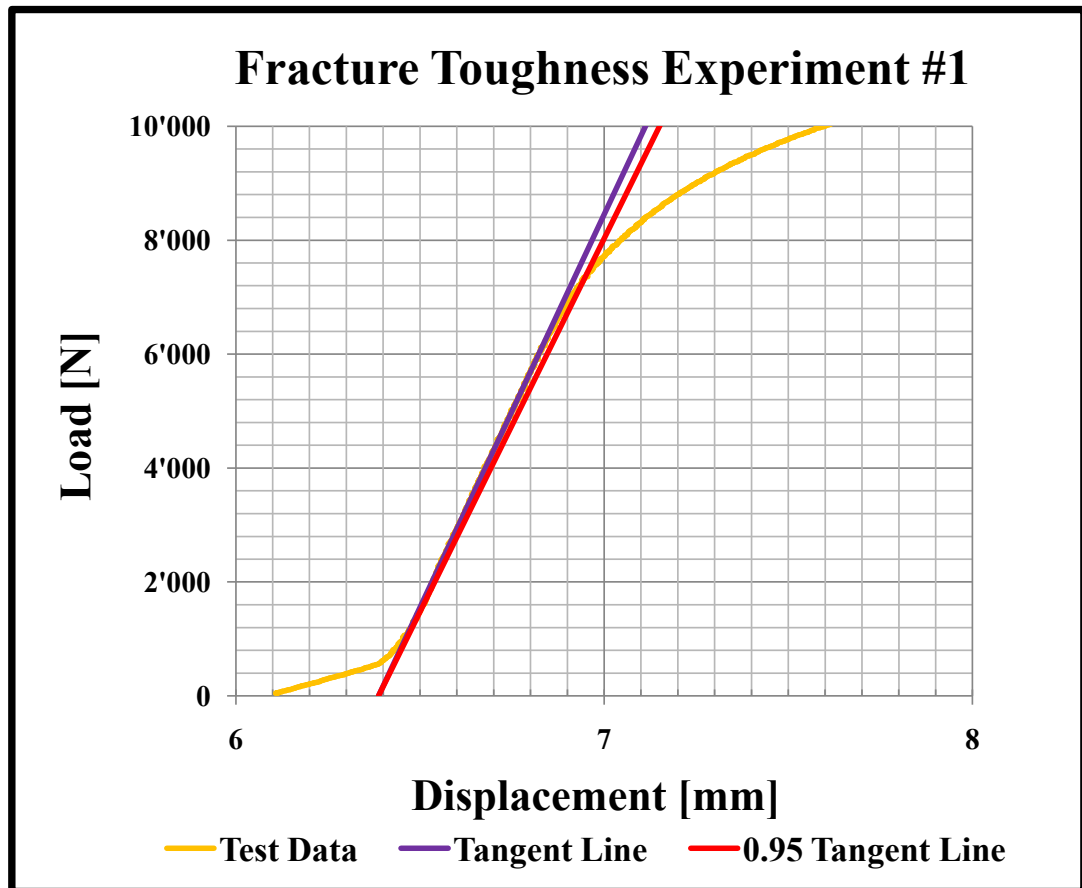


Figure B.9: Load vs Displacement data obtained from fracture toughness testing according to E-399

The results obtained from the experiment one is presented in Table B.3.

Table B.3: Compact tension specimen test results

W	B	$K_q$	$P_q$	$a$
50.35 mm	23.50 mm	15.07 MPa $\sqrt{m}$	7700 N	26.24 mm

### B.3.0.2 Second fracture toughness experiment

The same procedure that is described in Appendix B.3.0.1 is followed in this experiment. The dimensions of the second compact tension test specimen is given in Table B.4.

Table B.4: Compact tension specimen test data

W	B	h	$a_i$	$a_f$
50.54 mm	23.6 mm	60.8 mm	20 mm	25 mm

This time the loading rate is chosen as 0.5 KN/s which is again in the range that the standard is proposing for this geometry [59]. The load, displacement data collected in the second experiment is presented in Figure B.10.

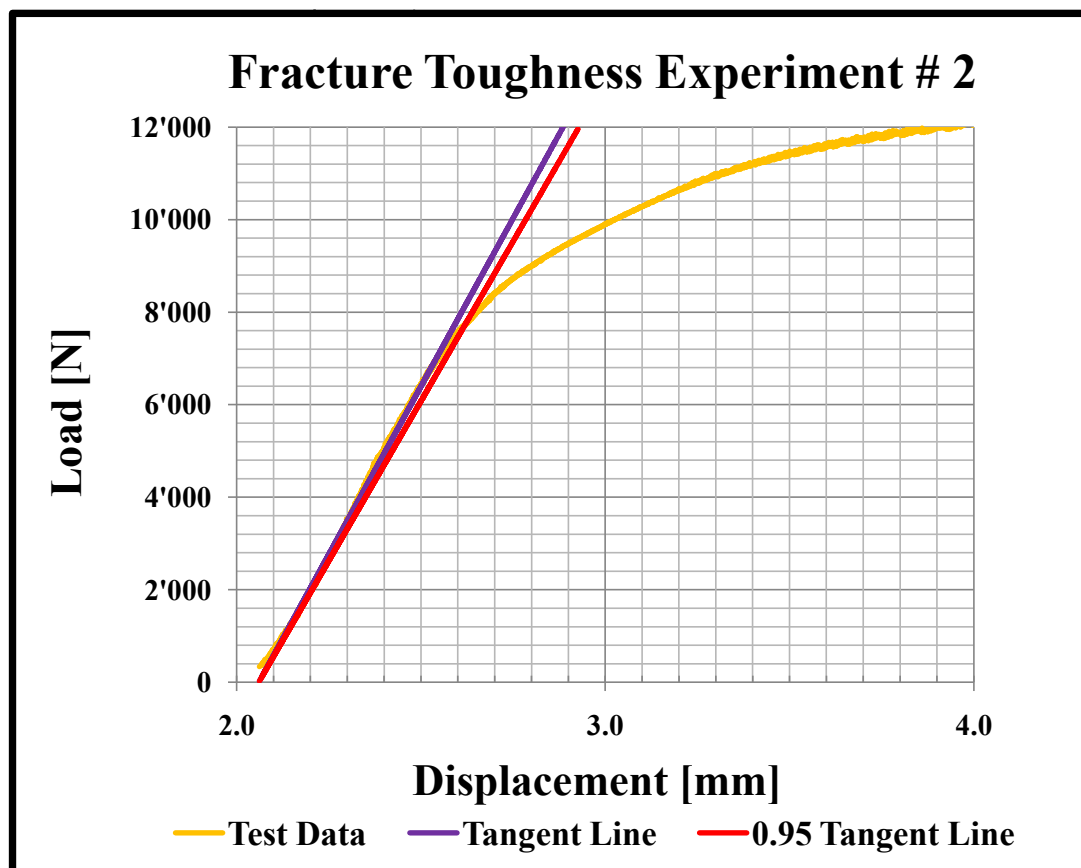


Figure B.10: Load vs Displacement data obtained from fracture toughness testing according to E-399

The test results for the second fracture toughness determination experiment is given in Table B.5.

Table B.5: Compact tension specimen test results

W	B	$K_q$	$P_q$	$a$
50.54 mm	23.40 mm	15.02 MPa $\sqrt{m}$	8000 N	25.63 mm

### B.3.0.3 Validity requirements, and Calculation of the $K_q$

The validity requirements, which are needed to be satisfied for the  $K_q$  to be called as fracture toughness of the material is listed below :

- The value of the  $2.5(K_q/\sigma_{ys})^2$  should be less than the un-cracked ligament which is  $W - a$ . Where the  $\sigma_{ys}$  is the 0.2 % offset yield stress obtained from the tension test in Appendix B.2.
- $K_{max}/E$  should not exceed  $0.003 \sqrt{m}$  during the experiment, where the  $K_{max}$  is the maximum stress intensity factor and the  $E$  is the Young's Modulus obtained from the tension test in Appendix B.2.
- The ratio  $P_{max}/P_q$ , where the  $P_{max}$  is the maximum load that the specimen is able to sustain, and  $P_q$  is the intersection of the test data with the 95 % tangent line as shown in Figures B.9 and B.10.

$K_q$  value of the aluminum 2124-T851 alloy is determined as 15MPa in two successive experiments. In both tests the first two requirements above are satisfied, however the third validity requirement is not satisfied. Therefore, the fracture toughness of the material could not be determined. This may be due to the misalignment of the testing fixtures or due to the unsymmetrical chevron notch. Moreover, the displacement gauge is recommended for measuring the displacement of the load line, but in this study the displacements of the load line is obtained by the MTS output.

The hardness of the specimen is obtained by the hardness test as 139 *Brinell*, which is close to the available data in the literature, therefore the it can be deduced that the material is not softened due to the over aging. Considering the composition and the temper condition of the material, which is very close to the material given in the literature, the fracture toughness value of 24 MPa  $\sqrt{m}$  is accepted. Later, during the successive crack growth experiments, as it is presented in Appendix B.4, it is observed that the fracture toughness value of the material is around 24 MPa  $\sqrt{m}$ .

## B.4 CRACK PROPAGATION TEST

The same experimental set-up which is introduced before in Figure B.5 is used in the crack propagation tests. Dimensions of the CT specimen, which is used in the experiments for determination of  $da/dN$  vs  $\Delta K$  curves, are given in Figure B.11. Five successive experiments were done to obtain the linear region on the  $da/dN$  vs  $\Delta K$  curve.

The crack length measuring systems which are working with a similar principal with strain measuring systems, are now widely being used in the world such as Fractomat Crack Measuring Device. Fractomat system in the Metallurgical and Materials Engineering Laboratory is intended to be used for measuring the crack length, but due to the lack of crack folios which are attached to the crack path, as illustrated before in Figure B.5b the traveler microscope is utilized, which is a very old historical device that allows magnification of 8X. Although the standard recommends the traveler microscope has 20X to 50X magnifying capacity [61], this tired old man proved itself by supplying surprisingly accurate data. One needs to be very careful trying to keep away the system from shaking even being careful when breathing which may lead to the measurement error and has to have sharp eyes with sharp hands to get a reliable data from the system. Every, one unit in the ocular with the built in ruler corresponds to the 0.1825 mm.

The experiments are performed under load control, with constant  $\Delta P$  loading which means the  $\Delta K$  is increasing during the experiment with growing crack length. This is the recommendation of the ASTM-E647 standard for the crack growth rate data expected above the  $10^{-8}[m/Cycle]$  [61]. Six successive experiments were done and only last two of them gives the reliable results that can be used for determination of the  $da/dN$  vs  $\Delta K$  curve.

The technical drawing of the crack growth rate experiment specimens is prepared in CATIA in accordance with the specifications in the ASTM-E647 [61] and the specimens are produced in the Metallurgy and Materials Engineering workshop. Figure B.11 shows the geometric properties of the compact tension (CT) specimens used in the experiments. In Figure B.11, all dimensions are given in mm. Figure B.12 shows the Compact tension test specimen geometry given in ASTM-E647 [61].

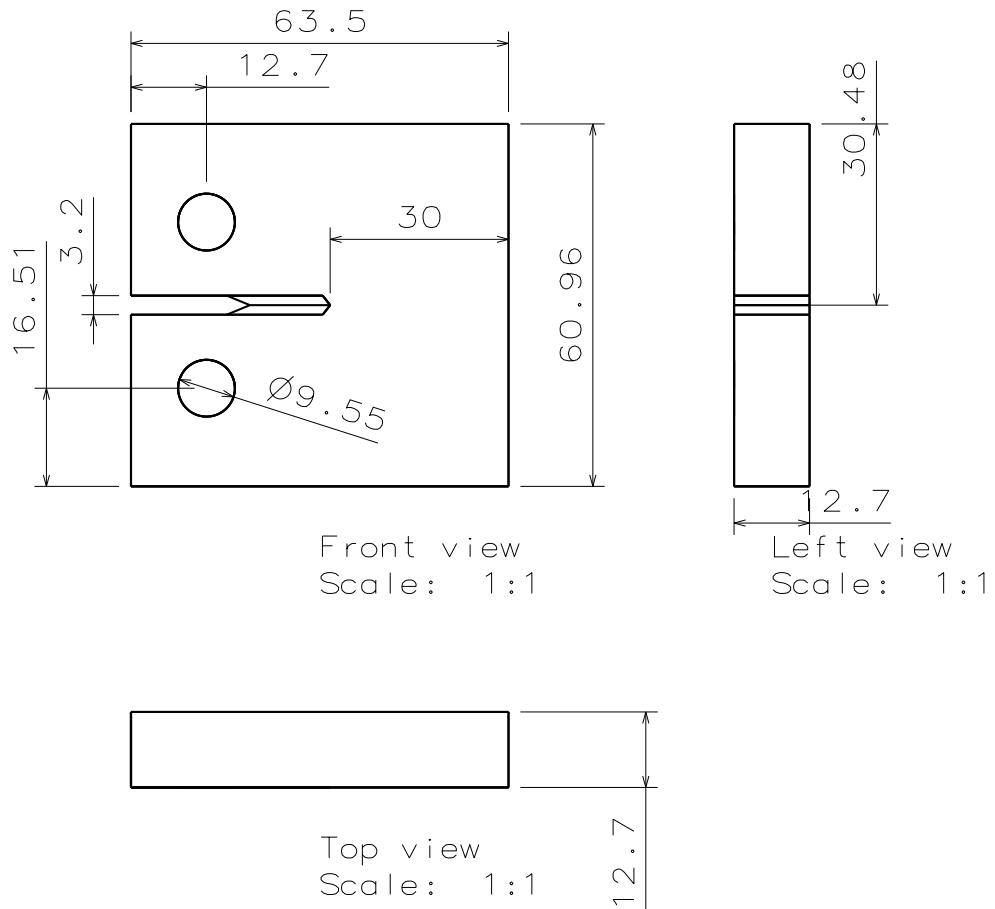


Figure B.11: Compact tension test specimen geometry used in the experiment

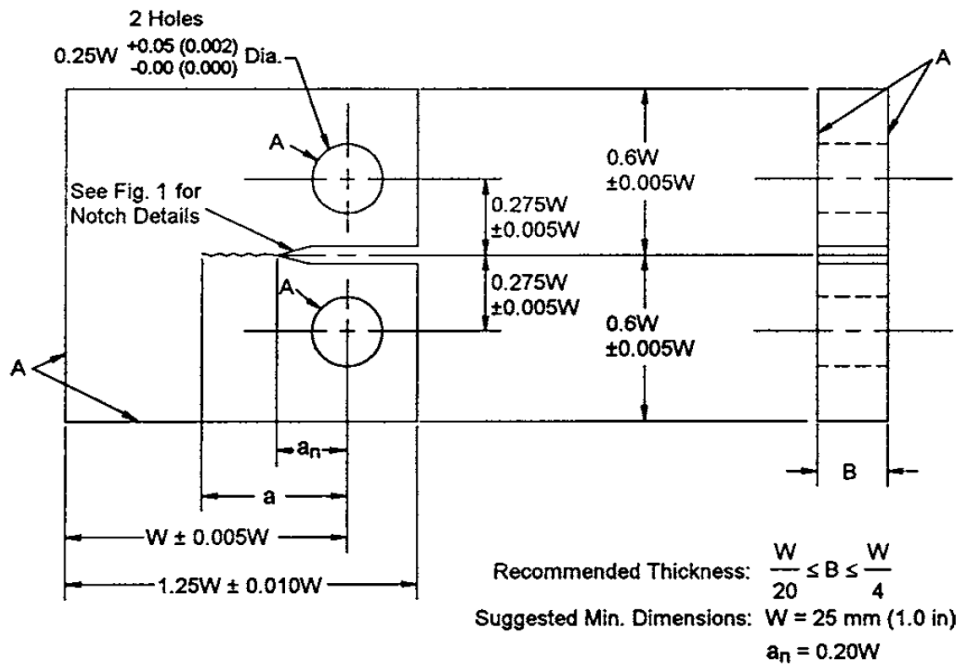


Figure B.12: Compact tension test specimen geometry given in ASTM-E647 [61].

According to ASTM-E647 [61], the crack tips should be one of the types given in Figure B.13. In this experiment the Chevron type crack tip is preferred, because it is more practical to induce the initial crack, and it is almost guaranteed that the crack starts from the notch, which considerably reduces the possibility of double starter crack.

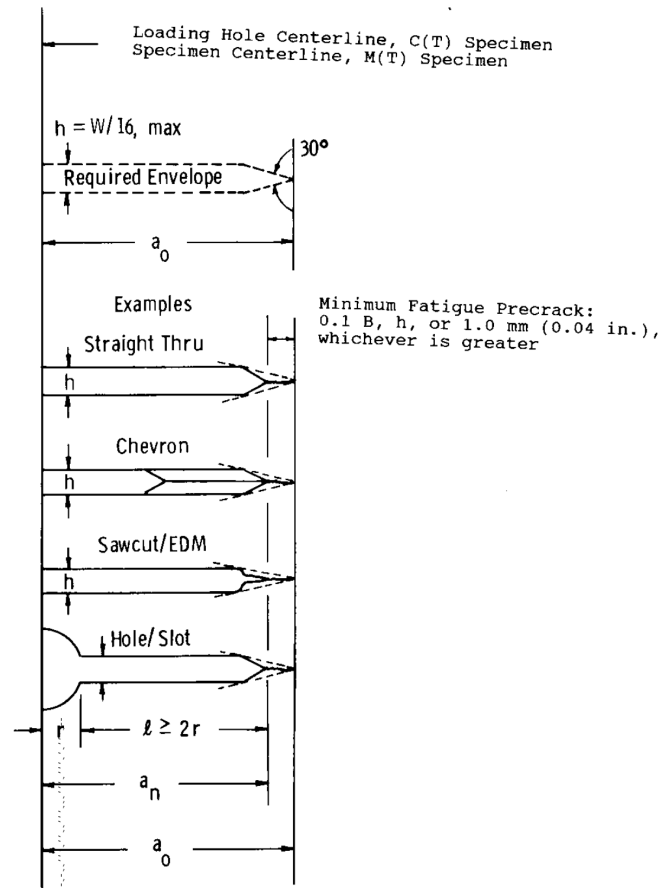


Figure B.13: Crack tip types and the minimum fatigue pre-crack size for compact tension test specimen [61]

The compact tension test condition data is presented in Table B.7. It should be noted that the  $R$  ratio is chosen very close to zero but not zero. This is due to prevent losing contact between the specimen lug and the pins. Standard recommends that the  $K_{max}$  should be stable in pre-cracking as possible. Further decreasing of the maximum load more than 20 % and decreasing more than 10 % is not recommended due to the transient effects which may affect the measurements. At the pre-cracking stage initially the maximum load  $P_{max}$  is set to 2500  $N$  which is the 30 % of the critical load may lead to the fracture with a starter crack length of 21.3  $mm$ . The  $R$  ratio is kept as close as zero. Applying the sinusoidal loading more than 100'000 cycles the initial starter crack not observed, therefore the pre-cracking load is

re-selected as 4000  $N$  which is the 48 % of the maximum load for the initial crack length.

The terminal crack length of 2.6  $mm$  is reached approximately after 80'000 cycle of propagation, the maximum load is gradually decreased with an increment less than 10 % as recommended in the standard [61]. At the last stages of the pre-cracking, the load is stabilized at a maximum load  $P_{max} = 2500N$  with  $R \cong 0$ .

The following requirements has to be satisfied in order to get valid results from the experiment:

- It is required that the machined notch in the compact specimen should be at least  $0.2W$  so that the  $K$  values are not influenced by the small variations in the location and dimensions of the loading pin holes.
- The terminal value of the pre-crack length should be greater than the maximum of the preceding values which are;  $0.1B$ ,  $h$  or  $1mm$ , where  $h$  is the distance due to saw-cut as illustrated in Figure B.13.
- The value of the  $4/\pi(K_{max}/\sigma_{ys})^2$  should be less or equal to the un-cracked ligament which is  $W - a$ .

Standard is also recommending to collect the data in such intervals that the  $da/dN$  should be evenly distributed with respect to the  $\Delta K$  [61]. For the compact tension specimens the suggested intervals are:

$$\Delta a \leq 0.04W \quad \text{for} \quad 0.25 \leq a/W \leq 0.40$$

$$\Delta a \leq 0.02W \quad \text{for} \quad 0.40 \leq a/W \leq 0.60$$

$$\Delta a \leq 0.01W \quad \text{for} \quad 0.25 \leq a/W$$

For the CT specimen used in the experiments, the intervals of measurement is then becomes to be:

$$\Delta a \leq 2.02mm \quad \text{for} \quad 12.6mm \leq a \leq 20.2mm$$

$$\Delta a \leq 1.01mm \quad \text{for} \quad 20.2mm \leq a \leq 30.3mm$$

$$\Delta a \leq 0.05mm \quad \text{for} \quad 30.3 \leq a$$

The crack lengths and the cycles which are presented in Figure B.14 are recorded with paying attention to the recommended crack length intervals during the experiment. In order to obtain the  $da/dN$ , derivative of the crack length vs cycles graph is needed. Standard is recommending two methods which are, Secant Method, and the Incremental Polynomial Method. In this thesis an alternative solution to this problem is proposed, which is, fitting a suitable analytic equation to the Cycles vs Crack length curve, and differentiate the equation with respect to the cycles to get the  $da/dN$  data for a specific crack length.

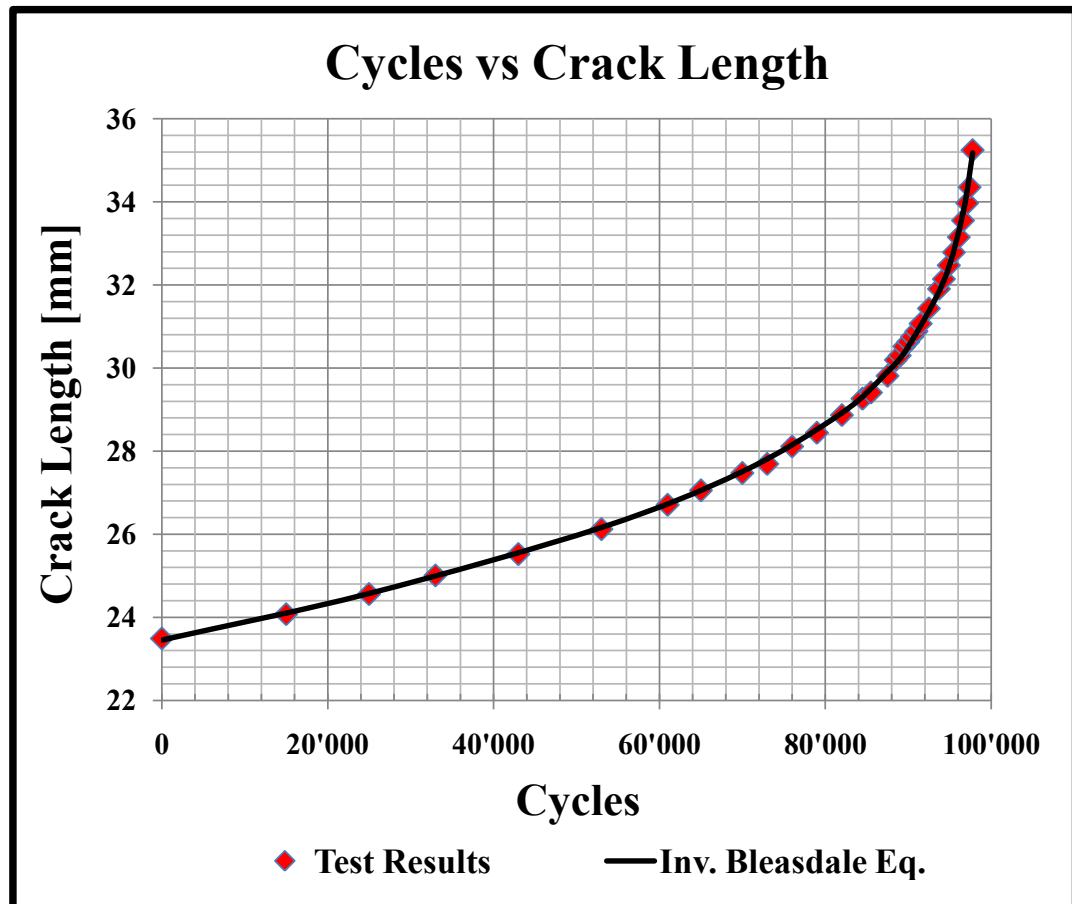


Figure B.14: Cycles vs Crack Length data obtained according to the ASTM-E647 [61]

Utilizing the function finder available in zunzun.com [62] the best analytic equation with least error is chosen to be the Inverse Bleasdale Equation with Offset presented as Equation (B.2).

$$y = \frac{x}{(a + bx)^{-1.0/c}} + Offset \quad (B.2)$$

For representing the experiment data,  $x$  and  $y$  in Equation (B.2) will be replaced by respectively *Cycles* and *Crack Length* and constant coefficients  $a, b, c$  and *Offset* are obtained. The

coefficients and the fitting target of lowest sum of squared absolute error is presented in Table B.6. As it can be seen from the Figure B.14 the Inverse Bleasdale Equation with Offset is perfectly fitting to the data obtained from the experiment.

Table B.6: Inverse Bleasdale Equation Coefficients and squared absolute error

a	b	c	Offset	Squared absolute error
7.97E+026	-7,99E+021	-3,64	2,35	5,81E-008

The  $\Delta K$  values corresponding to the crack length, at which the  $da/dN$  data obtained by taking the derivative of the Equation (B.2), can be calculated utilizing the Equation (B.3) which is proposed by the standard [61].

$$\Delta K = \frac{\Delta P}{B \sqrt{W}} \frac{(2 + \alpha)}{(1 - \alpha)^{\frac{3}{2}}} (0.886 + 4.64\alpha - 13.32\alpha^2 + 14.73\alpha^3 - 5.6\alpha^4) \quad (\text{B.3})$$

where,  $a$  is the crack length measured from the load line, and  $\alpha = a/W$ . According to the standard [61], Equation (B.3) is valid for  $a/W \geq 0.2$ . The experiment conditions for  $da/dN$  vs  $\Delta K$  curve determination is presented in Table B.7.

Table B.7: Compact tension specimen test data

$P_{max}$	$P_{min}$	$\Delta P$	B	W	Frequency
2500 [N]	50 [N]	2450 [N]	12.43 [mm]	50.16 [mm]	10 Hz

where,

$P_{max}$  : Maximum applied load in a cycle during the experiment

$P_{min}$  : Minimum applied load in a cycle during the experiment

$\Delta P$  :  $P_{max} - P_{min}$ , load range in a cycle

B : Specimen thickness

W : Specimen width described in Figure B.12

Using the data given in Table B.7 and the crack length vs cycle data collected during the experiment as presented in Figure B.14 with the Equation (B.3),  $da/dN$  vs  $\Delta K$  curve which is presented in Figure B.17, is obtained. The  $da/dN$  vs  $\Delta K$  curve obtained according to ASTM-E647 [61] is used for the life calculations and determining the Forman Constants is described in Section 4.2.5.

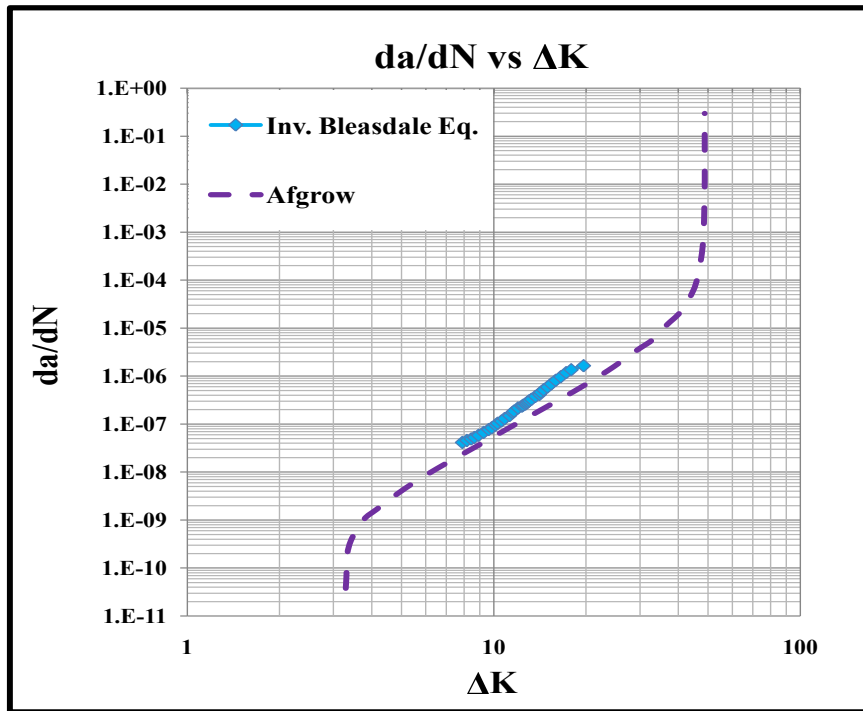


Figure B.15: Crack growth rate changing with the range of stress intensity factor data obtained from the experiment, Inverse Bleasdale with Offset

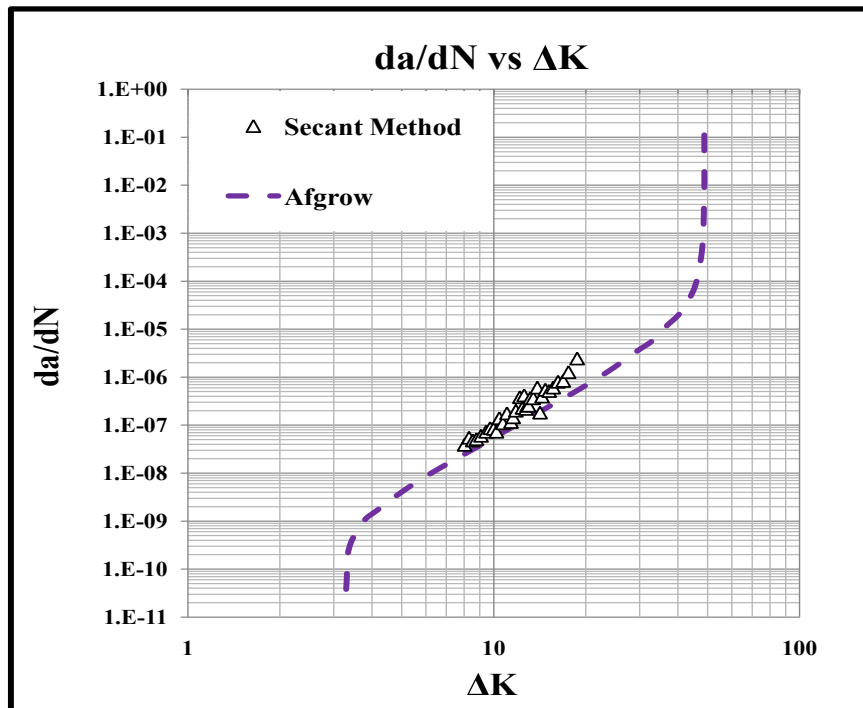


Figure B.16: Crack growth rate changing with the range of stress intensity factor data obtained from the experiment, Secant Method

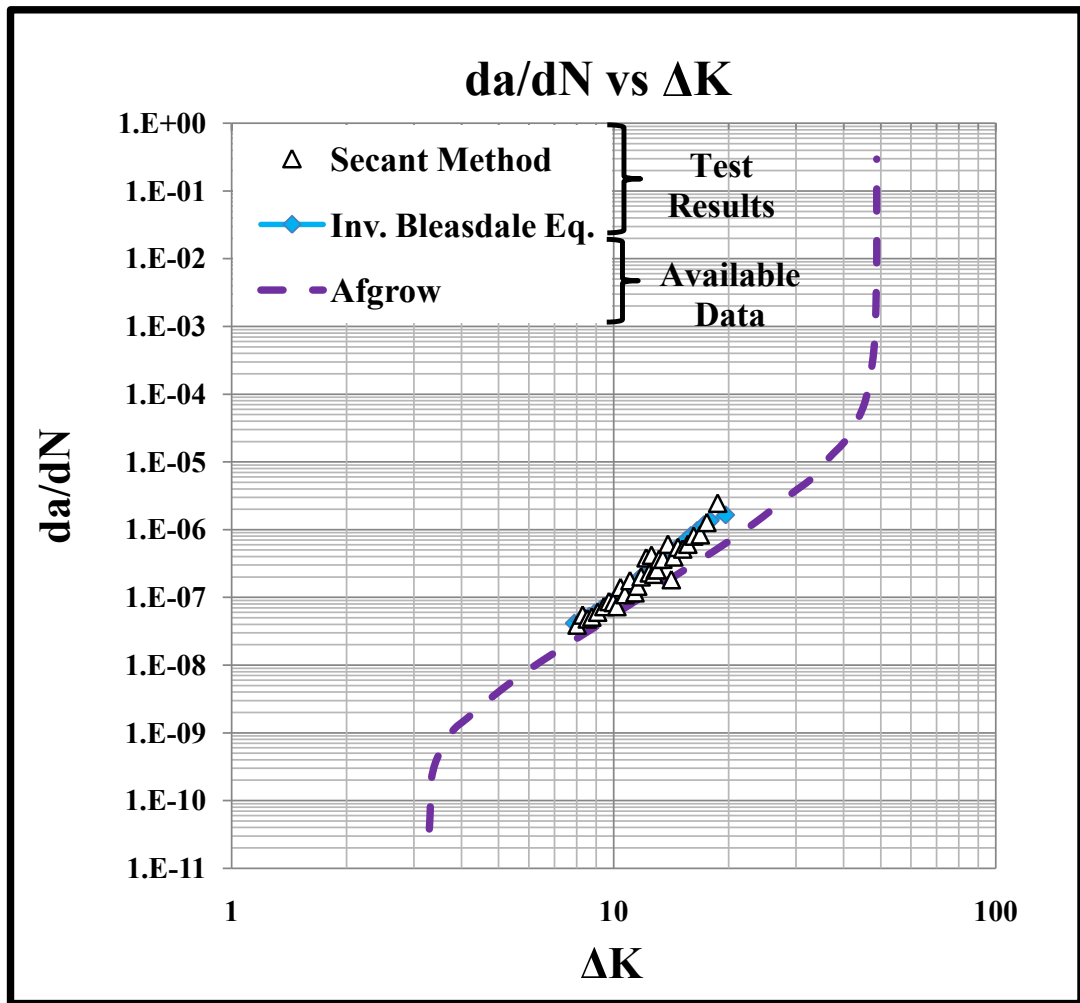


Figure B.17: Comparison of the crack growth rate changing with the range of stress intensity factor data obtained with Secant Method, and curve fitting with Inverse Bleasdale Eq. with Offset